COPPE
Instituto Alberto Luiz Coimbra de Pós-Graduação e Pesquisa de Engenharia
UFRJ

COALESCENCE OF ELLIPSOIDAL-WOBBLING BUBBLES AT A SURFACTANT-FREE INTERFACE

Eric Mauricio González Fontalvo

Tese de Doutorado apresentada ao Programa de Pós-graduação em Engenharia Química, COPPE, da Universidade Federal do Rio de Janeiro, como parte dos requisitos necessários à obtenção do título de Doutor em Engenharia Química.

Orientadores: Paulo Laranjeira da Cunha Lage
Juliana Braga Rodrigues Loureiro

Rio de Janeiro
Novembro de 2024

COALESCENCE OF ELLIPSOIDAL-WOBBLING BUBBLES AT A SURFACTANT-FREE INTERFACE

Eric Mauricio González Fontalvo

TESE SUBMETIDA AO CORPO DOCENTE DO INSTITUTO ALBERTO LUIZ COIMBRA DE PÓS-GRADUAÇÃO E PESQUISA DE ENGENHARIA DA UNIVERSIDADE FEDERAL DO RIO DE JANEIRO COMO PARTE DOS REQUISITOS NECESSÁRIOS PARA A OBTENÇÃO DO GRAU DE DOUTOR EM CIÊNCIAS EM ENGENHARIA QUÍMICA.

Orientadores: Paulo Laranjeira da Cunha Lage
Juliana Braga Rodrigues Loureiro

Aprovada por: Prof. Paulo Laranjeira da Cunha Lage
Prof. Juliana Braga Rodrigues Loureiro
Prof. Gabriel Gonçalves da Silva Ferreira
Prof. Ricardo de Andrade Medronho
Prof. Igor Braga de Paula

RIO DE JANEIRO, RJ – BRASIL
NOVEMBRO DE 2024

Fontalvo, Eric Mauricio González

Coalescence of Ellipsoidal-Wobbling Bubbles at a Surfactant-Free Interface/Eric Mauricio González Fontalvo. – Rio de Janeiro: UFRJ/COPPE, 2024.

XIV, 91 p.: il.; 29, 7cm.

Orientadores: Paulo Laranjeira da Cunha Lage

Juliana Braga Rodrigues Loureiro

Tese (doutorado) – UFRJ/COPPE/Programa de Engenharia Química, 2024.

Referências Bibliográficas: p. 72 – 76.

1. bubble coalescence. 2. coalescence time. 3. liquid film thickness. 4. drainage rate. I. Lage, Paulo Laranjeira da Cunha *et al.* II. Universidade Federal do Rio de Janeiro, COPPE, Programa de Engenharia Química. III. Título.

A mí, por no haber desistido. A Dios, gracias a Él, todo es posible. A mi familia: papá, mamá, tía, y hermanos, por ser siempre mi inspiración, mi respeto y mi apoyo incondicional para cualquier objetivo que me propongo. Y especialmente a Fabio, in memoriam, e a Cali por ser mi luz y mi guía para lograrlo. Los amo.

Acknowledgments

A special thanks to Prof. Paulo Lage for his dedication and contribution to this work. The knowledge and vast experience he shared were invaluable, in addition to the time and effort he devoted.

To Prof. Juliana Loureiro, for agreeing to be my co-advisor during this period and for her insightful ideas in developing the work.

I have great respect and admiration for their knowledge.

I would like to thank the Termofluidodinâmica Laboratory (LTFD), of which I was a part during these years, as well as the students and staff—Amanda, Antônio, Flávio, Andressa, Ana, and André—for their help in organizing ideas and their support throughout this journey.

To the Núcleo Interdisciplinar de Dinâmica dos Fluidos (NIDF), where the experiments were conducted: Cristian, Leonardo, Gustavo, Laert, Adão, Alexandre, Vinícius, Prof. Aibe, and Prof. Átila, I express my gratitude for the use of the facilities and equipment, as well as for their patience during my first foray into the experimental field of fluid dynamics.

I would also like to thank professors Gabriel Ferreira, Igor De Paula, and Ricardo Medronho for agreeing to serve on the examining board.

Finally, I am grateful to the Brazilian government funding agencies CNPq (process number 165784/2018-0) and CAPES (financial code 001), as well as the Colombian foundation COLFUTURO (PCB 2022), for the partial financial support provided during the development of this work.

Resumo da Tese apresentada à COPPE/UFRJ como parte dos requisitos necessários para a obtenção do grau de Doutor em Ciências (D.Sc.)

COALESCÊNCIA DE BOLHAS ELIPSOIDAIS-OSCILANTES EM UMA INTERFACE LIVRE DE SURFACTANTES

Eric Mauricio González Fontalvo

Novembro/2024

Orientadores: Paulo Laranjeira da Cunha Lage
Juliana Braga Rodrigues Loureiro

Programa: Engenharia Química

A fim de obter um conjunto mais completo de dados experimentais sobre o processo de coalescência de bolhas, foram levados a cabo experimentos de coalescência de bolhas esferoidais com uma interface gás-líquido plana e livre de surfactantes. As propriedades dos fluidos foram medidas e correlacionadas em uma faixa de temperatura entre 20 e 30 °C. Técnicas de visualização em fluidos foram utilizadas para estimar o tamanho, velocidade e tempo de coalescência das bolhas. O tempo de coalescência foi determinado usando dois critérios de "colisão": o critério físico, baseado na distância entre a superfície superior da bolha e a interface, e o critério hidrodinâmico, baseado na velocidade da bolha. As distribuições gama representaram bem a distribuição dos tempos de coalescência das bolhas em suas velocidades terminais. Foi encontrada uma relação linear entre o tempo de coalescência e o número de rebotes. O critério hidrodinâmico foi mais consistente na representação dos nossos dados sobre o tempo de coalescência. Um modelo simplificado foi desenvolvido para descrever o movimento de uma bolha após sua primeira colisão com a interface. O modelo foi validado com dados experimentais e previu adequadamente o movimento das bolhas até a coalescência. Uma análise comparativa mostrou que o modelo funciona bem usando dois conjuntos de condições iniciais, prevendo as velocidades experimentais e a frequência de oscilação das bolhas nos experimentos.

Abstract of Thesis presented to COPPE/UFRJ as a partial fulfillment of the requirements for the degree of Doctor of Science (D.Sc.)

COALESCENCE OF ELLIPSOIDAL-WOBBLING BUBBLES AT A SURFACTANT-FREE INTERFACE

Eric Mauricio González Fontalvo

November/2024

Advisors: Paulo Laranjeira da Cunha Lage
Juliana Braga Rodrigues Loureiro

Department: Chemical Engineering

In order to obtain a more complete set of experimental data on the bubble coalescence process, experiments were conducted with spheroidal bubbles coalescing with a flat and surfactant-free gas-liquid interface. The fluid properties were measured and correlated over a temperature range of 20 to 30 °C. Fluid visualization techniques were used to estimate the size, velocity, and coalescence time of the bubbles. The coalescence time was determined using two "collision" criteria: the physical criterion, based on the distance between the top surface of the bubble and the interface, and the hydrodynamic criterion, based on the bubble's velocity. Gamma distributions effectively represented the distribution of bubble coalescence times at their terminal velocities. A linear relationship was found between coalescence time and the number of bounces. The hydrodynamic criterion was more consistent in representing our data on coalescence time. A simplified model was developed to describe the movement of a bubble after its first collision with the interface. The model was validated with experimental data and predicted the bubble's motion and behavior until coalescence. A comparative analysis showed that the model performed well using two sets of initial conditions, predicting the experimental velocities and the bubbles' oscillation frequency observed in the experiments.

Contents

List of Figures

List of Tables

Chapter 1

Introduction

1.1 Motivation

The study of bubble coalescence plays an important part in many areas of interest in industrial, engineering and technological applications, such as mass and heat transfer equipment e.g. bubble columns [2, 3], separators [4], mineral flotation [5, 6], two-phase flow in pipes [7, 8], among others. The experimental analysis of this complex phenomenon improves models and predictions of dispersed multiphase processes where coalescence can occur.

Coalescence refers to the process in which two or more fluid particles merge into one after a collision, resulting in the loss of the original particles' individual identities. The probability that a collision will lead to coalescence is defined as coalescence efficiency. In previous studies, several air bubble collisions were observed within the cell. However, despite theoretical models predicting a high probability of coalescence, none were actually observed. The coalescence of bubbles at interfaces resembles the interaction between a small bubble and one of infinite diameter over an infinite interaction time. In this scenario, the probability of coalescence is always one, meaning every collision leads to coalescence. This approach has been widely adopted for its simplicity and high efficiency.

The literature review of bubbles coalescence at an interface showed that it is important to obtain a more complete data set on the liquid film drainage process due to the diversity of theoretical assumptions and a lack of estimation of the initial drainage stage in the ellipsoidal-wobbling bubble regime. For this reason, experiments of air bubbles colliding at a flat free air-water interface without the presence of surfactants were carried out. We used high-speed imaging in fluids to estimate the bubble characteristics and coalescence time. A simplified model was proposed to predict the motion and velocity of bubble at the interface until coalescence.

This work provides novel insights into bubble coalescence, complementing exist-

ing data and presenting results that align with previous knowledge. These results are important for planning new experiments of bubbles' coalescence using other fluids and conditions.

1.2 Objectives

1.2.1 General Objective

- Realize an analysis of the coalescence time of ellipsoidal-wobbling air bubbles colliding with an air-water interface for different approaching velocities.

1.2.2 Specific Objectives

- Adapt the coalescence cell built by COELHO [9] for experiments of bubble coalescence with a flat interface.
- Measure density, viscosity, electrical conductivity, and surface tension at different temperatures in a working range of 20 to 30 °C.
- Calculate the coalescence time of an individual distribution of bubbles.
- Analyze bubbles' bouncing and coalescence criterion.

1.3 Organization

The work is divided into the following chapters.

Chapter 2 provides a literature review concerning the effect of the characteristics of bubbles rising in still liquid on the coalescence time at a flat gas-liquid interface without surfactants and the modeling of bubble bouncing at the interface until coalescence.

Chapter 3 presents the experimental analysis of the coalescence time of bubbles at a interface with the assessment of two collision criteria.

Chapter 4 comprises the modeling of bubble bouncing and the determination of the critical Weber number for coalescence.

Conclusions and suggestions are provided in Chapter 5. Additionally, the document includes bibliographic references and appendices.

Chapter 2

Literature Review

The shape and movement of bubbles in a fluid due to forces such as gravity, drag, weight, and added mass have been addressed in several literature works and an *a priori* acknowledgment of dimensionless numbers such as Reynolds, Weber, Morton, Eötvös, and Galilei [10, 11] can effectively predict the regime and the current conditions of bounce and coalescence between bubbles [12–14]. To understand the coalescence mechanism, several studies have analyzed the coalescence of bubbles with interfaces, as well as the parameters that influence the contact and the coalescence times. This chapter summarizes the literature on bubble-interface coalescence experiments without the presence of surfactants. Additionally, it presents a review of models for such approach.

2.1 Bubble-Interface Coalescence Experiments

The simplest system for the study of coalescence involves the collision of bubbles with flat interfaces. The bubble coalescence with interfaces resembles an interplay between a small bubble and a bubble of infinite diameter for an infinite interaction time. This approach has been widespread due to its simplicity and high efficiency.

KIRKPATRICK e LOCKETT [15] carried out a set of experiments on bubble coalescence with flat interfaces to understand the influence of approach velocity on coalescence. In their first experiment, a cloud of air bubbles was kept within a region of a vertical tube by a downward water flow. They observed an almost complete absence of coalescence attributed to the large approach velocities of bubbles in the cloud. The second experiment confirmed the effect of the approach velocity by analyzing the coalescence of a single bubble with a diameter of 5 mm colliding with an air-water interface. They found that bubble coalescence was rapid at a low approach velocity because the film rupture occurred before the bubble bounced, while, at a high approach velocity, the bubble bounced before the film rupture, considerably increasing the coalescence time.

DOUBLIEZ [16] performed experiments to measure the thickness of a thin liquid film formed between an interface and approaching bubbles at terminal velocity using either distilled water or alcoholic solutions. Bubbles from 0.54 to 0.86 mm in diameter were formed at the tip of a capillary tube by blowing nitrogen at a rate of less than one bubble per second. He measured the liquid film thickness using interference fringe shifts, showing that it can reach the order of microns. In addition, he concluded that the models based on the lubrication theory fail to predict the initial drainage stage due to their assumptions.

SANADA *et al.* [17] conducted bubble-interface coalescence experiments using silicone oil and nitrogen bubbles recorded using a high-speed video camera. They concluded that the coalescence time is a single function of the Weber number in low-viscosity liquids with $Mo \lesssim O(10^{-8})$, observing that the coalescence time increases with the Weber number. The number of bounces was the most influential parameter determining the coalescence time. In addition, they determined a critical Weber number for coalescence for low-viscosity liquids that agreed well with the experimental and theoretical results of [18], whose values are $We_{crit} = 0.104$ and 0.117, respectively. They showed that the coalescence time is longer for a high-viscosity liquid for the same Weber number. They also observed the formation of foaming above the interface of high-viscosity liquids.

SUÑOL e GONZÁLEZ-CINCA [13] observed air bubbles with diameters between 0.27 and 1.85 mm rising and bouncing at an ethanol-air interface. They concluded that the bouncing time, defined between the first collision (the first maximum in the bubble position) and the coalescence, increases linearly with the Weber number, and the height of the first bounce also depends linearly on the bubble equivalent diameter. They noted that the movement of the bubble center is similar to a damped oscillator, and a large bubble does not reach heights larger than its equivalent diameter after the first bounce because the buoyancy force drastically decreases the bubble velocity after the "collision."

ZAWALA e MALYSA [19] studied the influence of the impact velocity and the thickness of the film formed on the coalescence time at a water-air interface of bubbles with diameters ranging between 1 and 1.76 mm. They concluded that the higher the impact velocity, the larger the bubble shape deformation and the liquid film thickness formed between the bubble and the interface. Furthermore, the larger the liquid film thickness, the longer the time required to reach the film rupture thickness, in other words, the more intense the bubble bouncing. The latter statement agrees with KIRKPATRICK e LOCKETT [15] results. ZAWALA e MALYSA [19] estimated a critical thickness of rupture of the liquid film using a lubrication model between 5 and 18 μm for coalescence times of 3 and 5 ms, respectively, assuming an initial film thickness of 100 μm.

SATO *et al.* [20] conducted experiments of bubbles bouncing at a free surface in pure water to verify the validity of a simple mass-spring model. The model agrees well with the experiments, and the time of the bubbles contacting the free surface was a function of the characteristic period of the oscillator.

HORN *et al.* [14] presented a coalescence map for bubbles in surfactant-free aqueous electrolyte solutions consisting of a plot of salt concentration against bubble approaching speed to indicate the transitions between the different types of behavior during bubble collisions being affected by surface forces, the thin film drainage and the boundary conditions (mobile and immobile interface) at the air-water interface. They validated a compilation of literature results including KIRKPATRICK e LOCKETT [15] and LEHR *et al.* [21]. For these authors, the critical Weber number above which the bubbles bounce is equal to 1, which agrees to the solutions of the flow and deformation during the approach of two bubbles along their centerline presented by CHESTERS e HOFMAN [22], but is only half of the critical Weber number measured experimentally by SANADA *et al.* [12]. The criterion of critical Weber number separates two regimes in the bubble coalescence map defined by HORN *et al.* [14]: the rapid inertial drainage and the elastic bounce regime.

The bubble regime can be effectively predicted using the dimensionless numbers Galilei, Eötvös, Reynolds, and Morton. Dimensionless numbers such as Eo and Mo depend solely on the properties of the continuous and dispersed phases, whereas Re_d and Mo also depend on the phase velocities in addition to the properties of the phases. Figure 2.1 presents the Eötvös, Morton, and equivalent diameter of the experimental data set I by FONTALVO *et al.* [27] plotted within the Eötvös-Morton-Reynolds diagram by CLIFT *et al.* [10]. The expected bubble regime corresponds to the oscillating ellipsoidal or wobbling region in the gray region on the map, which aligns with the observations from the bubble trajectories. Experiments were conducted in a region where the terminal velocity was achieved, but the ellipsoidal motion had not yet fully developed. To analyze the influence of this trajectory on coalescence time, it is necessary to use more than one camera to capture the displacement in different planes.

Likewise, the experimental dimensionless Galilei and Eötvös numbers were plotted in the Galilei - Eötvös diagram presented by TRIPATHI *et al.* [11]. As shown in Figure 2.2, the expected bubble regime corresponds to the oscillatory region (depicted in blue on the map) and is located very close to the yellow region, representing peripheral and central breakage. This proximity may explain the appearance of some satellite bubbles observed in previous experiments. The Galilei number can also be calculated using the relationship between the Morton and Eötvös numbers, as suggested by TRIPATHI *et al.*, given by $Mo = Eo^3/Ga^4$. Additionally, a secondary vertical axis corresponding to the equivalent diameter was added to the diagram for

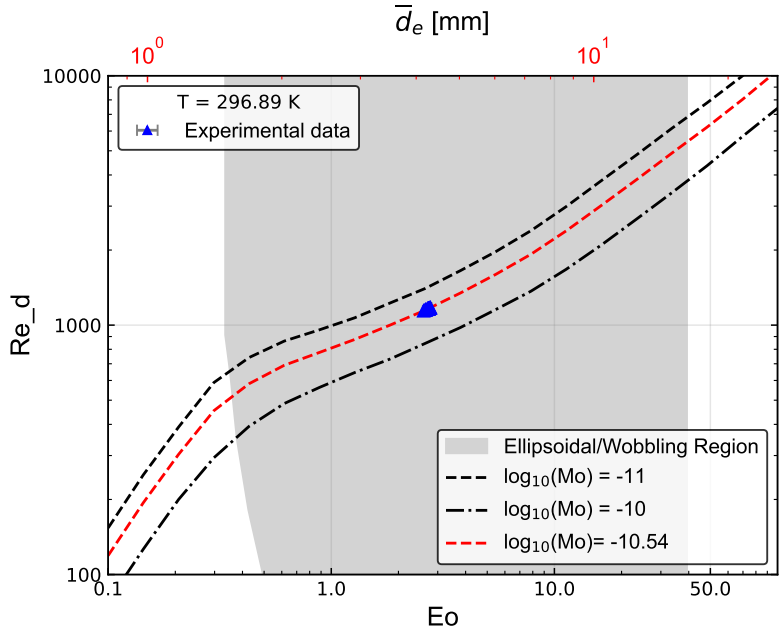

Figure 2.1: Data set I in Eötvös-Reynolds-Morton diagram [10].

the Morton number of $\log_{10}(Mo) = -10.54$.

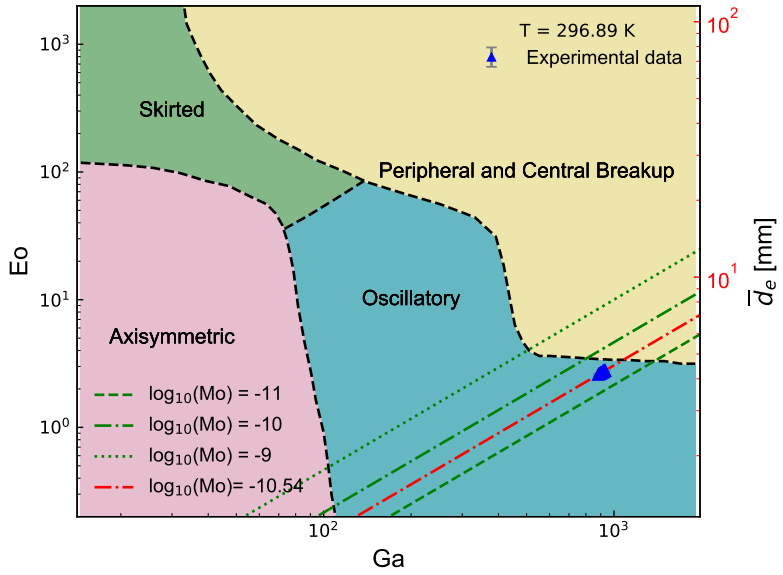

Figure 2.2: Data set I in Galilei-Eötvös-Morton diagram [11].

Although the literature on bubble coalescence at a gas-liquid interface is extensive, few works have conducted experiments on bubble-interface coalescence in the ellipsoidal-wobbling regime. Therefore, more data on this process is necessary to understand the phenomenon, given the diversity of theoretical assumptions and the lack of a precise definition of the initial drainage stage.

In this work, experiments were conducted with wobbling air bubbles of approximately 4 mm in diameter, colliding on a flat, surfactant-free air-water interface.

The objective was to estimate bubble characteristics and coalescence times using advanced high-speed imaging techniques, providing a more comprehensive analysis of the phenomenon. By focusing on the ellipsoidal-wobbling regime, this study addresses a gap in the literature, revealing longer coalescence times and a higher number of bounces compared to previously reported values. Furthermore, a linear relationship between the coalescence time and the number of bounces was established, indicating a constant period for the experiments. These findings enhance the understanding of bubble coalescence and significantly advance knowledge in this field.

2.2 Bubble-Interface Coalescence Models

The coalescence frequency is calculated by physical models as the product of two distinct functions: collision frequency and coalescence efficiency. The derived models, based on physical quantities, are defined according to the mechanisms of each collision [2, 23]. These models determine efficiency as the ratio between coalescence time and interaction time. The bubble-interface approach allows the liquid film to drain until it reaches its critical thickness for rupture, invariably leading to coalescence. Thus, the probability of coalescence is always one. Therefore, modeling this phenomenon focuses on the film drainage rate during the collision and the bouncing of the approaching bubble at the interface.

DUINEVELD [18] used the coalescence and bouncing condition for two bubbles derived by CHESTERS e HOFMAN [22] to model the approach of a spherical bubble to a free surface. The procedure used by the author solves an equation of motion until the bubble hits the surface and deforms. This condition depends on an initial distance from the bubble's center of mass to the surface. After that, they apply the bouncing criterion determined by the approach velocity. That is, if the velocity is too low the bubble coalesces with the free surface, otherwise, the pressure in the liquid film between the bubble and the free surface strongly increases, deforms the bubble, and exerts a repelling force incorporated into the equation system.

ZAWALA *et al.* [24] analyzed the bouncing of air bubbles with 1 mm in diameter at resting and vibrating air/oil interfaces. They modeled the film drainage time and the dynamic radius of the liquid film formed. The model showed that the drainage time is directly proportional to the liquid viscosity, the radius of the film formed (in second power), and inversely proportional to the driving force causing the film thinning. The model also depends on the initial film thickness. According to experiments, the deformation (radius of the liquid film) allows the bubble to bounce when the drainage time is longer than the contact time with the interface i.e. a large deformation increases the drainage time. They also observed that the bub-

bles approached the interface at a constant terminal velocity, then rapidly slowed, stopped, and bounced. After bouncing, the bubbles began a second approach. The time to bubble rupture depends on bubble size, liquid viscosity, and the number of rebounds.

SATO *et al.* [20] also derived a model to predict the time duration of the contact of a bubble upper surface with a free surface. The model comprises two linear springs in series and an energy conservation equation to account for the restoring forces and deformations of the bubble and free surfaces, calculating contact time based on their elastic constants, deformations, and approach velocity. Results showed that for smaller bubbles (equivalent diameter less than 1.2 mm), the deformations of both the bubble and free surfaces play important roles in bubble bouncing on a free surface, while for larger bubbles, the contribution of the bubble deformation for the estimation of the contact time is much less than that from the free surface deformation.

MANICA *et al.* [25] modeled the rise and impact of bubbles at an initially flat but deformable ultra-clean liquid-air interface taking into account the buoyancy force, hydrodynamic drag, inertial added mass effect, and drainage of the thin film. They compared the results with literature experimental observations. The collision and bounce of such bubbles with a water/air, silicone oil/air, and ethanol/air interface were predicted with excellent agreement without any fitting parameters. According to the authors, it is essential to start with a model that can predict the approach speed correctly to model the bouncing behavior accurately.

FENG *et al.* [26] studied experimentally and numerically the dynamics of an air bubble bouncing at a liquid/liquid/gas (water/oil/air, respectively) interface, which they refer to as a compound interface. According to the author, when a bubble interacts with a thin layer of oil on top of bulk water, the oil layer modifies the interfacial properties and thus the entire process of bouncing and bubble bursting. The experiment results suggest that the oil viscosity mainly influences the pressure in the water film, hence the drainage flow between the oil layer and the bubble. They compared numerical results from a reduced-order mass–spring–damper model with experiments to describe the bounce of a droplet/bubble at the compound interface focused on the contact time and coefficient of restitution. The model was found to capture the contact time of the first impact quite well.

In view of the aforementioned considerations, a simplified model was proposed to predict bubble motion at the interface and the critical velocity for coalescence. This model overcomes limitations primarily influenced by the definition of an initial film thickness, considering the hydrodynamic criterion as the collision instant. Furthermore, it was estimated that physical parameters such as the decay ratio, added mass coefficient, and oscillation frequency obtained from experiments align for the

same number of bounces before coalescence.

Chapter 3

Coalescence Time of Ellipsoidal-Wobbling Bubbles at Surfactant-Free Interface: Experimental Analysis and Collision Criteria

This chapter presents the content of the first article, "Coalescence Time of Ellipsoidal-Wobbling Bubbles at a Surfactant-Free Interface: Experimental Analysis and Collision Criteria," which was published by the journal Chemical Engineering Science [27].

This work experimentally analyzed bubbles' coalescence with an air-water interface in the ellipsoidal-wobbling regime for different bubble approach velocities, encompassing the ranges of Eötvös, Weber, and Reynolds numbers of 2-3, 1-4, and 500-1100, respectively. We employed high-speed imaging to measure the bubbles' size, shape, velocity, coalescence time, and number of bounces at the interface. We investigated two criteria to determine the beginning of bubble-interface interaction ("collision"): the physical criterion, based on the distance between the bubble top surface and the interface, and the hydrodynamic criterion, based on the bubble velocity. Gamma distributions represent the coalescence times of bubbles at their terminal velocities well. We found a linear relationship between the coalescence time and the number of bounces. The hydrodynamic criterion was more consistent in representing our data on coalescence time.

3.1 Introduction

The coalescence of bubbles and droplets is important in many industrial and engineering applications, occurring in mass and heat transfer processes in bubble columns [2, 3], mineral flotation [6, 28], gas and oil transportation [7], wastewater treatment [29], among others [19, 30].

When two fluid particles, or a particle and an interface, approach each other ("collision"), a thin film of the continuous-phase fluid forms between them. For some conditions, this film drains to a critical thickness and breaks, joining the two interfaces leading to coalescence, in which the film drainage is considered the controlling factor [22, 31, 32]. From the bubble "collision", we can define two characteristic times: the iteraction time, that is, the time that bubbles remain close to each other, and the coalescence time, defined as the time interval from the formation of the thin film to its rupture, which is approximately equal to the film drainage time [33]. Since not all "collisions" result in coalescence, the conditional probability of coalescence after a "collision" is the coalescence efficiency. The ratio between the coalescence and interaction times is used to model the coalescence efficiency [2, 23]. These characteristic times are functions of several parameters such as fluid properties, "collision" forces or velocities [30, 33], impurity or surfactant concentration [34–36], mobility and deformation of the interfaces [37, 38], gravity [39], among others [40].

The simplest system for the study of coalescence involves the collision of bubbles with flat interfaces [13, 15–17]. The coalescence of bubbles with interfaces resembles an interplay between a small bubble and a bubble of infinite diameter for an infinite interaction time. This scenario always allows the drainage of the liquid film up to its critical thickness of rupture, leading to coalescence. Therefore, the probability of coalescence is always one, and any "collision" results in coalescence, as shown in Figure 3.1a. This behavior contrasts with bubble-bubble interactions, where the coalescence efficiency can be null under some conditions, as depicted in Figure 3.1b.

Many works analyzed the coalescence mechanisms. These works studied the liquid film thickness at the onset of drainage and just before rupture [16], the influence of the bubbles' approach velocity and the thickness of the film formed [15, 16, 41], the liquid film drainage rate using models based on lubrication theory [19, 22, 25, 42], the number of bounces [20, 25, 43], and the influence of concentration of surfactants or additives that affect the interface's mobility [34–36, 44, 45].

Some works specifically studied the coalescence between a rising bubble in still liquid and a flat gas-liquid interface without surfactants. KIRKPATRICK e LOCKETT [15] conducted experiments on bubble coalescence with flat interfaces to understand how approach velocity affects coalescence, finding that high approach velocities led to bubble bouncing at the interface. In contrast, low velocities resulted in rapid

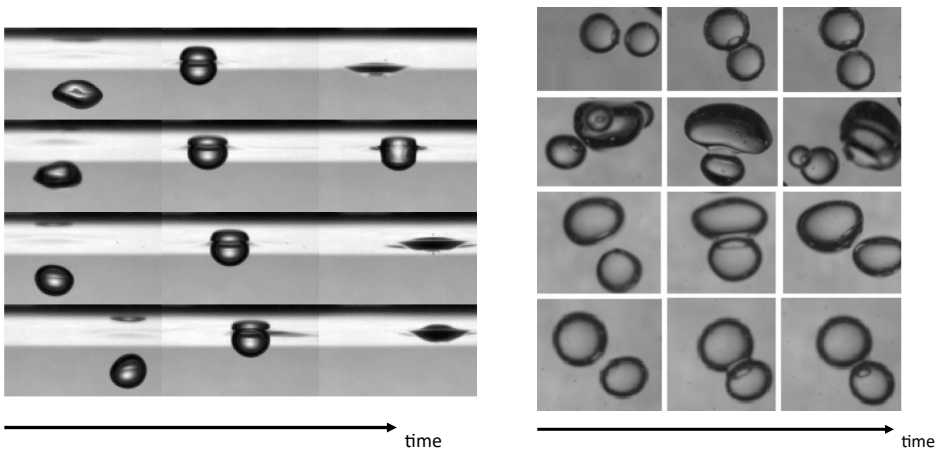

(a) (b)

Figure 3.1: Images of (a) bubbles bouncing and coalescing at the interface and (b) bubbles' collisions [1]. No coalescence was observed in the latter experiments.

coalescence. DOUBLIEZ [16] performed experiments using interference fringe shifts to measure the thickness of the thin liquid film between bubbles and interfaces, showing that it could reach the order of microns, concluding that the models based on the lubrication theory fail to predict the initial drainage stage. DOUBLIEZ [16] discovers a single relationship between coalescence time and Weber number in low-viscosity liquids, where the number of bounces was the most influential parameter. They determined a critical Weber number for coalescence in low-viscosity liquids that agreed well with the experimental and theoretical results of [18], whose values are $We_{crit} = 0.104$ and 0.117, respectively. SUÑOL e GONZÁLEZ-CINCA [13] observed air bubbles at an ethanol-air interface, concluding that the bouncing time increases linearly with the Weber number, and the height of the first bounce also depends linearly on the bubble equivalent diameter. ZAWALA e MALYSA [19] studied the influence of impact velocity and film thickness on coalescence time, finding that the higher the impact velocity, the larger the bubble shape deformation and the liquid film thickness, resulting in more intense bubble bouncing, consistent with earlier findings. SATO *et al.* [20] conducted experiments of bubbles bouncing at a free surface in pure water to verify the validity of a simple mass-spring model. The model agrees well with the experiments, and the time of the bubbles contacting the free surface was a function of the characteristic period of the oscillator.

Several works addressed the behavior of isolated bubbles ascending in a pool of a still liquid, predicting the regime from the Reynolds, Morton, and Eötvös dimensionless numbers [10, 11]. These dimensionless numbers, including the Weber number, are also used in analyzing coalescence [12, 13]. For instance, HORN *et al.* [14] presented a coalescence map for bubbles in surfactant-free aqueous electrolyte solutions, whose coordinates are the salt concentration and the bubble approach

velocity, based on the results compiled by KIRKPATRICK e LOCKETT [15] and [21], among others. The critical Weber number determined agrees with the result of $We_{crit} = 1$ presented by CHESTERS e HOFMAN [22] for two deformed bubbles approaching along their centerline. Their coalescence regime map defined the two regions separated by the critical Weber number as the rapid drainage and the elastic bounce regimes.

Although the literature on bubble coalescence at a gas-liquid interface is extensive, only some works have conducted experiments on bubble-interface coalescence in the ellipsoidal-wobbling regime. Therefore, more data on this process is necessary to model the phenomenon, given the diversity of theoretical assumptions and the lack of a precise definition of the initial drainage stage. Table 3.1 shows the experimental conditions carried out by KIRKPATRICK e LOCKETT [15], SANADA *et al.* [12], SUÑOL e GONZÁLEZ-CINCA [39], and ZAWALA e MALYSA [19].

Table 3.1 shows a need for experiments for bubbles of intermediate size (2.5-4.5 mm) in the literature. Therefore, in this work, we conducted experiments of 4 mm bubbles' coalescence with a flat, surfactant-free air-water interface.

We used advanced high-speed imaging techniques to measure bubble size, shape, velocity, and coalescence time [46]. We developed and reported new methods for determining the local bubble velocity and the uncertainties of the bubble image moments, which were used to obtain bubble size and position uncertainties. The Eötvös, Weber, and Reynolds numbers' ranges in our study are also shown in Table 3.1.

To calculate the coalescence time, we defined two "collision" criteria to determine the instant at which the bubble and interface begin their close contact, forming the thin liquid film: the physical criterion, based on the distance between the bubble's top and the static interface, and the hydrodynamic criterion, based on the bubble's instantaneous velocity.

This work structure follows. Section 2 details the materials and methods employed, providing a clear understanding of how we measured the fluid properties, set up flow visualization, and conducted the experiments. Section 3 presents the data analysis, covering image acquisition, processing, bubble data measurements, the definition of relevant dimensionless numbers, and estimating the uncertainty of image moments. Section 4 presents the configuration of the experimental data sets. Section 5 presents and discusses the results, while Section 6 provides our conclusions.

Table 3.1: Summary of literature review on bubble-interface coalescence experiments.

Author	Test section	Fluids	Conditions	d_e [mm]	Bubble Regime
KIRKPATRICK e LOCKETT [15]	A 3 in. diameter glass bell immersed in a water vessel Y_{int} = 4.5 to 35 mm	Air Water	T = 21±1°C Mo = O(10^{-11}) $We^{(*)}$ = 0.76 - 3.0 $Re^{(*)}$ = 500 - 985	5	Ellipsoidal and Wobbling
SANADA *et al.* [17]	Acrylic pool (15×15×40 cm) Y_{int} = 50 mm	Nitrogen Air/Silicone Oil	T = 20±3°C Mo = O(10^{-10}) to (10^{-4}) We = 0.02 - 3.4 Re = 1 – 100	0.3 - 1.66	Spherical and Ellipsoidal
SUÑOL e GONZÁLEZ-CINCA [13]	Methacrylate tank (25×25×25 cm) Y_{int} = 200 mm	Air Ethanol	T = 20±3°C Mo = O(10^{-9}) We = 0.01 - 3 Re = 5 – 300	0.1 - 2.0	Ellipsoidal
ZAWALA e MALYSA [19]	Square glass column Y_{int} = 1.8, 2.2, 4.0 and 300 mm	Air Water	T = 22±1°C Mo = O(10^{-11}) We$^{(*)}$ = 1.0 - 3.34 Re$^{(*)}$ = 263 - 600	1.0 - 1.6	Ellipsoidal
SATO *et al.* [20]	Acrylic tank (12×12×60) cm	Nitrogen Air/Water	T = 25.8 °C Mo = O(10^{-11}) We$^{(*)}$ = 0.08 - 1.44 Re$^{(*)}$ = 97 - 648	0.62 - 1.56	Ellipsoidal
Present work	Polymethyl methacrylate cell Inlet: 4×5 cm Outlet: 12×5 cm Y_{int} = 10 and 25 mm	Air Water	T = 23–25 °C Mo = O(10^{-11}) We = 1 - 4 Re = 500 - 1100 Eo = 2 - 3	4	Ellipsoidal and Wobbling

$^{(*)}$ They were estimated in the present work based on data from the original reference.

3.2 Materials and Methods

3.2.1 Materials

The properties of fluids were measured over the temperature range of 20 to 30 °C. The experiments utilized pure water as the continuous phase, produced by a Marte Pilsen-type distiller, filtered and demineralized. Its density was measured using an Anton Paar densimeter model DMA 4200M, with an accuracy of 10^{-4} g/cm^3. The viscosity was measured with a HAAKE MARS 40 rheometer, with a torque range of 20 - 200 nNm and a resolution of 0.1 nNm. Surface tension was measured by a KRUSS tensiometer, model K100C, using a Wilhelmy flat plate, with a deviation of 0.02 mN/m within a measured range of 1 to 2000 mN/m. Electrical conductivity was measured with a Metler Toledo conductivity meter model Seven Excellent, with a 0.001 μS/cm resolution. Ultra-pure water has a conductivity of 0.055 μS/cm at 25 °C. The density of the air, used as the dispersed phase, is calculated at sea level using a psychrometric chart.

Measured properties such as density, viscosity, and surface tension of the phases were correlated with models of one or two parameters capable of predicting fluid properties within the temperature range of 20 to 30 °C. The temperature of the liquid phase was measured with a digital thermometer with a resolution of 0.1 °C and expanded uncertainty of 0.13 °C for a coverage factor of 2. We used a Siberius digital hygrometer model HTC-2 with a resolution of 0.1 °C to measure room temperature and relative humidity, with measurement uncertainties of 0.30 °C and 1% RU, respectively, for a coverage factor of 2.

The data and models used to calculate the fluid properties are provided in the Supplementary Material 1. The standard uncertainties were calculated using Type A and Type B evaluation methods [47]. The water electrical conductivity was measured as 0.2 μS/cm at 23 °C.

The water and room temperatures were obtained from an average of four measurements taken during the experimental runs, which gave 24.40 ± 0.51 °C and 24.80 ± 0.68 °C, respectively. Their combined standard uncertainty include repeatability error, thermometer resolution, and data from a calibration certificate. The mean operating temperature was defined as the arithmetic average between the mean water and room temperatures.

Table 3.2 presents the properties such as density, viscosity, and surface tension between the phases with their uncertainties at a 95 % confidence level, calculated at the mean operating temperature of $\overline{T} = 24.60 \pm 0.43$ °C. The percent relative errors for the density and viscosity of the continuous phase, the surface tension, and the density of the dispersed phase are 0.70 %, 0.21 %, 0.31 %, and 0.34 %, respectively.

Table 3.2: Phase properties at $\overline{T} = 23.0 \pm 0.1$ °C.

ρ_C [kg/m^3]	ν_C [mPa s]	σ [mN/m]	ρ_D [kg/m^3]
997 ± 7	0.964 ± 0.002	65.2 ± 0.1	1.184 ± 0.001

3.2.2 Experimental Setup

We used high-speed imaging to calculate the bubble characteristics such as volume, equivalent diameter, and instantaneous velocity in the stagnant liquid. The bubbles were filmed in the frontal plane of the test section of the experimental setup built by COELHO [9] to observe coalescence. Figure 3.2 presents a schematic illustration of the experimental setup. The unit was built to acquire experimental data on the coalescence efficiency of upward moving bubbles in a downward divergent flow channel. The experimental setup was adapted to experiments on bubble coalescence with a flat interface in a liquid pool. A capillary tube with a 2 mm inner diameter was vertically positioned at the bottom of the test section. This tube was connected to a 1 ml syringe pump to guarantee slow air injection and achieve a single bubble formation at its tip. The syringe pump was fabricated using a Stratasys Objet1000 Plus 3D printer. Its injected volume per step was calibrated by adjusting the mean flowrate calculated based on the difference in mass and the actuation speed for the syringe pump, driven by an Arduino code. The equipment used in the calibration included a digital thermometer with a resolution of 0.1°C, two 50 ml beakers, one 100 ml beaker (both cleaned and dried), and a BEL Engineering precision balance with a resolution of 1 mg.

The equipment used for the image acquisition consisted of a Phantom Speed-Sense Lab M310 camera, a stroboscopic LED light, and a synchronizer/timer box. Illumination was homogenized using a diffuser sheet. The camera has a maximum acquisition rate of 3260 frames per second (fps) with an image resolution of 1280 $\times$ 800 pixels. Its sensor size is 25.6 mm $\times$ 16.0 mm of complementary metal-oxide-semiconductor (CMOS) type, allowing for monochrome or color imaging with 12-bit depth. Its pixel size is 20 $\times$ 20 µm. The camera was equipped with an AF Micro-Nikkor lens with a focal length of 60 mm and an aperture range of 2.8 to 32. The timer box was driven by a National Instruments counter/time board model PCIe-6612, which synchronizes the camera and LED to a computer featuring an Intel Xeon processor 2.5 GHz (8 CPUs) and 16 GB of RAM. Software Dynamic Studio 2015a of DANTEC Dynamics was employed to configure acquisition image parameters such as interframe, exposure, and illumination times.

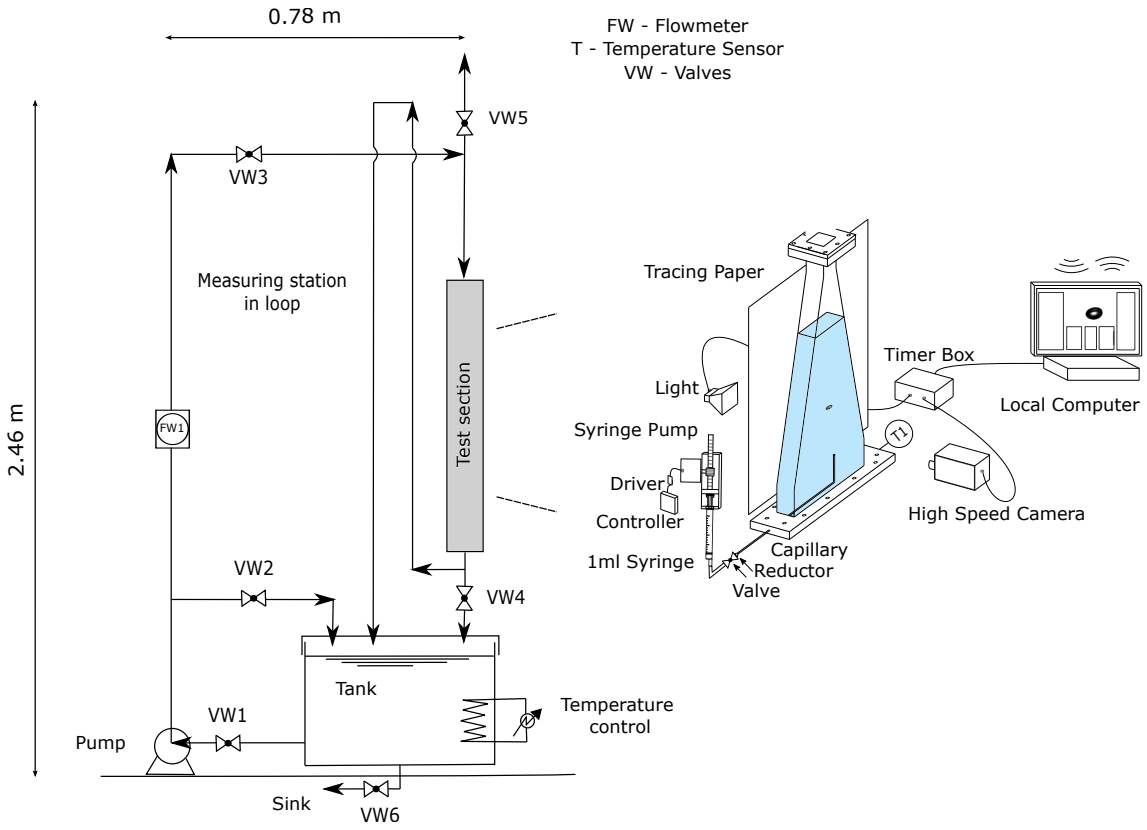

Figure 3.2: Experimental Setup.

3.2.3 Experimental Procedure

Before each experimental campaign, the coalescence cell was removed from the apparatus, cleaned, and then rinsed three times with the same water used in the experiments. Next, we filled the test section with water, and slightly opened the VW4 valve in Figure 3.2 to allow water to be slowly discharged into the tank to position the interface. We positioned the interface at the desired height above the tip of the capillary tube. During the experiments, the valve VW4 remained closed. Reference strips were placed on the sidewalls of the coalescence cell to facilitate the interface positioning. We took care to handle water without contaminating it. A water sample from each experiment was stored and dated for properties measurements. The duration of each experimental set, as well as the room and water temperatures, were recorded. The mean operating temperature was determined.

The camera's field of view was adjusted to capture the bubble detachment, ascension, collision, and coalescence with the interface. The focus and effective aperture of the diaphragm lens were adjusted manually. The distance between the object and the camera must exceed the lens' minimum focal distance. Acquisition parameters were synchronized with the timer box and modified using the Dynamic Studio software. We used an illumination time shorter than the exposure time to prevent pixel saturation, thus reducing the motion blur [46]. The software's graphical interface

allowed for a preview visualization of the camera view with the adjusted parameters. If saturation occurred, we decreased the diaphragm aperture or the exposure time.

Each experimental set comprises several runs, each providing images with the chosen number of frames in single-frame mode at the selected acquisition frequency, given in frames per second (fps). In the syringe pump software driver, we configured the number of steps and the actuation frequency of the pump in steps per second (steps/s).

3.3 Data Analysis

The image-based measurement procedure comprises three stages: image acquisition, digital processing, and measurement extraction. The first stage (acquisition) is sensitive to external parameters such as vibrations, light flicker, focus, and hardware characteristics like spatial resolution, shutter, and lens distortion. These factors influence the second stage (image processing), which propagates these effects to the measurements resulting from the third stage [48]. The following subsections describe the image acquisition, the image processing, and the measurements' extraction for the bubbles' characteristics.

3.3.1 Image Acquisition

The first step in analyzing an image is calibration. For calibration, we cleaned a 30 cm transparent ruler and positioned it immersed in the water at the center of the cell aligned with the outlet of the capillary tube tip, as shown in Figure 3.3a. The points O, A, and B in Figure 3.3a were set respectively at the origin of the image coordinate plane xy and at two positions separated by a known absolute length, L, provided by the calibration target. Figure 3.3b shows that the capillary tube and interface appear black, with a gradual transition from white to black for the latter due to interface refraction.

From the number of pixels in the image calibration segment, N_L, and the absolute distance in mm, L, we calculated the scale factor as follows:

We calculated the scale factor as the ratio of the number of pixels in the image calibration segment and the absolute distance in mm, such that:

$$\kappa = \frac{N_L}{L} \tag{3.1}$$

A new $x'y'$ coordinate system was defined for each bubble, whose origin is the initial position of its barycenter, given by the coordinates in pixels (x_{c_0}, y_{c_0}). The

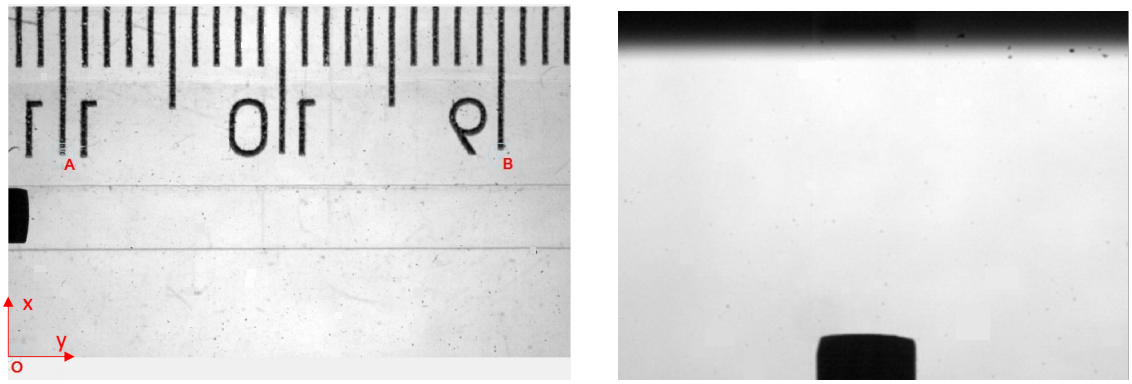

(a) (b)

Figure 3.3: Image analysis: (a) estimation of the scale factor for calibration, and (b) image of the interface and capillary tube tip.

positions in the $x'y'$ plane are:

$$x' = x_c - x_{c_0} \ ; \ y' = y_c - y_{c_0} \tag{3.2}$$

Once the conversion factor from pixel to mm is known, the position of a pixel in mm in the $x'y'$ plane of the image, representing the horizontal and vertical axis, respectively, is given by:

$$X' = \frac{x'}{\kappa} \ ; \ Y' = \frac{y'}{\kappa} \tag{3.3}$$

3.3.2 Image Processing

The intensity of a pixel, $I(x, y)$, in a grayscale image, is given by an integer value from 0 to $(2^{bits} - 1)$, where $bits$ is the number of bits uses to define each pixel, that is, the number of represented grayscale tones. The values of x and y are the pixel positions in the image coordinate plane, also represented by integer values, with $x = 1, ...N_x$ and $y = 1, ..., N_y$, for images with a resolution of $N_x \times N_y$ pixels. For instance, in 12 bits, the image can store up to 4096 levels of gray, where usually black corresponds to 0 and white to 4095. In the case of a binary image, there are only two values for each pixel, 0 and 1, corresponding to black and white, respectively.

Bubble image processing

Figure 3.4a demonstrates the initial manual image filtering conducted for every acquired image set. This step is crucial as it delineates the phenomenon of interest from the detachment of the bubble from the capillary to its coalescence with the interface. The detachment corresponds to the neck break that connects the bubble to the capillary, while the coalescence corresponds to the rupture of the liquid film between the bubble and the interface. Following this, a series of sequential oper-

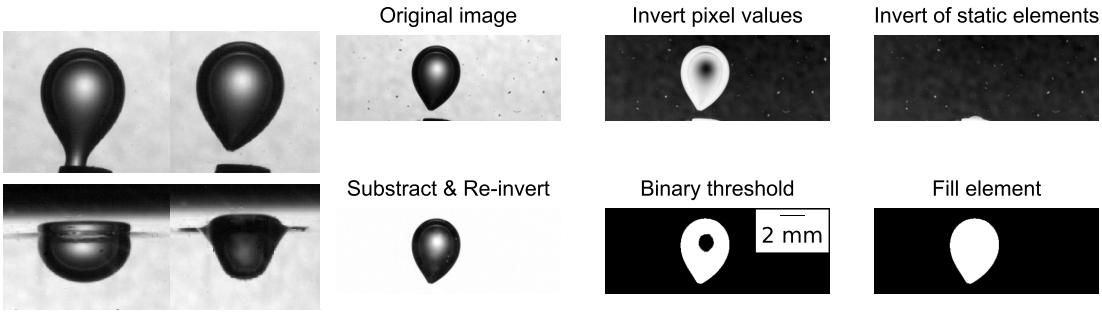

Figure 3.4: Image processing: (a) bubble detachment and coalescence, and (b) sequence of steps done on the image processing.

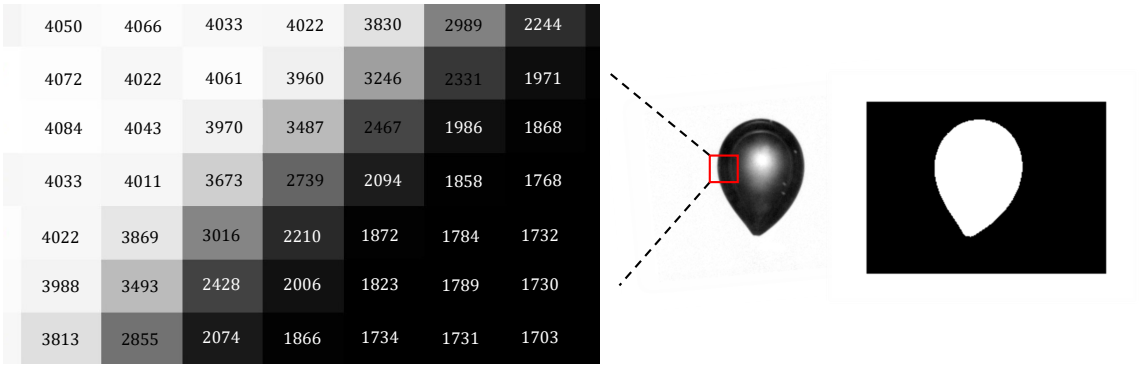

Figure 3.5: Pixel intensity values near to bubble interface and resulting binary image.

ations were systematically applied to each image to identify the bubbles and their characteristics. The sequence of image processing steps and the resulting image at each stage are clearly depicted in Figure 3.4b.

We employed the following image operations: *pixel inversion*, *invert image subtraction* to eliminate static elements, *pixel inversion* to return to the values of $I(x, y)$ of the original image, *image binarization* using Eq. 3.4 with the threshold intensity, I_{thresh}, determined by Otsu's method [49], *bubble filling* to eliminate the dark region in its center, and *image masking* to remove uninteresting areas or elements defined in a mask from the image set, particularly reflections of the bubble when it is close to the interface.

$$I(x,y) = \begin{cases} 0 & , \text{ if } I(x,y) > I_{thresh} \\ 1 & , \text{ otherwise} \end{cases} \tag{3.4}$$

Figure 3.5 shows the intensity values close to the bubble interface for a 12-bit grayscale image on the left and the resulting image of the above processing that generates the filled binary image with $I = 1$ inside the bubble on the right.

The algorithm also executes the following steps to determine the uncertainties in the image moments due to the bubble image binarization.

- Using the final binarized image of the bubble, it calculates the number of pixels inside the bubble, N_b, and outside, N_{out}, as being the difference between the total number of pixels ($N_x \times N_y$) and N_b.

- Using the original grayscale image of the isolated bubble, it determines the ΔI_{thresh} as 5 % of the difference between the mean intensity values inside, I_b, and outside the bubble, I_{out}, such that $\Delta I_{thresh} = 0.05|I_{out} - I_b|$, where $I_{out} = 1/N_{out} \sum_{k=1}^{N_{out}} I_k$ and $I_b = 1/N_b \sum_{k=1}^{N_b} I_k$.

- It determines the perturbed thresholds of intensity $I_{thresh} + \Delta I_{thresh}$ and $I_{thresh} - \Delta I_{thresh}$ and the resulting values of N_b^+ and N_b^-, respectively

The algorithm calculates the zeroth and first image moments of the binary image from their definitions:

$$m_{ij} = \iint_{\mathbb{D}} x^i y^j I(x,y) dxdy = \sum_{k=1}^{N_b} x_k^i y_k^j \Delta x \Delta y, \quad (ij) = (00), (10), (01) \tag{3.5}$$

where $\Delta x = \Delta y = 1$ in pixel units. The zero-order moment, m_{00}, corresponds to the area of the bubble in pixel units, whose barycenter in the xy coordinates is:

$$x_c = \frac{m_{10}}{m_{00}} \ ; \ y_c = \frac{m_{01}}{m_{00}} \tag{3.6}$$

Then, it computes the second-order central moments of the binary distribution, $\mu_{ij}, i + j = 2$, from:

$$\mu_{ij} = \iint_{\mathbb{D}} (x - x_c)^i (y - y_c)^j I(x,y) dxdy = \sum_{k=1}^{N_b} (\Delta x_k)^i (\Delta y_k)^j \Delta x \Delta y \tag{3.7}$$

where $\Delta x_k = x_k - x_c$ and $\Delta y_k = y_k - y_c$.

Finally, the algorithm recalculates the imagem moments using the perturbed threshold intensities $I_{thresh} + \Delta I_{thresh}$ and $I_{thresh} - \Delta I_{thresh}$. Section 3.3.5 explains the calculation of the moments' uncertainties due to the binarization process.

Besides, for each bubble image, we also determined the coordinates of the lower $(x,y)_{bottom}$ and upper $(x,y)_{top}$ corners of the rectangle that contains the bubble projected area.

Gas-liquid interface image processing

The interface image processing follows a procedure similar to bubble image processing. The procedure begins with binarizing the original grayscale image using a threshold determined by Otsu's method, as given in Eq. 3.4. This results in a white

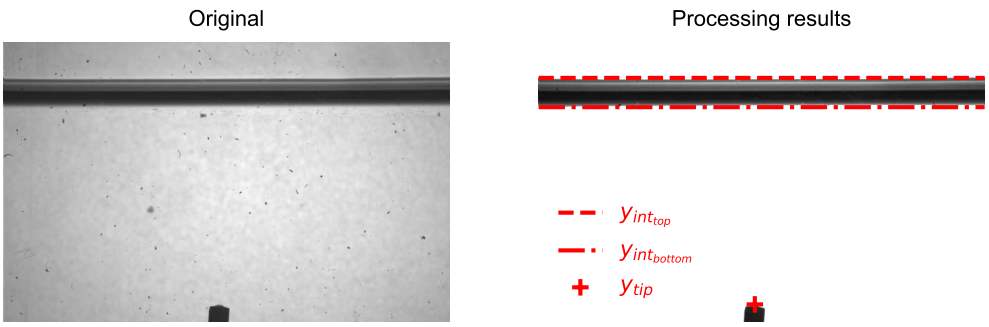

Figure 3.6: Interface image processing

interface on a black background. Image masking is then applied to remove all image features except the capillary tube and the interface.

To determine the interface vertical position, the coordinates in pixels of the lower ($y_{int_{bottom}}$) and upper ($y_{int_{top}}$) corners of the rectangle containing the interface projected area are determined. Thus, we defined the vertical interface position as:

$$y_{int} = \left(y_{int_{top}} + y_{int_{bottom}}\right)/2 \tag{3.8}$$

Figure 3.6 shows the resulting image of the interface processing, indicating the interface's top and bottom positions and the vertical position of the capillary tube tip in pixel units.

The rising height is the vertical distance between the interface position and the capillary tube tip calculated as:

$$h_{ris} = y_{int} - y_{tip} \tag{3.9}$$

We used Eqs. 3.1 and 3.3 to calculate the vertical positions of the interface, Y_{int}, and capillary tube tip, Y_{tip}, and the rising height, H_{ris}, in mm. We assumed the uncertainty of the interface position as half the difference between the top and bottom positions, determining the uncertainty in the rising height from error propagation. The distance from the capillary tip to the interface was carefully selected to ensure that the bubble reached its terminal velocity without developing the helical motion observed in previous experiments. Furthermore, the 50 mm thickness of the test section had no noticeable effect on movement development.

3.3.3 Bubble Data Measurements

Bubble volume and shape

Assuming that the bubble is a spheroid, the second-order central moments calculated using Eq. 3.7 were used to calculate its major and minor semi-axes and the

orientation of the major semi-axis with the horizontal [50]. The major, a, and minor, b, semi-axes of an ellipse are given by:

$$a = \left[\frac{16\lambda_1^3}{\pi^2\lambda_2}\right]^{1/8} \tag{3.10}$$

$$b = \left[\frac{16\lambda_2^3}{\pi^2\lambda_1}\right]^{1/8} \tag{3.11}$$

where λ_1 and λ_2 are the eigenvalues of the covariance matrix of the second-order central moments, given by:

$$\lambda_{1,2} = \frac{\mu_{20} + \mu_{02}}{2} \pm \frac{\sqrt{4\mu_{11}^2 + (\mu_{20} - \mu_{02})^2}}{2}, \lambda_1 > \lambda_2 \tag{3.12}$$

The angle of the major semi-axis with the x-coordinate axis is calculated as follows:

$$\theta = \frac{1}{2}\tan^{-1}\left(\frac{2\mu_{11}}{\mu_{20} - \mu_{02}}\right) \tag{3.13}$$

We computed the inverse tangent function in the above equation using the function $atan2(2\mu_{11}, \mu_{20} - \mu_{02})$ as it gives θ in the correct quadrant.

The complete analysis of the image moments and its interpretation using the elliptical shape assumption is presented in the Supplementary Material 1.

The bubble's projected area approximated as an ellipse was calculated from its major and minor semiaxis as:

$$A_{ellipse} = \pi ab \tag{3.14}$$

The bubble's volume was approximated to that of an oblate or prolate spheroid, depending on the orientation of its semi-axes, as follows:

$$V = \frac{4\pi}{3}abc \tag{3.15}$$

where

$$c = \begin{cases} a, & \text{if } -45° < \theta < 45° \\ b, & \text{otherwise} \end{cases} \tag{3.16}$$

The bubble's equivalent diameter is defined by:

$$d_e = \sqrt[3]{6V/\pi} \tag{3.17}$$

To evaluate mean values for area, volume, and velocity of each bubble with minimal interference from its detachment and "collision" with the interface, we used just the images acquired when the bubble barycenter was in middle half of the available liquid height, that is, $Y'_c \in [Y'_{min} + \Delta Y', Y'_{max} - \Delta Y']$, where $Y'_{min} = 0$,

$Y'_{max} = \max\{Y'_{top}\}$, and $\Delta Y' = 0.25 Y'_{max}$.

Considering N images, the bubble's mean area and volume were calculated using the following weighted average:

$$\overline{\varphi} = \frac{\sum_{n=1}^{N} \varphi_n \omega_n}{\sum_{n=1}^{N} \omega_n} \tag{3.18}$$

where φ_n is the variable value, and ω_n is the corresponding weight given by the reciprocal of the experimental measurement uncertainty $\omega_n = 1/u(\varphi_n)$. The sample standard deviation was also calculated as $s_\varphi = \sqrt{\frac{\sum_{j=1}^{N}(\varphi_j - \overline{\varphi})^2}{N-1}}$. The mean equivalent diameter was determined from the bubble's mean volume using Eq. 3.17.

The mean velocity was estimated in as the slope of the linear model:

$$Y' = \overline{U}_{Y'} t + Y'_0 \tag{3.19}$$

whose parameters were adjusted using the Orthogonal Distance Regression (ODR) method [51].

To evaluate the accuracy and repeatability of the $\overline{d}_e$ and $\overline{U}_{Y'}$ data for each experimental data set, we determined the arithmetic means of their determination errors at the 95% confidence level and their standard deviations, both expressed as percentages of the corresponding mean values.

Bubble's instantaneous vertical velocity

The vertical component of the bubble's velocity at a given time instant, t, is obtained by adjusting the linear model $Y'_c(t) = \zeta'_0 t + \zeta'_1$ to a (t, Y'_c) data set in a time interval around t. The ζ'_0 and ζ'_1 coefficients were also estimated using the ODR method, being $U_{Y'_j} = \zeta'_0$. The data set is symmetrically distributed around t in a moving window given by $\Delta t = 2n\Delta t_{min}$, where $\Delta t_{min} = 1/f_{acq}$. The window contains $2n+1$ points from $Y'(t_j - n\Delta t_{min})$ to $Y'(t_j + n\Delta t_{min})$, or Y'_{j-n} to Y'_{j+n}, considering $Y'_j = Y'(t_j)$.

For the initial ($j < n$) and the final ($j > N - n$) time instants, the fitting of the data sets in the interval from Y'_0 to Y'_n, and from Y'_{N-n} to Y'_N, respectively, determines the instantaneous velocity. The first and the last velocity values were calculated by forward and backward finite differences, respectively.

We assumed that there is an agreement between the instantaneous velocity calculated using two different windows (Δt_1 and Δt_2) when there is a large percentage (>95%) of their points satisfies the following condition:

$$\frac{|U_{Y'}(t, \Delta t_2) - U_{Y'}(t, \Delta t_1)|}{[u[U_{Y'}(t, \Delta t_2)]^2 + u[U_{Y'}(t, \Delta t_1)]^2]^{0.5}} < 1 \tag{3.20}$$

Estimation of coalescence time

The drainage of a thin liquid film formed when the bubble and the gas-liquid interface are very close to each other controls the coalescence time. Since the thin film thickness is of tenths of micrometers [16], image analysis cannot resolve it. Thus, we defined the coalescence time as the time interval between the instant when the bubble finally coalesces with the interface, t_f, and the time, t_{coll}, which is the onset of formation of the thin liquid film between the interfaces. Thus, the coalescence time is defined by:

$$t_c = t_f - t_{coll} \tag{3.21}$$

Since the image analysis cannot resolve the liquid film thickness, to determine t_{coll}, we defined two criteria for its onset: the first time the bubble gets close to the gas-liquid interface, that is, at the first "collision." The physical collision criterion (PCC) defines t_{coll} when, for the first time, the distance between the bubble's top surface and the interface is null, considering its uncertainty:

$$t_{coll} = t_j \quad \text{if } h_{f_j} - u(h_{f_j}) \leq 0 \tag{3.22}$$

where h_f at the time instant t_j is the distance between positions of the top surface of the approaching bubble, Y_{top}, and the static interface, Y_{int}, given by:

$$h_{f_j} = Y_{int} - Y_{top_j} \tag{3.23}$$

Image processing estimated the bubble's top surface and static interface positions. We assumed the interface position as the average between the top and bottom interface positions, that is:

$$Y_{int} = (Y_{int_{top}} + Y_{int_{bottom}})/2 \tag{3.24}$$

The hydrodynamic collision criterion (HCC) defines t_{coll} when, for the first time, the bubble's vertical velocity is null considering its uncertainty:

$$t_{coll} = t_j \quad \text{if } U_{y_j} - u(U_{y_j}) \leq 0 \tag{3.25}$$

The mean and standard deviation of the t_c data for several bubbles were calculated directly from the experiments and by assuming a two-parameter (α, β) gamma cumulative distribution of the form:

$$F(t_c) = \frac{\gamma(\alpha, \beta t_c)}{\Gamma(\alpha)} \tag{3.26}$$

where $\bar{t}_c = \alpha/\beta$ and $s(t_c) = \sqrt{\alpha/\beta^2}$. We calculated the experimental cumulative density function as:

$$\hat{F}(t_c) = \frac{1}{(N+1)} \sum_{\substack{i=0 \\ t_{c_i} < t_c}}^{N} 1 \tag{3.27}$$

and used it to determine α and β with their uncertainties at a 95 % confidence level using the ODR method.

3.3.4 Relevant Dimensionless Numbers

In this study, the relevant dimensionless numbers are Eötvös, Morton, Weber, and Reynolds, defined as:

$$Eo = \frac{\Delta\rho g \overline{d}_e^2}{\sigma} \tag{3.28}$$

$$Mo = \frac{g\nu_C^4(\rho_C - \rho_D)}{\rho_C^2\sigma^3} = \frac{g\nu_C^4\Delta\rho}{\rho_C^2\sigma^3} \tag{3.29}$$

$$We = \frac{\rho_C \overline{U}_y^2 \overline{d}_e}{\sigma} \tag{3.30}$$

$$Re_d = \frac{\rho_C \overline{U}_y \overline{d}_e}{\nu_C} \tag{3.31}$$

3.3.5 Estimation of uncertainty of the image moments.

Applying the generalized Reynolds transport theorem in the continuous formulation of the moments to calculate the variation of the moments m_{ij}, we have:

$$\delta\left(\iint_{\mathbb{D}} x^i y^j dxdy\right) = \iint_{\mathbb{D}} \delta(x^i y^j) dxdy + \iint_{\partial\mathbb{D}} x^i y^j (\delta\mathbf{r}_s \cdot \hat{\mathbf{n}}) dS \tag{3.32}$$

where $\partial\mathbb{D}$ is the boundary of $\mathbb{D}$, $\mathbf{r}_s$ is the position vector over $\partial\mathbb{D}$, $\hat{\mathbf{n}}$ is the outward unit vector normal to $\partial\mathbb{D}$, and S is the arc lenght along $\partial\mathbb{D}$. The last term in Eq. 3.32 is the contribution of the size variation of $\mathbb{D}$ in the moment variation.

The discrete form of Eq. 3.32 applied to a bubble with N_b pixels is:

$$\delta\left(\sum_{k=1}^{N_b} x_k^i y_k^j\right) = \sum_{k=1}^{N_b} \delta(x_k^i y_k^j) + \delta\left[\sum_{k=1}^{N_b} x_k^i y_k^j\right] \tag{3.33}$$

The uncertainty of m_{ij} comes from Eq. 3.33 as:

$$u\left(m_{ij}\right) = \sqrt{u^2\left(m_{ij}^{(\mathbb{D})}\right) + u^2\left(m_{ij}^{(\partial\mathbb{D})}\right)} \tag{3.34}$$

where

$$u^2\left(m_{ij}^{(\mathbb{D})}\right) = \sum_{k=1}^{N_b} u^2(x_k^i y_k^j), \tag{3.35}$$

and $u\left(m_{ij}^{(\partial\mathbb{D})}\right)$ is the uncertainty corresponding to the last term of Eq. 3.33. We approximated this term using the bubble's images with N_b^+ and N_b^- pixels, determined by the threshold perturbation analysis of the binarization process, shown in Section 3.3.2, giving:

$$u\left(m_{ij}^{(\partial\mathbb{D})}\right) = \frac{1}{2}\left[m_{ij}^{N_b^+} - m_{ij}^{N_b^-}\right] \tag{3.36}$$

where, in pixel units, we defined

$$m_{ij}^{N_b^\pm} = \sum_{k=1}^{N_b^\pm} x_k^i y_k^j \tag{3.37}$$

Using the uncertainties of the pixels' positions, $u(x_k)$ and $u(y_k)$, we can write:

$$u\left(x_k^i y_k^j\right) = x_k^i y_k^j \sqrt{\left(\frac{iu\left(x_k\right)}{x_k}\right)^2 + \left(\frac{ju\left(y_k\right)}{y_k}\right)^2} \tag{3.38}$$

which, by assuming that $u\left(x_k\right)$ and $u\left(y_k\right)$ are equal to the sensor's positioning uncertainty, $u\left(x\right)$, becomes:

$$\frac{u\left(x_k^i y_k^j\right)}{x_k^i y_k^j} = u(x)\left[\left(\frac{i}{x_k}\right)^2 + \left(\frac{j}{y_k}\right)^2\right]^{1/2} \tag{3.39}$$

Since $u(x)$ is quite small and the factor between brackets in Eq. 3.39 is also small for the lower order moments as $i << x_k$ and $j << y_k$, we neglected $u^2\left(m_{ij}^{(\mathbb{D})}\right)$ in Eq. 3.34, obtaining:

$$u\left(m_{ij}\right) = u\left(m_{ij}^{(\partial\mathbb{D})}\right) = \frac{1}{2}\left[m_{ij}^{N_b^+} - m_{ij}^{N_b^-}\right] \tag{3.40}$$

Similarly, we approximated the uncertainties of the central moments as:

$$u\left(\mu_{ij}\right) = u\left(\mu_{ij}^{(\partial\mathbb{D})}\right) = \frac{1}{2}\left[\mu_{ij}^{N_b^+} - \mu_{ij}^{N_b^-}\right] \tag{3.41}$$

where, in pixel units, we defined

$$\mu_{ij}^{N_b^\pm} = \sum_{k=1}^{N_b^\pm} (\Delta x_k)^i (\Delta y_k)^j \tag{3.42}$$

Appendix 3.A gives details on the evaluation of the uncertainties of all bubble's

characteristics, derived quantities, and dimensionless numbers described in Sections 3.3.3 and 3.3.4.

3.3.6 Numerical procedure

We implemented all image analysis and data processing in Python using some libraries: OpenCV (version 4.6.0.66) for thresholding and binarization, NumPy (version 1.23.1) and Pandas (version 1.4.3) for handling data arrays and data frames, SciPy (version 1.9.0) for performing regression using the ODR method [51], and Matplotlib (version 3.5.2) for generating graphics.

We implemented the algorithm to process an image to obtain the binarized bubble image, determine its moments, calculate the perturbation to the binarization threshold, and determine the moments' uncertainties by recalculating the moments of binary bubble images obtained using perturbed thresholds. We validated the algorithm against images with known moments.

We also implemented the algorithm to determine the bubble's local vertical velocity using the bubble barycenter positions in a set of consecutive frames in a moving time window and the ODR package for model fitting.

3.4 Experimental data sets

We performed experiments using different camera acquisition frequencies, pump actuation speeds, and image resolutions. We organized the experimental runs into different data sets to determine the bubble characteristics, coalescence time, and number of bounces. For all experimental data sets, we employed a micro-Nikkor lens with a focal length of 60 mm, an effective aperture of $f/D = 16$, and an exposure time of 50 μs. The image resolution was 1280 $\times$ 800 pixels, $N_{frames} = 2500$ in single frame mode and $N_{steps} = 212$. For 212 steps in the syringe pump, the injected volume was $40.4 \pm 1.5\mu$l, calculated by the pump volumetric calibration:

$$V_{inj} = N_{steps} R_v \tag{3.43}$$

where $R_v = 0.19 \pm 0.01$ μl/step is the pump volumetric resolution for the 1 ml syringe. The injected volume at each experimental run generated a unique bubble with an equivalent diameter of approximately 4.26 mm.

Table 3.3 lists other configurations used for the different data sets and gives the values for the scale factor. The reader should note that the scale factor error is approximately 3% for all experimental data sets. One of the configurations in Table 3.3 is the time delay between the activation of the syringe pump (first action) and the camera trigger (second action), which was necessary to capture the bubble's

Table 3.3: Configurations of the experimental data sets.

Configurations	Data Sets		
	I	II	III
Runs	1 – 30	31 – 35	36 – 40
f_{acq} (fps)	500	1000	1000
f_{pump} (steps/s)	50	10	10
Delay (s)	1.5	21.0	21.0
κ (px/mm)	23.0 ± 0.7	22.5 ± 0.6	49.9 ± 1.4
T_{op} (°C)	23.7 ± 0.3	23.0 ± 0.1	23.0 ± 0.1

detachment, ascension, and coalescence with the interface. The mean operational temperature for all experiments was in the 23-25 °C range. Table 3.3 lists the T_{op} values for data sets I, II, and III.

Appendix 3.B compares bubble volume via pump calibration and image processing for different pump actuation and acquisition frequencies. Results show that the mean bubble volume is independent of the injection flow rate up to 200 steps/s.

3.4.1 Configurations of the experimental data sets

For data set I, the total acquisition time was 5 s, and the injection time was 4.24 s. Therefore, the time delay of approximately 1.5 s allows for measuring coalescence times up to 2.26 s, which is the difference between the total acquisition time and the injection time plus the time delay.

To measure the bubble characteristics better, we reduced the pump actuation frequency by five times and increased the image acquisition frequency by twice in experimental data set II. For this data set, the total acquisition time was 2.5 s, and the injection time was 21.2 s. Therefore, a delay of approximately 21.0 s was necessary, allowing recording up to 2.3 s of the phenomenon.

We conducted experimental data set III to analyze the bubbles' bouncing at the interface with the highest possible resolution of our equipment by using the minimum focal length and rotating the camera 90 degrees to maximize the number of pixels vertically. The scale factor obtained was almost double that of previous experiments. Additionally, we decreased the distance between the interface and the injection tube to obtain bubble approaching velocities lower than their terminal velocity.

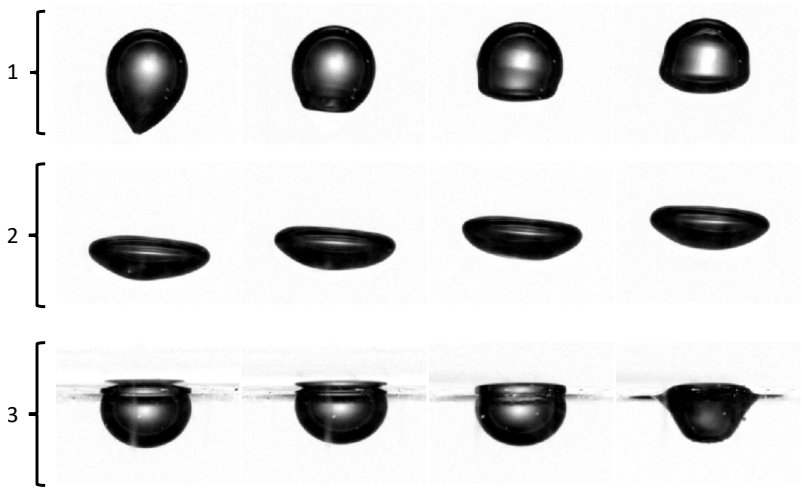

Figure 3.7: Bubble behavior in coalescence experiments: 1 - Detachment, 2 - Ascension, 3 - Bouncing and coalescence.

3.5 Results and Discussion

The Supplementary Material 1 lists the results for the bubble characteristics, dimensionless numbers, and coalescence times of each run of experimental data sets I, II, and III.

3.5.1 Bubble behavior

Figure 3.7 illustrates three stages of bubble behavior after detachment from the capillary until coalescence. The first stage occurs immediately after the detachment, where the lower part of the bubble moves much faster than the rest due to the action of the interfacial forces. In the second stage, the bubble deforms as it ascends through the fluid, assuming approximately the shape of a spheroid. The final stage involves the bubble's interaction with the interface, where its shape is approximately a spherical cap that oscillates and slides at the interface until coalescence. Furthermore, the interface deforms and is pushed upwards due to the bubble's presence.

3.5.2 Image Processing Validation

Static Interface Position

Table 3.4 presents the results of the image processing applied to images of the static air-water interface from experimental data sets I, II, and III, determined as described in Section 3.3.2. Table 3.4 lists the values for $Y_{int_{top}}$, $Y_{int_{bottom}}$, Y_{int}, Y_{tip} and H_{ris}, which are the vertical positions of the top, bottom and middle of the interface, the tip of the capillary tube, and the rising height. All vertical positions represent

Table 3.4: Static interface processing results.

Set	$Y_{int_{top}}$ [mm]	$Y_{int_{bottom}}$ [mm]	Y_{int} [mm]	Y_{tip} [mm]	H_{ris} [mm]
I	27.7 ± 0.1	26.5 ± 0.1	27.1 ± 0.6	2.11 ± 0.02	25.0 ± 0.6
II	28.4 ± 0.1	27.9 ± 0.1	28.1 ± 0.3	3.18 ± 0.02	24.9 ± 0.3
III	9.89 ± 0.01	8.37 ± 0.01	9.1 ± 0.8	1.17 ± 0.01	8.0 ± 0.8

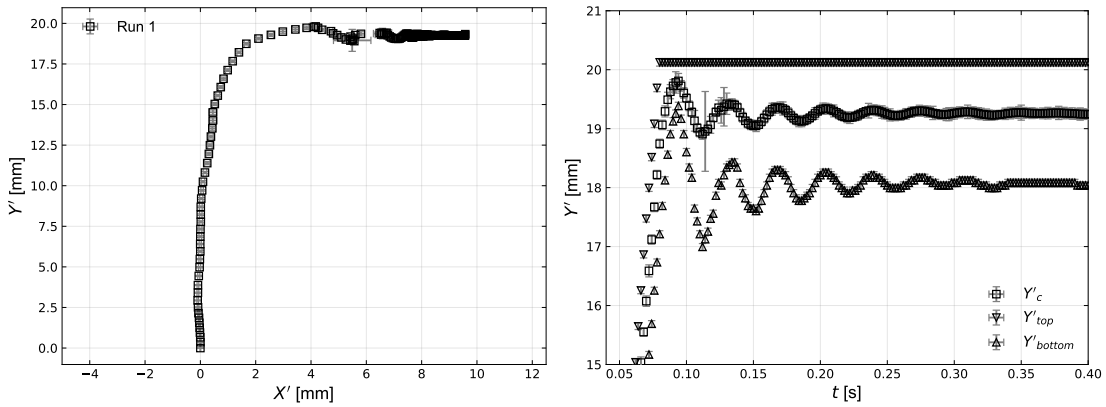

(a) X'_c and Y'_c (b) Y'_c, Y'_{bottom}, Y'_{top}

Figure 3.8: Bubble's ascension: (a) trajectory of bubble barycenter, and (b) vertical positions of the bubble's centroid, top and bottom surfaces. Run 1 of experimental data set I.

heights from the bottom of the image.

Bubble volume and velocity

We chose run 1 of the experimental data set I from Table 3.3 to exemplify the determination of the trajectories, volume, mean ascension velocity, and the vertical component of the instantaneous velocity of the rising bubbles.

Figure 3.8a shows the bubble's trajectory through the X' and Y' coordinates of its centroid, while Figure 3.8b depicts the vertical positions of the bubble' s centroid, Y'_c, top surface, Y'_{top}, and bottom surface, Y'_{bottom}. As observed, the bubble follows an almost rectilinear trajectory until it approaches the interface. After the "collision", the bubble oscillates and slides at the interface, as shown by the displacement of Y'_{bottom} and the horizontal centroid position, X'_c, respectively.

Figure 3.9 presents the results for the bubble's volume and ascension velocity of run 1. Figures 3.9a and 3.9b represent $V \times Y'_c$ and $Y'_c \times t$ data, respectively, where V came from Eq. 3.15. The model given by Eq. 3.19 determined $\overline{U}_{Y'}$ from Figure 3.9b data. The ODR method provides the standard deviation of $\overline{U}_{Y'}$ and its error at a 95 % confidence level.

For all runs of data set I, Figure 3.10a compares the mean bubble projected area

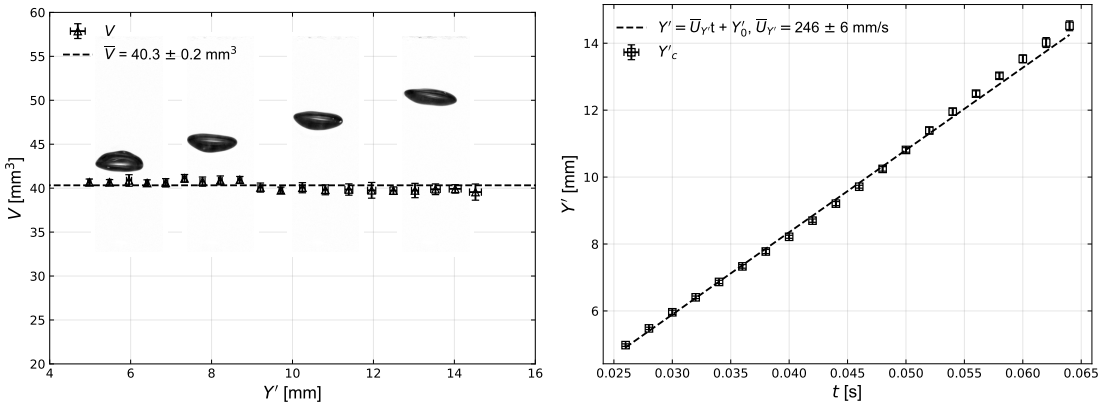

(a) (b)

Figure 3.9: Results for the bubble's (a) volume and (b) centroid position and ascension velocity for run 1 in the experimental set I.

estimated from the zeroth-order moment and the mean area determined from the ellipse's semi-axes determined from the image second-order central moments. For the same data, Figure 3.10b compares the mean bubble volume obtained using the ellipse's area and the spheroidal shape hypothesis to the injected volume calculated from the pump calibration. Equation 3.18 calculates the mean values using all bubble images for a given run during its ascension. The volume injected by the pump was $40.4 \pm 1.5 \mu$l, obtained by the Eq. 3.43, and the light gray region in Figure 3.10b represents its margin of error.

For all runs of data set I, the mean bubble area obtained from the image zeroth-order moment and the elliptical approximation agree well. The bubble volume estimated from the injected volume for all runs of this data set also agrees well with the values estimated from image analysis, as they are equal within their margin of error. The difference between the mean volume of all runs and the injected volume is lower than 1%. The image processing determines a single bubble's volume more accurately than the predicted injected volume, as shown by the error bars in Figure 3.10b. These results validate the hypothesis of elliptical and spheroidal shapes used to estimate the bubble's volumes from the images.

Figure 3.11 compares the mean ascension velocity, $\overline{U}_{Y'}$, with the vertical component of the instantaneous velocity, $U_{Y'}$, calculated as described in Section 3.3.3 using the time intervals of $\Delta t_1 = 12$ and $\Delta t_2 = 16$ ms for runs 1 to 4 of experimental data set I. These intervals represent moving windows with seven and nine data points, respectively, as $\Delta t_{min} = 2$ ms for this experimental set. As can be seen, the velocity uncertainty decreases as Δt increases. The instantaneous velocity closely aligns with the mean velocity in the bubble's ascension period, decreasing when it approaches the interface. From 98.5 to 99.0 % of the measured data points for each

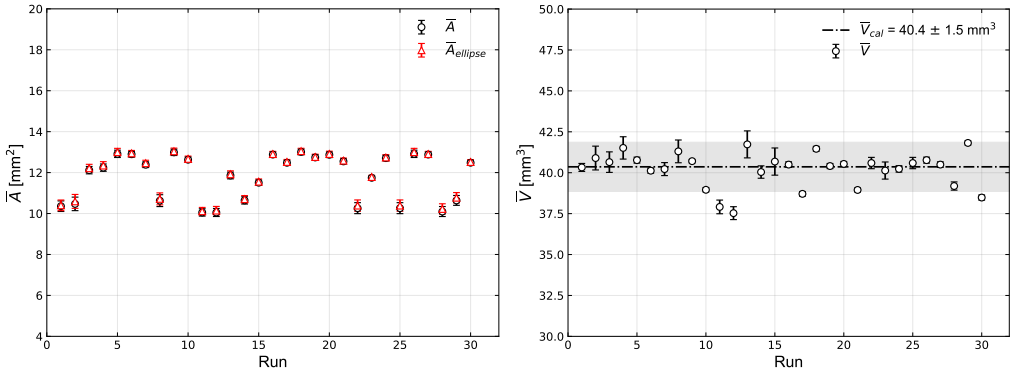

(a) (b)

Figure 3.10: Comparison of (a) bubbles' areas using image processing with and without the elliptical shape assumption and (b) their volumes using image processing and the injected volume determined from the syringe pump calibration for the experimental data set I.

bubble satisfies the condition given by Eq. 3.20. Hence, we opted for the moving window with seven data points ($\Delta t = 12$ ms) to estimate the instantaneous bubbles' velocity. This interval yielded more local and less smooth results, even though with slightly larger errors than those using a moving window with nine data points. An increase in the frame acquisition rate might mitigate these errors. A less smoothed $U_{Y'}$ data is important for detecting its steep drop due to the bubble interaction with the interface.

Figure 3.12 shows $U_{Y'}$ and the bubbles' top surface velocity, $U_{Y'_{top}}$, near the interface position, Y'_{int}, for runs 1 to 4 of the experimental set I. We used the time window with seven data points to calculate both vertical velocities. The shaded region corresponds to the Y'_{int} error of error. As mentioned earlier, the error of $U_{Y'}$ increases as the distance between the bubble and the interface decreases due to the deviation of the data points from the employed linear model. Nevertheless, this approach gave the lowest error coefficients in the adjustment. Both $U_{Y'}$ and $U_{Y'_{top}}$ decrease, reaching zero when the bubble is at the interface.

In addition, Figure 3.12 shows the "collision" instants detected by the PCC and the HCC. The PCC relies on the distance between the bubble top face and the static interface, while the HCC employs the velocity, considering their uncertainties. In all cases, the collision instant predicted by the PCC criterion precedes that of the HCC. Using the HCC, after reaching the interface, $U_{Y'}$ oscillates around zero until coalescence.

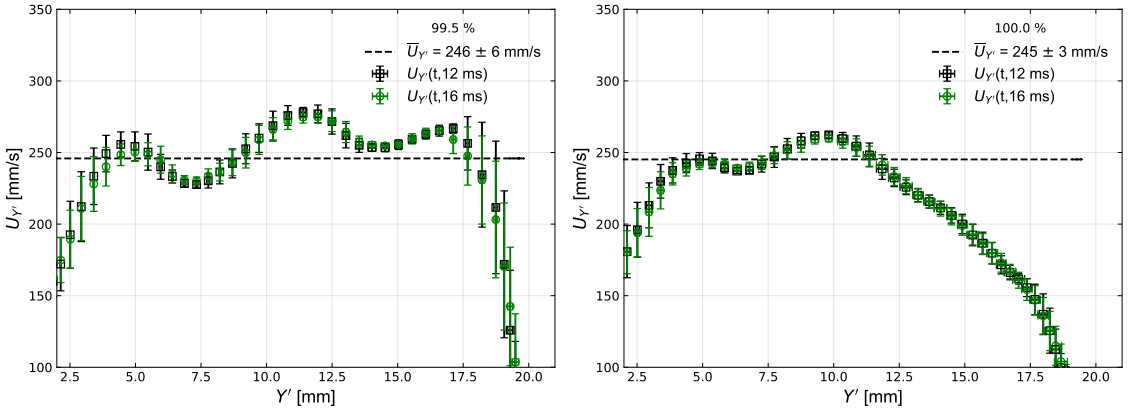

(a) Run 1

(b) Run 2

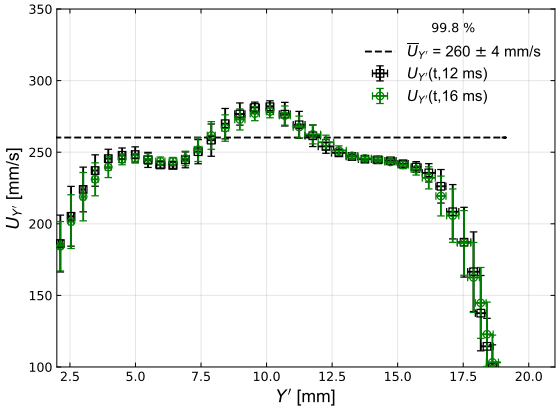

(c) Run 3

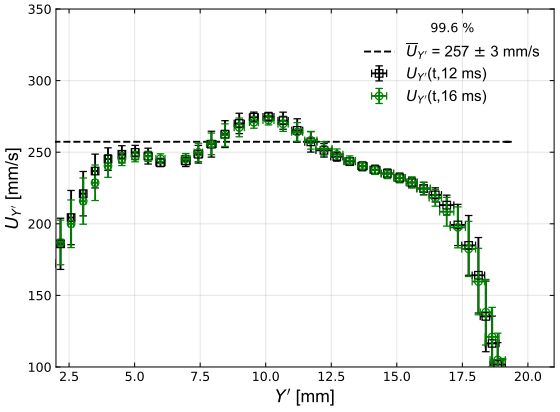

(d) Run 4

Figure 3.11: Behavior of $U_{Y'} \times Y'$ against $\overline{U}_{Y'}$ calculated for the ascension stage. $U_{Y'}$ determined using $\Delta t = 12$ and 16 ms for four runs of the experimental set I, including the percentage of data agreement using these two intervals.

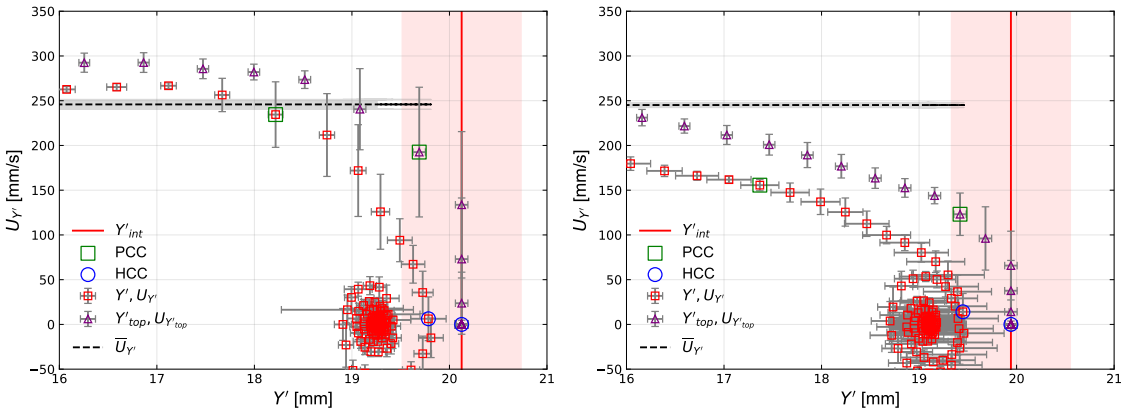

(a) Run 1

(b) Run 2

(c) Run 3

(d) Run 4

Figure 3.12: Behaviors of $U_{Y'}$ and $U_{Y'_{top}}$ calculated using the seven-point moving window near the interface for four runs of experimental set I.

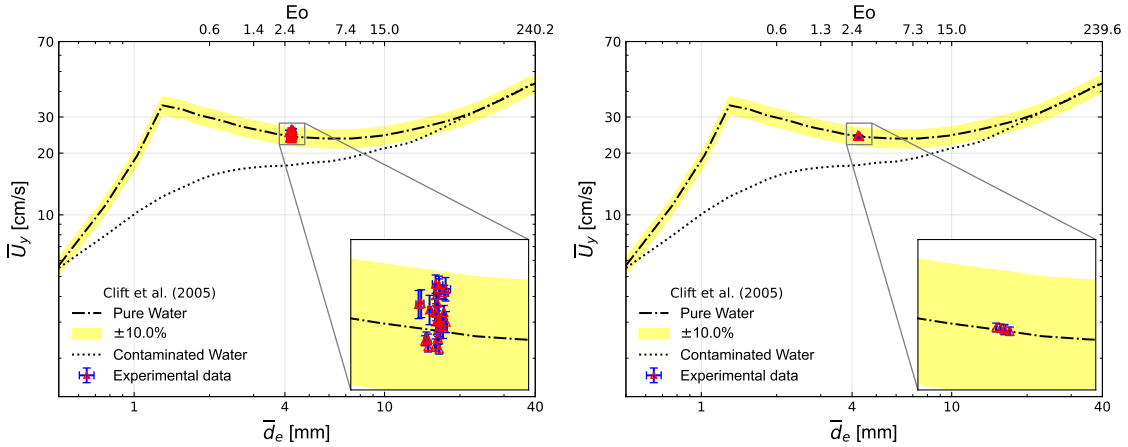

(a) (b)

Figure 3.13: Equivalent diameter and mean ascension velocity for the experimental data sets (a) I and (b) II

.

3.5.3 Effects of the injection flowrate and the image acquisition rate

To increase the accuracy of the bubble's characteristics, we obtained the experimental data set II using a pump actuation frequency five times lower (10 steps/s) and an image acquisition frequency twice higher (1000 fps) than those used in the experimental data set I.

Figure 3.13 compares the equivalent diameter and mean ascension velocity determined from experimental data sets I and II with the results from CLIFT *et al.* [10] for pure and contaminated water. In both experimental data sets, the experimental data for the bubbles' ascension velocity are within the range of ±10 % of the bubble's terminal velocity for pure water. The accuracy and repeatability of the experimental data set I were 0.34 % and 1.20 %, respectively, while the corresponding values for the experimental data set II were 0.83 % and 0.23 %. These results are in excellent agreement with previous knowledge, indicating that we managed to achieve the conditions of bubble ascension in pure water.

Figure 3.14 shows the behavior of the bubbles' centroid, bottom, and top vertical positions over time near the interface for runs 1 and 2 of data set I and runs 31 and 32 for data set II. In experimental data set I, bubbles' bouncing is easily perceived, with amplitudes decreasing after each bounce. Although the terminal velocity and coalescence time results were better determined for the experimental data set II, observing the number of bubble bounces at the interface was difficult because of the small amplitude of bounces.

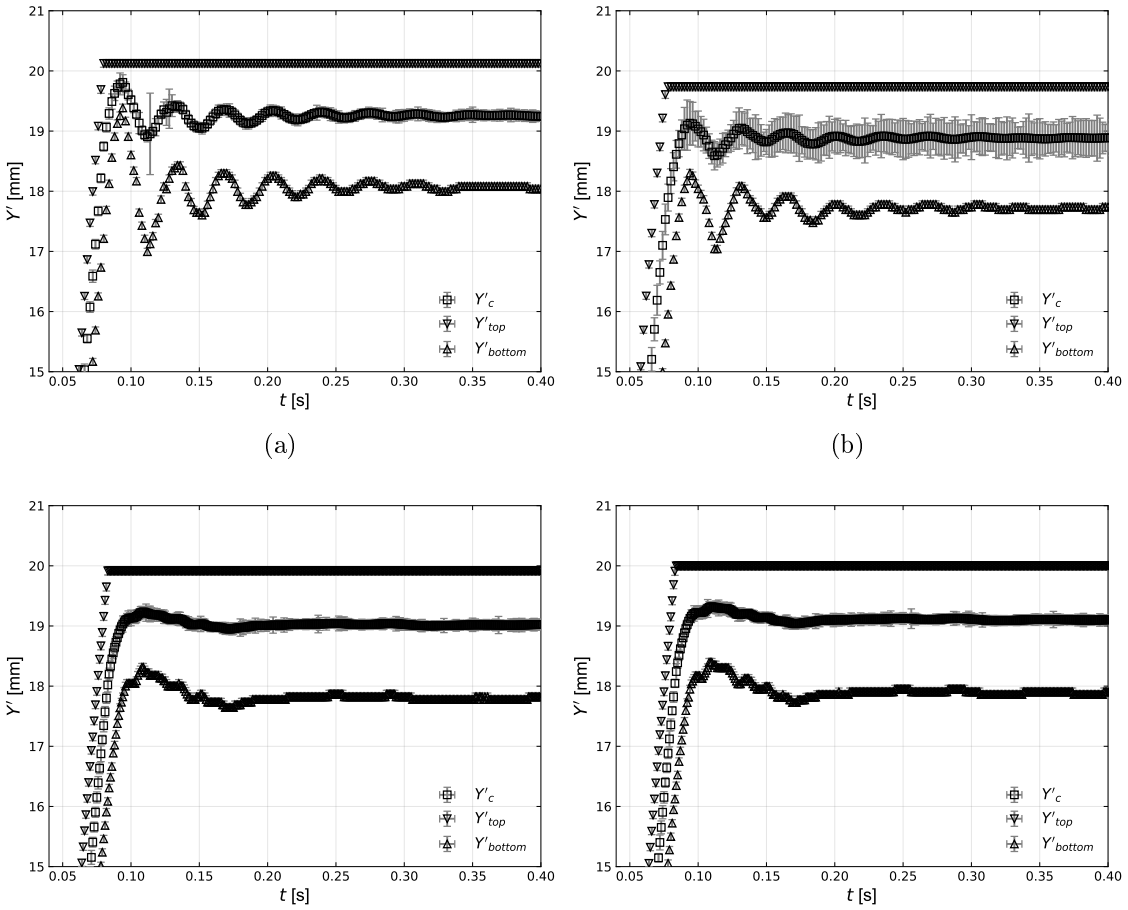

Figure 3.14: Vertical positions of the bubbles' centroid (Y'_c), bottom surface (Y'_{bottom}), and top surface (Y'_{top}) for runs (a) 1 and (b) 2 of data set I, and runs (c) 31 and (d) 32 of data set II.

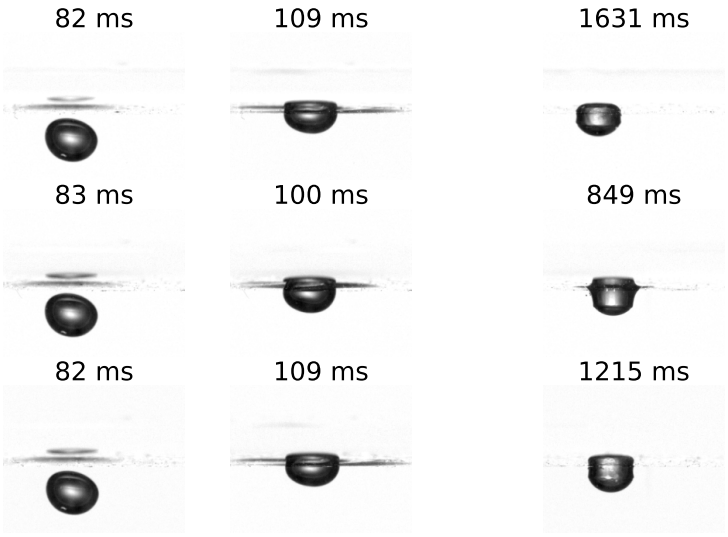

(a) PCC (b) HCC (c) Coalescence

Figure 3.15: Snapshots of bubbles from runs 31, 32, and 33 of data set II at "collision" times with the interface using the (a) PCC and (b) HCC, and (c) at coalescence times.

3.5.4 Coalescence time distribution at terminal velocity

Figure 3.15 displays snapshots of the bubbles' at "collision" times as detected by both collision criteria, and at the coalescence time with the interface for runs 31, 32, and 33 of data set II. Figures 3.15a and 3.15b show, respectively, the "collision" times according to PCC and HCC, and Figure 3.15c shows the coalescence instants. The PCC detected the collision when the bubbles were farther from the interface. In contrast, the HCC detected it when the bubbles visually touched the interface, which is more consistent with forming a thin film between the bubble and the interface before coalescence.

Table 3.5 gives the estimated parameters for the gamma distribution using the coalescence times determined using both "collision" criteria. Both parameters were determined with uncertainties around 10-12 %. Figure 3.16 compares the adjusted cumulative distribution with the experimental cumulative density function using PCC and HCC. For both "collision" criteria, the empirical cumulative distributions and their adjusted gamma distribution exhibit similarity and agreement.

Table 3.6 presents the mean value, $\bar{t}_c$, standard deviation, $s(t_c)$, and their uncertainties at the 95% confidence level for the coalescence time data calculated directly from the experiments and from the gamma distributions adjusted to the coalescence times determined using both "collision" criteria. The values of $\bar{t}_c$ and $s(t_c)$ obtained directly from the experimental data and from the gamma distribution agree well, but the $u_{95}(\bar{t}_c)$ values do not, being about 2.5 times smaller for the estimates using

Table 3.5: Estimated parameters for the gamma distributions for $\bar{t}_c$ for data set I using both collision criteria.

Criterion	Parameters	
	$\alpha \pm u_{95}(\alpha)$	$\beta \pm u_{95}(\beta)$
PCC	3.9 ± 0.4	7.0 ± 0.8
HCC	3.7 ± 0.4	6.8 ± 0.9

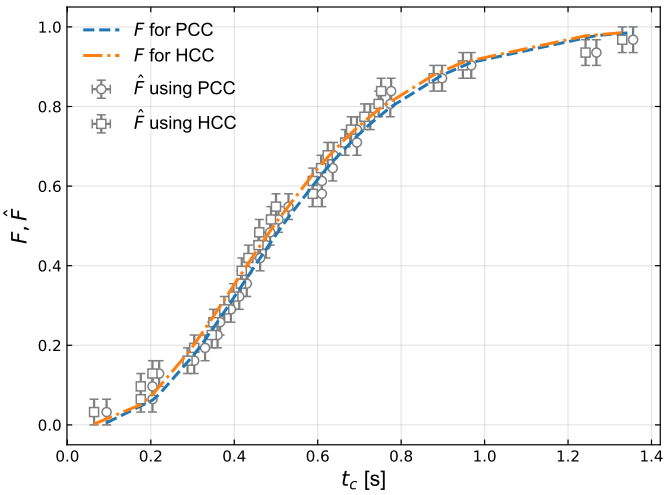

Figure 3.16: Comparison between the "collision" time data obtained using PCC and HCC for data set I to the adjusted cumulative distributions.

the gamma distributions.

3.5.5 Bubbles' bouncing analysis

We carried out the experiments of data set III (Runs 36, 37, 38, 39, and 40), with its larger image resolution, κ=49.9 px/mm, to analyze bubbles' bouncing. Although the data set I experiments did not always allow us to count the number of bounces accurately, we managed to extract seven experiments (Runs 5, 8, 14, 16, 20, 23, and 24) for which we could count the number of bubble bounces. Besides, in data set III, the bubble rising height was smaller, making the bubbles' mean velocity at first "collision" with the interface about 60 % of their terminal velocity (see Supplementary Material 1).

Table 3.6: Coalescence time results for data set I using both collision criteria.

Criterion	Experimental results			Estimates from $F(t_c)$			
	$\bar{t}_c$	$s(t_c)$	$u_{95}(\bar{t}_c)$	$\bar{t}_c$	$u_{95}(\bar{t}_c)$	$s(t_c)$	$u_{95}(s)$
PCC	0.56	0.29	0.11	0.56	0.04	0.28	0.02
HCC	0.54	0.29	0.11	0.54	0.05	0.28	0.02

Table 3.7: Morton and Weber numbers for experimental data sets I and III.

Set	$Mo \times 10^{11}$	$\overline{We}$
I	2.86 ± 0.03	3.62 ± 0.09
III	3.04 ± 0.03	1.26 ± 0.19

Table 3.7 presents the Morton and mean Weber numbers with their uncertainties at the 95% confidence level for data sets I and III. According to HORN *et al.* [14], if the Weber number calculated with the bubble approaching velocity exceeds $We_{crit} \sim 1$, the bubble bounces. All our experiments were above this boundary, indicating bubble bouncing, which indeed occurred. The We values for the experiments in data set III were the nearest to the We_{crit} boundary, showing much lower coalescence times than those observed for the experimental data set I (see Supplementary Material).

Figure 3.17 shows the vertical positions of the centroid, bottom surface, and top surface for the bubbles in runs 36 to 40 of data set III, organizing them according to the number of bounces. We counted the number of bounces at the interface before coalescence, considering the number of times the bubble approached the interface after the first collision. As the amplitude decreases after each "collision", counting the bounces as their number increases becomes difficult. Even for the resolution of data set III, it was difficult to count a large number of bounces.

The reader can notice in Figure 3.17 that the uncertainty in the vertical position of the bubble barycenter largely increases at some instants. Figure 3.14 also shows the same behavior, although to a lesser extent. These larger uncertainties in Y_c' came from the increase in the uncertainties of the zeroth and first-order moments of the bubble image when its upper surface is close to the gas-liquid interface. We determined these larger uncertainties were due to lighting changes associated with bubble and interface deformations that affected the image binarization process. Nevertheless, the Y_c' values at such instants agree with those at neighbor points, which do not present such an increase in their uncertainties. Moreover, we could count the number of bubble bounces even for the runs that presented such behavior.

SANADA *et al.* [12] stated that t_c increases with $N_{bounces}$. Thus, we assumed a linear relationship representing the $t_c(N_{bounces})$ dependency, testing linear models with two parameters and one parameter. For the latter, $t_c(0) = 0$, and it is given by:

$$t_c = \mathcal{T} N_{bounces} \tag{3.44}$$

where $\mathcal{T}$ is the predicted bouncing period in milliseconds.

We fitted the two linear models to the available data for data sets I and III. In these data regressions, the standard uncertainty on the number of bounces was

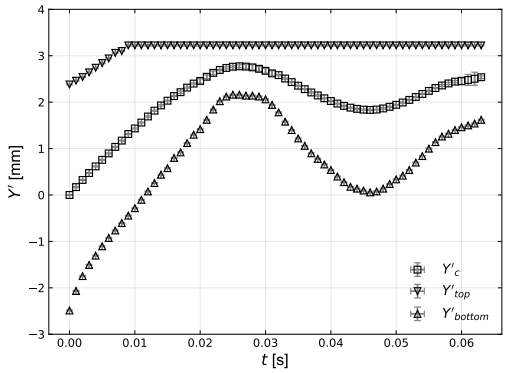

(a) Run 39, $N_{bounces} = 1$

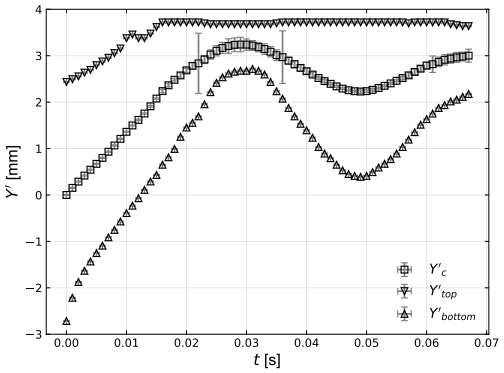

(b) Run 37, $N_{bounces} = 1$

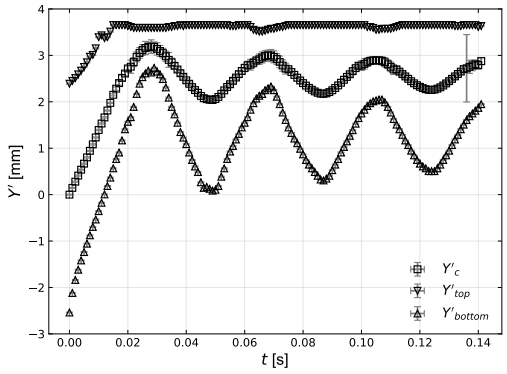

(c) Run 36, $N_{bounces} = 3$

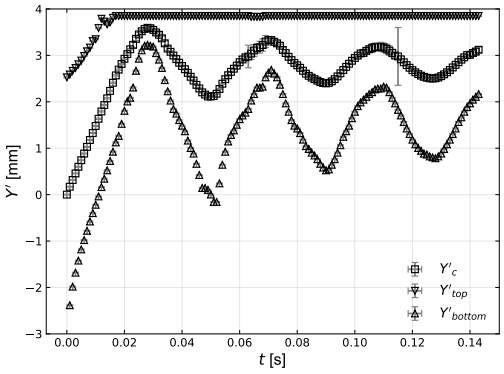

(d) Run 40, $N_{bounces} = 3$

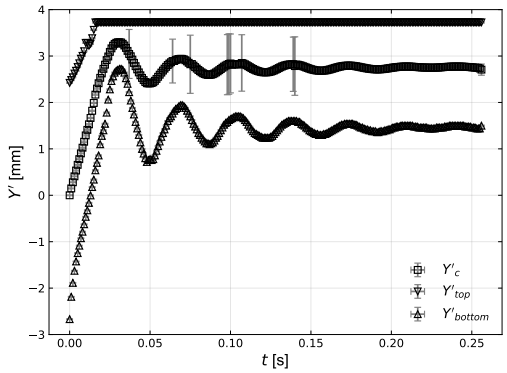

(e) Run 38, $N_{bounces} = 6$

Figure 3.17: Behaviour of the vertical position of the centroid (Y_c'), bottom face (Y_{bottom}'), and top face (Y_{top}') of the bubbles until their coalescence with the interface for data set III.

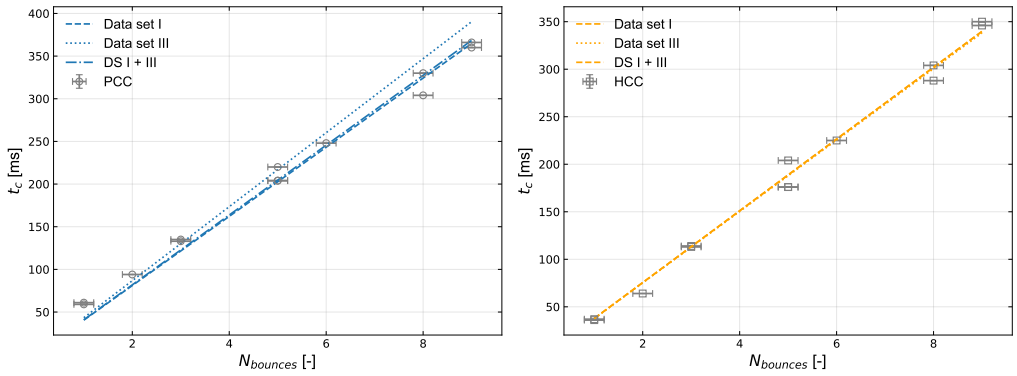

(a) Model PCC (b) Model HCC

Figure 3.18: Fitted linear model between t_c and $N_{bounces}$ for the experimental data sets I, III, and I+III, using (a) PCC and (b) HCC.

Table 3.8: Comparison of resulting $\mathcal{T}$ from experiments.

	$\mathcal{T}$ [ms]		
	DS I	DS III	DS I+III
PCC	40.5 ± 1.4	43.4 ± 5.1	40.9 ± 1.4
HCC	37.8 ±1.5	37.6 ± 0.4	37.7 ± 1.0

evaluated as type B, considering an error of unit and a triangular probability distribution. Only the Eq. 3.44 model correlated the available t_c data using HCC or PCC for both data sets with statistically significant parameter values, which occurs when the 95 % confidence interval does not include zero. Therefore, we presented results only for this model.

Figure 3.18 shows the fitted linear model for $t_c(N_{bounces})$ (Eq. 3.44) using the experimental t_c data determined either using PCC or HCC for data sets I and III, either separately or together. Table 3.8 presents the parameter's values determined for these different data sets using both collision criteria.

Table 3.8 clearly shows that only the HCC led to a fitted model for both data sets with the same parameter value with low uncertainties. Besides, Figure 3.18 shows that the fitted models for each data set or for the two data sets using HCC are identical, which does not occur for the t_c data obtained using PCC. Therefore, the linear model using the t_c data obtained using the HCC is more consistent with the available data.

We could not identify any relationship between the coalescence time of a bouncing bubble and its initial approaching velocity (see Tables 5 and 7 of the Supplementary Material).

3.5.6 Comparison with literature data

This section compares our data with those available in the literature, examining differences and similarities in bubble diameters, coalescence times, and the number of bounces.

The bubbles' diameter of 4 mm presented in this study is smaller than those in the experiments conducted by KIRKPATRICK e LOCKETT [15] for bubbles with a 5 mm diameter, but larger than those reported by SANADA *et al.* [17], SUÑOL e GONZÁLEZ-CINCA [13], ZAWALA e MALYSA [19] and SATO *et al.* [20], who analyzed bubbles with diameters smaller than 2 mm.

Our experiments measured larger coalescence times than those reported in the literature, and our bubbles also bounced more on average.

In our experiments, the coalescence time ranged from 36 to 1550 ms for injection distances of 8.0 to 25.0 mm, with more than nine bounces observed. KIRKPATRICK e LOCKETT [15] reported coalescence times ranging from 150 to 180 ms for rising heights within 8.7 to 27.0 mm, where the bubble either coalesces on the first contact or oscillates twice before coalescence. On the other hand, SANADA *et al.* [12] observed coalescence times from 0 to 60 ms with up to three bounces in low-viscosity liquids, and ZAWALA e MALYSA [19] reported coalescence times within 3 to 5 ms with up to five bounces. SUÑOL e GONZÁLEZ-CINCA [13] measured coalescence times up to 100 ms with up to four bounces, and SATO *et al.* [20] observed a maximum of four bubble bounces.

We could determine the bouncing period to be approximately 37.7 ms for bubbles with the same diameter but different approaching velocities. Only KIRKPATRICK e LOCKETT [15] reported the time interval between the first two "collisions" to be within 40 and 60 ms for similar rising heights. For SANADA *et al.* [17] experiments with low-viscosity liquids, we estimated bouncing periods within 15 to 25 ms.

For small bubbles in the spherical regime, we expected that the coalescence time and the number of bounces would increase with the bubble size, as the bubble approaching velocity also tends to increase for the same rising height. For the ellipsoidal-wobbling bubble regime, this seems not to be true as KIRKPATRICK e LOCKETT [15] data and ours, both in this regime with the same range of rising heights, do not agree in the number of bounces or the coalescence time.

3.6 Conclusions

In this work, we analyzed the coalescence time of ellipsoidal-wobbling air bubbles with a surfactant-free flat air-water interface. The Morton number was 2.9×10^{-11}, and the ranges of Eötvös, Weber, and Reynolds dimensionless numbers were 2 to 3,

1 to 4, and 500 to 1100, respectively. We used high-speed fluid imaging techniques to measure the bubbles' size, velocity, and number of bounces at the interface. Two criteria to establish the time of the first collision with the interface were defined: the physical criterion, PCC, based on the distance between the top of the bubble and the static interface, and the hydrodynamic criterion, HCC, based on bubble velocity. We present results for the bubble volume, velocity, coalescence time, and number of bounces at the interface before coalescence.

The terminal velocity of the bubbles was close to its literature value for pure air-water systems under standard conditions. The distribution of coalescence time for the bubbles colliding at terminal velocity was estimated using both collision criteria. A two-parameter gamma distribution was for representing the coalescence time data for both criteria.

We analyzed the relation between the coalescence time and the number of bubble bounces. We determined that a linear model with just one parameter, the bouncing period, can fit our data for both collision criteria. However, only the coalescence time obtained using the HCC gave the same low-uncertainty value for the bouncing period for two data sets with quite different bubble-approaching velocities, making this criterion more consistent with our data. Using the two data sets and the HCC, the predicted bouncing period was 38 ± 1 milliseconds.

Nomenclature

A	area
a	ellipse's semi-major axis
b	ellipse's semi-minor axis
$\mathbb{D}$	domain of N_b
d_e	equivalent diameter
F	cumulative gamma distribution
$\hat{F}$	empirical cumulative distribution
f_{acq}	frequency of acquisition
f_{pump}	frequency of pump
h_f	bubble-interface distance
I	pixel intensity
I_b	mean intensity inside bubble
I_{max}	maximum intensity
I_{out}	mean intensity outside bubble
I_{thresh}	intensity threshold
i	first index/order
j	second index/order
L	calibration segment length
N	number of total elements in a sample
N_L	number of pixels in the calibration segment

N_b	number of pixels inside bubble
$N_{bubbles}$	number of injected bubbles
$N_{bounces}$	number of bounces
N_{out}	number of pixels outside bubble
N_{frames}	number of frames
N_{steps}	number of steps
N_x	number of pixels in x coordinate
N_y	number of pixels in y coordinate
$\hat{\mathbf{n}}$	unit normal vector
n	number of element in a sample
m_{ij}	image moment of order i and j in the x and y coordinates
$\mathbf{r}_s$	position vector
R_v	mean pump volumetric resolution
S	perimeter
s	standard deviation
T	temperature
t	time
t_c	coalescence time
t_{coll}	collision time
t_{exp}	exposure time
t_f	final time
U	velocity
u	standard uncertainty
V	volume
V_{calc}	volume by pump calibration

V_{inj}	injected volume
X	x position in mm
x	pixel position in x coordinate
x_{bottom}	bubble bottom position in x coordinate
x_{top}	bubble top position in x coordinate
Y	y position in mm
Y_{int}	interface position in mm
y	pixel position in y coordinate
y_{bottom}	bubble bottom position in y coordinate
y_{top}	bubble top position in y coordinate

Greek letters

α	first parameter of the gamma distribution
β	second parameter of the gamma distribution
χ	generic measure
Δ	difference between magnitudes
η	generic power
Γ	gamma distribution
γ	incomplete gamma function
κ	scale factor
λ	eigenvalue
μ_{ij}	image central moment of orders i and j in the x and y coordinates
ν_C	continuous phase dynamic viscosity
ν_D	dispersed phase dynamic viscosity
ρ_C	continuous phase density
ρ_D	dispersed phase density

σ	surface tension
θ	orientation of a with the horizontal
φ	generic variable
ζ	adjustment coefficients

Abbreviations

Eo	Eötvös number
Mo	Morton number
Re	Reynolds number
We	Weber number
ODR	orthogonal regression distance

Appendix

3.A Evaluation of the bubble's characteristics and derived quantities uncertainties

We obtained the uncertainty of bubbles' derived quantities by propagation. For instance, for a generic variable equal to the product of other variables raised to a different power, such as $\varphi = \prod_{n=1}^{N} \chi_n^{\eta_n}$, we have:

$$\frac{u(\varphi)}{\varphi} = \sqrt{\sum_{n=1}^{N} \left(\frac{\eta_n u(\chi_n)}{\chi_n} \right)^2} \tag{3.45}$$

Hence, the propagation of the uncertainties of the image moments of order zero and one determined the standard combined uncertainty of the position coordinates of the bubble centroid (x'_c, y'_c) in pixel units. Similarly, the standard combined uncertainty of the vertical position of the bubble centroid in units of length resulted from the propagation of the uncertainty of the position in pixels and the uncertainty of the calculated scale factor. The scale factor uncertainty arises from combining the uncertainty of the calibration segment length with the uncertainty in the number of pixels in the segment, where their uncertainties stem from the resolution of the calibration target and the number of pixels for an error of unit, respectively, considering a triangular probability distribution.

The semiaxis uncertainties came from the propagation of the uncertainties of the eigenvalues of the central moments. In particular, the uncertainty of the eigenvalues ($\lambda_{1,2}$) are calculated as:

$$u\left(\lambda_{1,2}\right) = \sqrt{\left(\frac{\partial \lambda_1}{\partial \mu_{20}} u(\mu_{20})\right)^2 + \left(\frac{\partial \lambda_1}{\partial \mu_{02}} u(\mu_{02})\right)^2 + \left(\frac{\partial \lambda_1}{\partial \mu_{11}} u(\mu_{11})\right)^2} \tag{3.46}$$

where

$$\frac{\partial \lambda_1}{\partial \mu_{20}} = \frac{1}{2} + \frac{(\mu_{20} - \mu_{02})}{2\Delta\mu} \tag{3.47}$$

$$\frac{\partial \lambda_1}{\partial \mu_{02}} = \frac{1}{2} - \frac{(\mu_{20} - \mu_{02})}{2\Delta\mu} \tag{3.48}$$

$$\frac{\partial \lambda_1}{\partial \mu_{11}} = \frac{2}{\Delta\mu} \mu_{11} \tag{3.49}$$

and

$$\Delta\mu = \sqrt{4\mu_{11}^2 + (\mu_{20} - \mu_{02})^2} \tag{3.50}$$

The uncertainty of the orientation of the ellipse's semi-axes came by propagating the uncertainties of the centered moments, being given as:

$$u(\theta) = \frac{1}{\Delta\mu^2} \sqrt{\mu_{11}^2 u^2(\mu_{20}) + \mu_{11}^2 u^2(\mu_{02}) + (\mu_{20} - \mu_{02})^2 u^2(\mu_{11})} \tag{3.51}$$

The propagation of the uncertainty of the ellipse's semi-axes lengths calculates the uncertainty of the ellipse's area. The bubble's volume uncertainty came from the uncertainty propagation of the semi-axes lengths of an oblate or prolate spheroid, depending on the orientation of its semi-axes. The uncertainty of the equivalent diameter was calculated from the volume uncertainty.

The uncertainty in the instantaneous vertical velocity came from the standard deviation of the parameter of the adjusted linear model obtained via ODR.

The uncertainty of the coalescence time came from propagating the uncertainty of the final time and the collision time. The uncertainty of any time instant is equal to the uncertainty of the camera's exposure time, assuming a triangular distribution. In addition, the uncertainty in any time interval, Δt, is $u(\Delta t) = \sqrt{2u^2(t)}$.

The relative uncertainty of the bubble-interface distance came from propagating the uncertainties of the interface and the top face bubble's position. The uncertainties of the dimensionless numbers are calculated by propagating the uncertainties of the bubbles' characteristics and the fluids' properties.

Finally, all the combined uncertainties were multiplied for a coverage factor to obtain the error range with 95 % confidence level.

Table 3.B.1: Configuration of the experimental data set A. For all runs, f_{pump} = 50 steps/s, $\kappa = 23.0 \pm 0.7$ px/mm, and no time delay.

Run	f_{acq} (fps)	$N^{(*)}_{frames}$	N_{steps}
1 - 5	50	2000	1313
6 - 10	500	2500	212

$^{(*)}$ in single frame mode

3.B Comparison of bubbles' mean volumes from pump calibration and image processing

Two methods estimated the mean bubble volume: method 1, which employs the syringe pump calibration, and method 2, which uses the image processing described in Section 3.3.

3.B.1 Bubble volume from pump calibration (Method 1)

We calculated the mean bubbles' volume from pump calibration as the ratio of the injected volume divided by the number of bubbles generated during injection, $V_{cal} = V_{inj}/N_{bubbles}$, in which $N_{bubbles}$ can be obtained from image observation or signal treatment from image processing. The injected volume is the product of N_{steps} in each run and the pump volumetric resolution obtained previously through calibration, Eq. 3.43.

The uncertainty of the mean volume from pump calibration is obtained by propagating the uncertainties of the injected volume and the number of bubbles, where the uncertainties of N_{steps} and $N_{bubbles}$ were both evaluated as type B considering an error of unit and a triangular distribution.

3.B.2 Configuration of the experimental data set A

We performed two sets of five runs with camera acquisition frequencies of 50 to 500 fps and a pump injection speed of 50 steps/s. Table 3.B.1 shows the configuration of these runs. The operational temperatures during the experiments were 22.58 ± 0.08 and 23.02 ± 0.08 ° C for the runs with 50 and 500 fps acquisition frequencies, respectively.

3.B.3 Bubble volume comparison

Tables 3.B.2 and 3.B.3 present the results of the mean volume of bubbles determined by methods 1 and 2 and their difference for the two sets of experiments of data set

Table 3.B.2: Average volume results for 50 fps and $V_{inj} = 250 \pm 9$ μl.

Run	$N_{bubbles}$	Method 1 $\overline{V}_{cal}$ (μl)	Method 2 $\overline{V}$ (μl)	$\lvert\overline{V}_{cal} - V\rvert$ (μl)
1	7	36 ± 2	39 ± 1	3
2	6	42 ± 2	40 ± 8	2
3	7	36 ± 2	38 ± 15	2
4	6	42 ± 2	42 ± 1	0
5	6	42 ± 2	41 ± 5	1

Table 3.B.3: Average volume results for 500 fps and $V_{inj} = 40.4 \pm 1.5$ μl.

Run	$N_{bubbles}$	Method 1 $\overline{V}_{cal}$ (μl)	Method 2 $\overline{V}$ (μl)	$\lvert\overline{V}_{cal} - V\rvert$ (μl)
6	1		41.3±0.5	0.9
7	1		41.2±1.5	0.8
8	1	40.4±1.5	41.4±1.3	1.0
9	1		37.0±0.4	3.4
10	1		40.8±0.6	0.4

A. The volume injected for the runs with 50 and 500 fps was respectively 250 ± 9 and 40.4 ± 1.5 μl, calculated using Eq. 3.43.

In some experiments running at $f_{acq} = 50$ fps, 1 or 2 satellite bubbles formed during the injection of 6 or 7 bubbles, which increased the error in the mean volume obtained by the image analysis. For the runs at $f_{acq} = 500$ fps, only one bubble formed. In this case, the error in the bubbles' mean volume obtained by method 1 was larger than that obtained from the images by method 2.

Figure 3.B.1 compares the mean bubbles' volume calculated by both methods for the experiments at 50 and 500 fps of data set A. The mean bubbles' volumes obtained by methods 1 and 2 agree within their margins of error. The repeatability of the experiments was much better for the experiments at 500 fps, which generated only one bubble. The mean bubbles' volumes with both methods at both acquisition frequencies also agree within their error margins. These results strongly support the spheroidal bubble hypothesis.

3.B.4 Bubbling regime

Figure 3.B.2 presents the mean bubbles' volume obtained via image processing (method 2) as a function of the syringe pump actuation frequency, which is proportional to the volumetric flowrate through the capillary tube. This figure includes the data from experiments using $f_{acq} = 50$ and 500 fps for $f_{pump} = 50$ steps/s and

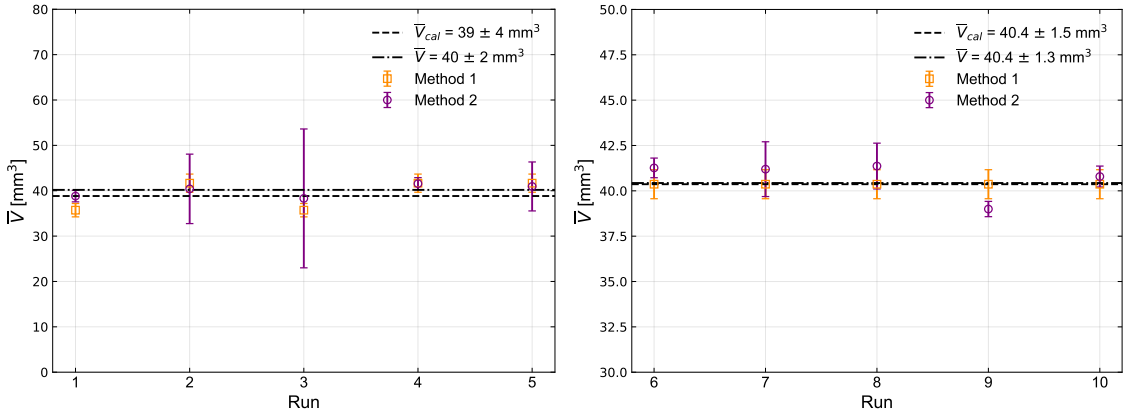

(a) 50 fps (b) 500 fps

Figure 3.B.1: Comparison of bubbles' volume obtained by the two methods for the experimental data set A.

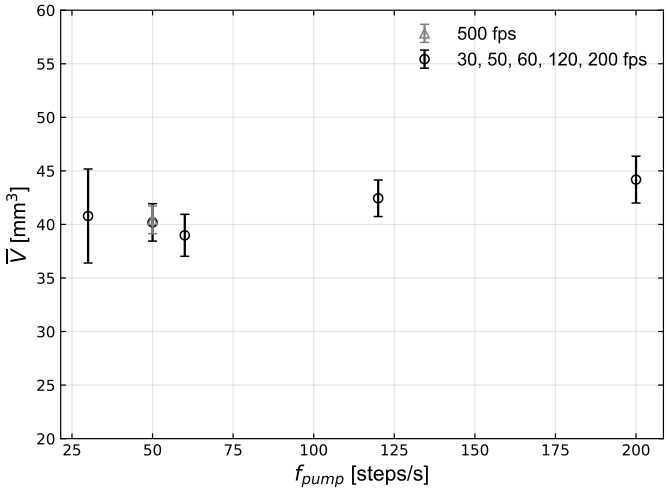

Figure 3.B.2: Bubble volume via image processing (method 2) as a function of the acquisition and pump frequency.

from other experiments, in which $f_{acq} = f_{pump}$ and equal to 30, 60, 120 and 200 fps or steps/s, respectively. These results show that the mean bubbles' volume is independent of the injection flow rate up to 200 steps/s, indicating that bubble formation occurred in the slow-bubbling regime, in which the interfacial force dominates the gas momentum influx.

Chapter 4

A Simplified Model for Bubble Bouncing at Surfactant-Free Gas-Liquid Interfaces and Critical Weber Number for Coalescence

This chapter presents an extended version of the second article, entitled "Modeling Bubble Bouncing at Surfactant-Free Gas-Liquid Interfaces: Critical Weber Number for Coalescence," which was submitted for publication in the journal Chemical Engineering Science.

This study developed a model for bubble bouncing at gas-liquid surfactant-free interfaces and applied it to previously obtained experimental data on the bouncing and coalescence of ellipsoidal-wobbling air bubbles at water-air interfaces. The model derives from the balance of forces acting after the first "collision" between the bubble and the interface, including drag, gravity, buoyancy, virtual mass, and restitution forces. The simplified model is a linear second-order ordinary differential equation for the bubble's barycenter vertical position with three dimensionless parameters, for which, we derived its analytical solution. Using two sets of experimental data as initial conditions, we estimated the three dimensionless physical parameters by fitting the available experimental data using the hydrodynamic "collision" criterion (HCC) for detecting the first "collision". The estimated model parameters for bubbles with the same number of bounces agree well. The approximated model reasonably represented bubbles' motion during bouncing until their coalescence. The predicted oscillation frequency agrees with our previous prediction within their error margins. Both the experimental data and simulated results for the maximum bubble's velocity between bounces indicate that coalescence occurred after this velocity dropped below 5 cm/s, which corresponds to a critical Weber

number below 0.35.

4.1 Introduction

Bubble-interface coalescence occurs in several industrial processes, including froth flotation, oil extraction, and chemical reactors. The coalescence frequency of bubbles is typically quantified using physical models, by the product of two distinct functions: collision frequency and coalescence efficiency [2, 23]. These models are defined according to the mechanisms of each collision. Most of them determine the efficiency as the ratio between the coalescence time and the interaction time. A strategy to study coalescence is to analyze bubbles "collision" to a gas-liquid interface. In this approach, bubbles always have enough time to drain the thin liquid film formed between the interfaces during the collision, allowing the film to reach a critical thickness for rupture, invariably leading to coalescence.

The literature on modeling bubble-interface coalescence focused on the film drainage rate during collisions and the bubbles' bouncing behavior at interfaces. Several researchers have contributed to the development of bubble-interface coalescence models. For instance, DUINEVELD [18] utilized conditions of coalescence and bouncing of two bubbles presented by CHESTERS [33] to model the approaching of spherical bubbles with diameters of 0.7 to 0.9 mm to a free surface, solving an equation of motion until the bubble deforms upon colliding with the surface. This model depends on the initial distance from the bubble's center of mass to the surface, and the bouncing criterion is based on the approach velocity; velocities lower than critical lead to coalescence, while higher velocities increase pressure in the liquid film, causing deformation and repulsion. ZAWALA e MALYSA [19] analyzed 1 mm air bubbles bouncing at air/oil interfaces, modeling film drainage time as being proportional to liquid viscosity and film radius, and inversely proportional to the driving force for thinning. Their experiments showed bubbles approaching the interface at terminal velocity, which slow down, stop, and then bounce. The time to liquid film rupture depended on bubble size, viscosity, and number of rebounds.

SATO *et al.* [20] derived a model to predict the contact time between the interface and bubbles with size between 0.6 and 1.6 mm using two linear springs to account for the restoring force, assuming overall energy conservation. They showed that deformations of both bubble and interface play an important role for bubbles with radii below 0.6 mm. In contrast, surface deformation is more significant for larger bubbles. Furthermore, the contact time slightly increases with the number of bubble bounces. FENG *et al.* [26] examined the dynamics of air bubbles with 1.3 to 1.64 mm of diameter at a compound interface (water-oil-air), finding that oil viscosity significantly influences the pressure in the water film and its drainage.

Their reduced-order model effectively captured the contact time and coefficient of restitution of bubble bouncing. These bubble-bouncing models use the analogy with the mass-spring-damper system, differing mainly in the assumptions of the restitution force. SATO *et al.* [20] use two springs connected in series, considering that the restoring forces due to each deformation should be balanced through the film thickness between the bubble and free surfaces, and FENG *et al.* [26] proposed two effective spring constants to represent a compound water-oil-air interface.

MANICA *et al.* [25] proposed a model including interface and bubble deformations, film drainage, and a force balance for the bubble incorporating buoyancy, drag, added mass effect, and interfacial restitution forces. It takes into account the behavior of the interface at large radial distances by incorporating its deformation through a boundary condition. This model achieved excellent agreement with experimental literature observations for various interfaces in a bubble diameter range of 0.4 to 1.6 mm.

Although current models for bubble-interface coalescence have significantly advanced our understanding of the phenomenon, they face limitations as the definition of the initial film thickness, the prediction of the number of bounces before coalescence, and the estimation of critical values of velocity and Weber number for coalescence, and their applicability to bubbles larger than 2 mm in diameter.

Therefore, in this work, we modeled the bouncing of 4 mm diameter bubbles at an interface without surfactants using an approximate model for the bubble motion after its first "collision" with the interface. The model has three parameters: the bouncing frequency, the amplitude decay factor, and the bubble's added mass coefficient. The experimental data corresponding to the data set III presented by FONTALVO *et al.* [27] was used to estimate the model's parameters, using two different sets of data to determine the model's integration constants. Furthermore, we analyzed the maximum critical approaching velocity after each bounce to determine the critical Weber number for coalescence.

This work structure follows. Section 2 details the deduction of the bubble-bouncing approximate model, the calculation of bubble velocity, and the parameter estimation. Section 3 presents the numerical procedure. Section 4 discusses the results, and Section 5 provides our conclusions.

4.2 Bubble's motion model

We considered vertically oriented forces acting on a bubble in contact with a gas-liquid interface, including drag, gravity, buoyancy, virtual mass, and surface resti-

tution forces. The resulting equation of motion is [52, 53]:

$$(\rho_D + C_V \rho_C)\, V \frac{dU_Y}{dt} = -(\rho_D - \rho_C)\, Vg + F_D + F_R \tag{4.1}$$

where the subscripts D and C refer to the disperse and continuous phases, respectively, ρ is the density, $V = 4/3\pi R^3$ is the bubble's volume, R is the equivalent bubble's radius, g is the gravity acceleration, Y is the upward-oriented vertical coordinate, U_Y is the vertical bubble's velocity, F_D is the drag force, F_R is the restitution force, and C_v is the added mass coefficient.

Similar to the modeling of the normal contact force in the soft-sphere model [52], we used the following linear spring model for the restitution force:

$$F_R = -k(Y_c + R - Y_{int})\sigma, \quad \text{for} \quad Y_c + R > Y_{int} \tag{4.2}$$

where subscripts c and int refer to the bubble's barycenter and gas-liquid interface, k is the restitution coefficient, and σ the surface tension.

We assumed the following drag force model [52]:

$$F_D = -6\pi\nu_C f(Re)\frac{A_c}{R} \tag{4.3}$$

where ν_c is the dynamic viscosity, f is the drag factor, $Re = \rho_C |U_Y| 2R/\nu_C$, is the Reynolds number, and $A_c = \pi a^2$, being a is the horizontal semi-axis of a spheroidal bubble .

Considering that $\sqrt{R/g}$ has time units, we defined the dimensionless variables:

$$\tau = \sqrt{\frac{g}{R}}t, \quad \xi = \frac{Y_c + R - Y_{int}}{R} \quad , \quad K = \frac{\rho_C}{\rho_D} \tag{4.4}$$

resulting in

$$U_Y = \frac{dY_c}{dt} = \sqrt{Rg}\frac{d\xi}{d\tau} \quad , \quad \frac{dU_Y}{dt} = \frac{d^2Y_c}{dt^2} = g\frac{d^2\xi}{d\tau^2} \tag{4.5}$$

where we assumed that Y_{int} is constant. From Eqs. 4.2 and 4.4, the model assumes $\xi \geq 0$ after the first bubble-interface collision.

Substituting Eqs. 4.2 and 4.3 into Eq. 4.1 and using the definitions of the dimensionless variables, Eq. 4.4, we derived:

$$(1 + C_V K)\frac{d^2\xi}{d\tau^2} = (K-1) - \frac{9f(Re)}{2Re_g}K\frac{a^2}{R^2}\frac{d\xi}{d\tau} - k\frac{3}{4\pi}\frac{K}{We_g}\xi \tag{4.6}$$

where we also defined

$$We_g = \frac{\rho_C(gR)R}{\sigma}, \quad \frac{1}{Re_g} = \frac{\nu_C}{\rho_C R\sqrt{Rg}} \tag{4.7}$$

Since $K >> 1$ for a bubble at low pressure, we can write:

$$\frac{d^2\xi}{d\tau^2} + 2B\frac{d\xi}{d\tau} + E\xi = C_V^{-1} \tag{4.8}$$

where

$$B = \frac{9f(Re)}{2C_V Re_g}\frac{a^2}{R^2}, \quad E = k\frac{3}{2\pi}\frac{1}{C_V We_g} \tag{4.9}$$

If we assume that C_V, B, and E are constant in the process, we can derive the analytical solution for Eq. 4.8 (see Appendix 4.A), which reads:

$$\xi(\tau) = \frac{1}{C_V(J^2+B^2)} + e^{-B\tau}\left[C_1\cos(J\tau) + C_2\sin(J\tau)\right] \tag{4.10}$$

where $J^2 = E - B^2 > 0$ is the oscillation frequency, and C_1 and C_2 are the integration constants that can be calculated from experimental data, at $\tau = 0$ or considering other data at $\tau > 0$.

4.2.1 Set 1 of data as initial conditions (IC1)

We estimated the constants C_1 and C_2 using initial conditions at the instant of the first "collision", $\tau = 0$ when bubble velocity $d\xi/d\tau$ is close to zero. In this case, we have:

$$\tau = 0, \quad \xi = \xi(0), \quad \frac{d\xi}{d\tau} = \left.\frac{d\xi}{d\tau}\right|_{\tau=0} \tag{4.11}$$

Using Eq. 4.10, we calculated:

$$C_1 = \xi(0) - \frac{1}{C_V(J^2+B^2)}, \quad C_2 = \frac{B}{J}C_1 + \frac{1}{J}\left.\frac{d\xi}{d\tau}\right|_{\tau=0} \tag{4.12}$$

4.2.2 Set 2 of data as initial conditions (IC2)

Alternatively, we can determine C_1 and C_2 using two experimental values of ξ at different instants:

$$\begin{aligned} \tau &= 0 \quad , \quad \xi = \xi(0) \\ \tau &= \tau_I \quad , \quad \xi = \xi(\tau_I) \end{aligned} \tag{4.13}$$

where τ_I is a second instant, in particular, the second maximum.

From Eq. 4.10, we determined:

$$\begin{aligned} C_1 &= \xi(0) - \frac{1}{C_V(J^2+B^2)} \\ C_2 &= \left[\left(\xi(\tau_I) - \frac{1}{C_V(J^2+B^2)}\right)e^{B\tau_I} - C_1\cos(J\tau_I)\right]\left[\sin(J\tau_I)\right]^{-1} \end{aligned} \tag{4.14}$$

4.2.3 Maximum bubble's velocity between consecutive bounces

We determined the maximum velocity after n bounces from the model represented by Eq. 4.10, from which we can obtain:

$$\begin{aligned} U_Y = \; & \sqrt{gR}\left\{-Be^{-B\tau}\left[C_1\cos(J\tau)+C_2\sin(J\tau)\right]\right. \\ & \left.+e^{-B\tau}\left[-JC_1\sin(J\tau)+JC_2\cos(J\tau)\right]\right\} \end{aligned} \tag{4.15}$$

The maximum bubble's velocity after n bounces comes from:

$$U_{Y_{max}} = \sqrt{gR}\left(\frac{d\xi}{d\tau}\right)_{max_n} \quad , \quad n = 1, ..., N_{bounces} \tag{4.16}$$

which were compared to the corresponding experimental values.

We determined the maximum Weber after n bounces as:

$$We_{max} = 2\left(\frac{\rho U_{Y_{max}}^2 d}{\sigma}\right) = \frac{\rho g d^2}{\sigma}\left(\frac{d\xi}{d\tau}\right)_{max}^2 \tag{4.17}$$

4.2.4 Initial guesses for the parameters

Due to the periodic behavior of the model given by Eq. 4.10, we needed good initial guesses for estimating its parameters, which we obtained from selected experimental data and some assumptions. We used subscript 1 to denote these initial guesses.

The initial guess for C_V was always 0.5, which holds for a sphere accelerating in an infinitely non-viscous fluid. For calculating B_1, we consider the first maximum of ξ at $\tau_1 > 0$, where $J\tau_1 = 2\pi$. Eq. 4.10 gives:

$$\xi(\tau_1) = \frac{1}{C_{V_1}(J_1^2 + B_1^2)} + C_1 e^{-B_1\tau_1} \tag{4.18}$$

where $\xi(\tau_1)$ was the experimental point that best represents this maximum. Moreover, we took $\tau_{1/2}$ from the experimental data as the instant that best approximates the first minimum of ξ. Assuming that ξ is also a maximum at $\tau = 0$, we can estimate:

$$J_1 = \frac{\pi}{\tau_{1/2}} \tag{4.19}$$

Substituting Eq. 4.12, into Eq. 4.18, we have:

$$\xi(\tau_1) = \frac{1}{C_{V_1}(J_1^2 + B_1^2)} + \left(\xi(0) - \frac{1}{C_{V_1}(J_1^2 + B_1^2)}\right) e^{-B_1\tau_1} \tag{4.20}$$

or

$$B_1 = -\frac{1}{\tau_1} \ln \left[\frac{\left(\xi(\tau_1) - \dfrac{1}{C_{V_1}(J_1^2 + B_1^2)} \right)}{\left(\xi(0) - \dfrac{1}{C_{V_1}(J_1^2 + B_1^2)} \right)} \right] \tag{4.21}$$

Eq. 4.21 is nonlinear for B_1, requiring an iterative solution. We use $-\frac{1}{\tau_1} \ln \left(\frac{\xi(\tau_1)}{\xi(\tau_0)} \right)$ as the first guess for B_1.

4.3 Numerical Procedure

We performed all calculations in Python using the SciPy (version 1.9.0) libraries. We used NumPy (version 1.23.1) and Pandas (version 1.4.3) to handle data arrays and data frames. We employed Matplotlib (version 3.5.2) to generate graphics.

We used the experimental data of air bubbles' position, velocity, coalescence time, and number of bounces at the air-water interface in the ellipsoidal-wobbling regime for different bubble approach velocities from a previous work [27]. The experimental points of the first minimum and maximum values of $\xi(\tau)$ as well as their values at the coalescence time, τ_c, were extracted from the experimental data, using Scipy library functions to determine the local maxima and minima from the signal.

We fitted the parameters using the Scipy interface to the orthogonal distance regression (ODR) routine [51], employing the initial guesses described in Section 4.2.4. We solved Eq. 4.21 using the SciPy function `fsolve`.

We assumed that there is an agreement between the approximate model predictions and the experimental data for the bubble's position and instantaneous velocity if the following conditions hold:

$$\Delta Y_c = \frac{|Y_{c,exp} - Y_{c,model}|}{u(Y_{c,exp})} < 1 \tag{4.22}$$

$$\Delta U_Y = \frac{|U_{Y_{exp}} - U_{Y_{model}}|}{u(U_{Y_{exp}})} < 1 \tag{4.23}$$

where $u(Y_{c,exp})$ and $u(U_{Y_{exp}})$ are the experimental uncertainties of the centroid position and its velocity at the 95% confidence level.

For both initial conditions, we evaluated the model accuracy by comparing the arithmetic means and standard deviations of the results of Eqs. 4.22 and 4.23 for all data points of all experiments.

Except for the estimated model parameters, the uncertainties of derived quantities were obtained by the propagation of measurement uncertainties. All the combined uncertainties were multiplied for a coverage factor to obtain the error range at

the 95 % confidence level. The ODR routine provides the standard deviation of the model parameters and we calculate their uncertainties at a 95 % confidence level.

4.4 Results and Discussion

The results below employed the data set III of FONTALVO *et al.* [27]. The hydrodynamic collision criterion (HCC) was chosen to determine the instant of the bubble-interface first contact. Appendix 4.B presents the experimental data points in terms of the dimensionless variables τ and ξ for runs 36 to 40.

4.4.1 Parameters' Estimation and their Analysis

Table 4.4.1 presents the initial guesses for the parameter estimation, applied for estimating the model parameters using both initial conditions.

Table 4.4.1: B_1 and J_1 initial guesses, and $C_{V_1} = 0.5$.

Run	B_1	J_1
36	0.11	2.1
37	0.15	2.3
38	0.17	2.4
39	0.15	2.3
40	0.11	2.1

Tables 4.4.2 and 4.4.3 show the estimated parameters' values from the solution obtained using the two sets of initial conditions. For the IC1 model, the arithmetic mean values of B, C_V, and J with their propagated uncertainties at the 95% confidence level are 0.18 ± 0.08, 0.33 ± 0.03, and 2.41 ± 0.07, respectively. The relative standard deviations are 51.6 %, 9.9 %, and 3.5 %. For the IC2 model, the mean values of B, C_V, and J, with their uncertainties, are 0.24 ± 0.11, 0.32 ± 0.03, and 2.47 ± 0.06, with relative standard deviations of 45.4 %, 9.6 %, and 2.8%, respectively. Although the relative standard deviations of J and C_V for the model with IC1 and IC2 are smaller than 10%, the relative deviation for B is much larger, which may be attributed to its dependence on the drag coefficient of highly deformed bubbles. The estimated B and J values for the IC2 model agree within their error margin for the bubbles with the same number of bounces, which did not occur for the IC1 model results.

The number of bounces can be calculated as:

$$N_{bounces}^{calc} = \frac{J\tau_c}{2\pi} \tag{4.24}$$

Table 4.4.2: Parameters estimation for initial condition 1.

Run	B	C_V	J	$N_{bounces}$
36	0.10 ± 0.01	0.357 ± 0.003	2.38 ± 0.01	3
37	0.12 ± 0.04	0.353 ± 0.004	2.34 ± 0.01	1
38	0.33 ± 0.02	0.290 ± 0.003	2.51 ± 0.01	6
39	0.22 ± 0.03	0.296 ± 0.003	2.50 ± 0.01	1
40	0.14 ± 0.02	0.345 ± 0.005	2.34 ± 0.01	3

Table 4.4.3: Parameters estimation for initial condition 2.

Run	B	C_V	J	$N_{bounces}$
36	0.14 ± 0.01	0.358 ± 0.004	2.41 ± 0.01	3
37	0.24 ± 0.01	0.320 ± 0.009	2.49 ± 0.04	1
38	0.42 ± 0.02	0.279 ± 0.006	2.56 ± 0.03	6
39	0.26 ± 0.01	0.299 ± 0.008	2.49 ± 0.04	1
40	0.16 ± 0.01	0.333 ± 0.004	2.39 ± 0.01	3

where τ_c is the experimental dimensionless coalescence time. The number of bounces obtained by Eq. 4.24 for runs 36 to 40 are approximately 3, 1, 6, 1, and 3, respectively. These values agree with the experimental number of bubble bounces in each run.

FONTALVO *et al.* [27] determined the period of bouncing using the HCC as $\mathcal{T} = 38 \pm 1$ ms. For each run i, the values of J can be calculated from Eq. 4.4 and $\mathcal{T}$ by

$$J^{calc} = \frac{2\pi}{\mathcal{T}}\sqrt{\frac{R_i}{g}} \tag{4.25}$$

which gives 2.42, 2.42, 2.42, 2,43, and 2,45 for runs 36 to 40, respectively, all with an uncertainty of 0.06 at a 95% confidence level. Using IC2, the model predicted all bouncing frequencies, except for run 38, in agreement with the estimated values of J within their margins of error. Run 38 showed a slightly higher estimated J value. In contrast, the J values estimated for the IC1 model agree with those calculated from Eq. 4.25 for only two runs.

4.4.2 Predicting bubble's vertical position and velocity

Table 4.4.4 presents the percentage of Y_c and U_Y data points that agree using the criteria given by Eqs. 4.22 and 4.23 using IC1 and IC2 for calculating the model constants. The arithmetic means of ΔY_c for the IC1 and IC2 models are 81.7 % and 80.8 %, while the corresponding values for ΔU_Y are 54.5% and 52.4%. The best predictions are for cases 37 and 39 with the lowest bounce number. The standard deviations using the IC1 model were 22.7 % and 19.9 % for ΔY_c and ΔU_Y, respec-

tively, while the corresponding values for the IC2 model are 22.5 % and 17.9 %. These results are quite similar.

Table 4.4.4: Percentage of data points satisfying Eqs. 4.22 and 4.23 using IC1 and IC2 for data set III.

	$\Delta Y_{c,IC1}$	$\Delta Y_{c,IC2}$	$\Delta U_{Y,IC1}$	$\Delta U_{Y,IC2}$
Run	%	%	%	%
36	93.9	88.6	51.8	57
37	100	100	71.1	65.8
38	70.4	66.8	28.8	27
39	97.3	100	75.7	70.3
40	47	48.7	45.2	41.7

Figures 4.4.1 and 4.4.2 depict a comparison between the model prediction of Y_c and U_y against experimental data using IC2. As shown, the approximated model reasonably represents the bubble's motion during bouncing until their coalescence with the interface.

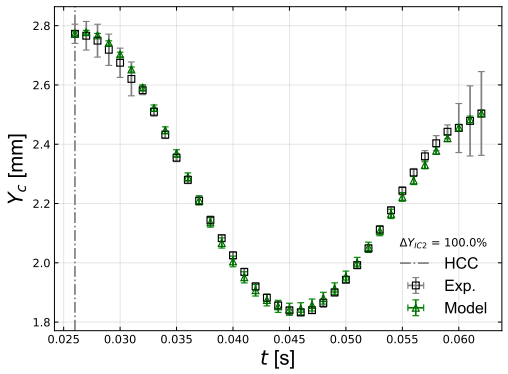

(a) Run 39

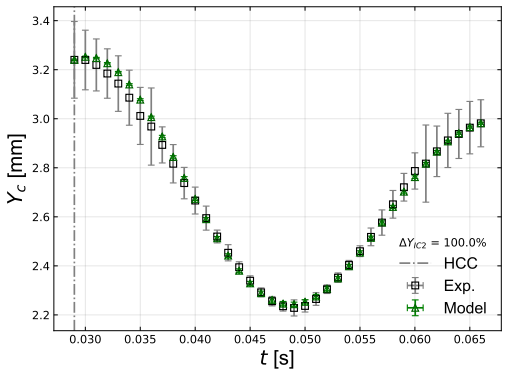

(b) Run 37

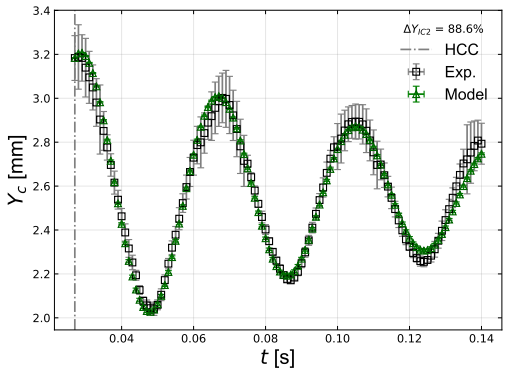

(c) Run 36

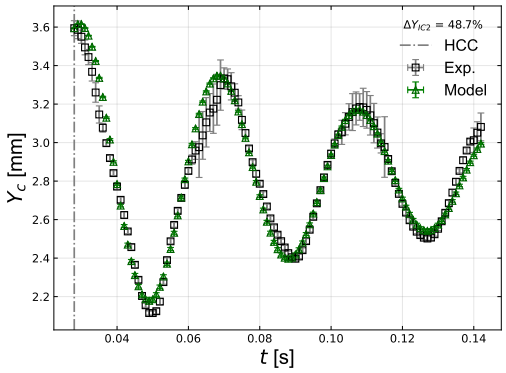

(d) Run 40

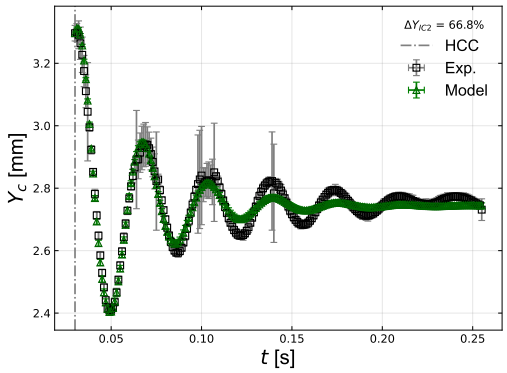

(e) Run 38

Figure 4.4.1: Behaviour of Y_c against t until bubble coalescence with the interface for experimental data set III using IC2.

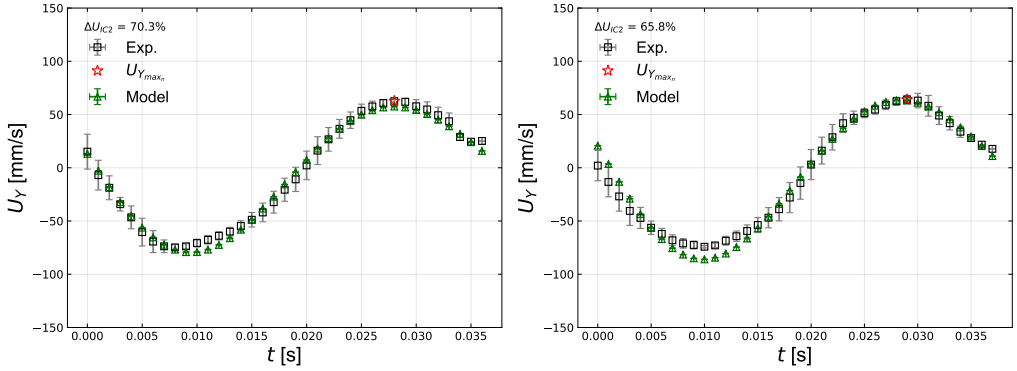

(a) Run 39

(b) Run 37

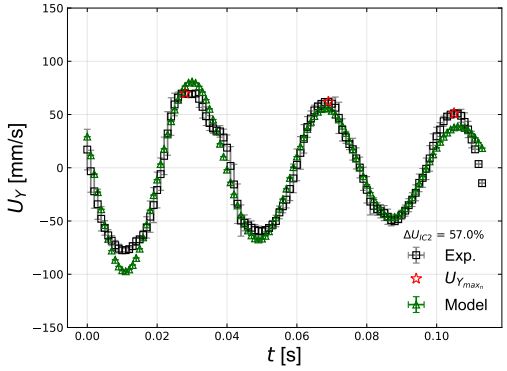

(c) Run 36

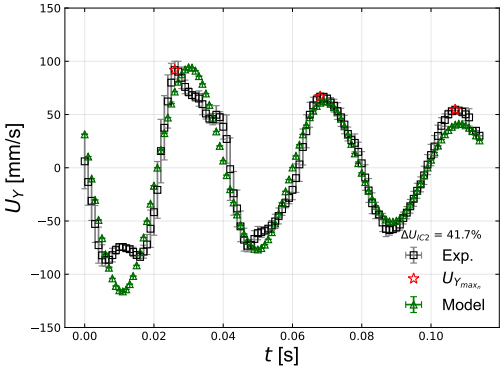

(d) Run 40

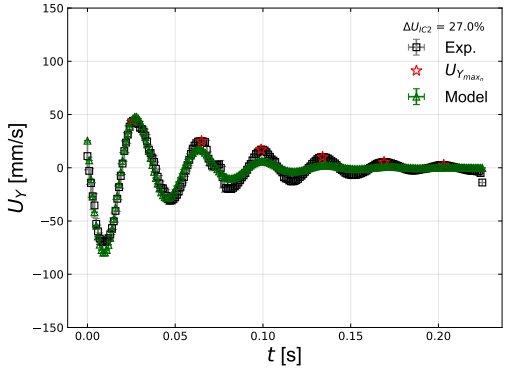

(e) Run 38

Figure 4.4.2: Behaviour of U_y against t until bubble coalescence with the interface for experimental data set III using IC2.

4.4.3 Critical velocity and Weber number for coalescence after bouncing.

We compared the maximum velocity after each bounce predicted by the model using IC1 and IC2 with those determined from the experimental data. Table 4.4.5 presents these results for runs 36 to 40 of data set III, which shows that the predicted $U_{Y_{max}}$ using IC1 are slightly better than those obtained using IC2. Except for run 38, the

maximum bubbles' velocities between bounces determined using the experimental and simulated data indicate that coalescence occurs when the velocity drops below 5 cm/s, which agrees with the critical velocity value estimated by KIRKPATRICK e LOCKETT [15], and corresponds to a critical Weber number for coalescence below 0.35.

Table 4.4.5: Comparison of $U_{Y_{max}}$ (mm/s) and We_{max} between experiments and model.

		Exp.		IC1		IC2	
Run	Bounce	U_Y	We	U_Y	We	U_Y	We
37	1	64.1 ± 3.7	0.53 ± 0.06	67.1	0.58	63.4	0.52
39	1	62.6 ± 1.8	0.51 ± 0.03	61.0	0.48	57.5	0.43
36	1	69.9 ± 2.2	0.63 ± 0.04	81.1	0.84	80.9	0.84
	2	61.8 ± 1.4	0.49 ± 0.02	62.8	0.51	56.1	0.40
	3	51.1 ± 0.7	0.34 ± 0.01	48.9	0.31	38.8	0.19
40	1	91.7 ± 8.3	1.11 ± 0.20	91.3	1.10	94.3	1.17
	2	66.8 ± 1.5	0.59 ± 0.03	62.6	0.52	62.4	0.51
	3	54.6 ± 1.1	0.39 ± 0.02	43.0	0.24	41.3	0.22
38	1	44.1 ± 0.9	0.25 ± 0.01	51.8	0.34	47.7	0.29
	2	25.0 ± 0.8	0.080 ± 0.005	22.9	0.067	17.1	0.04
	3	17.1 ± 0.6	0.038 ± 0.003	10.1	0.013	6.1	0.005
	4	10.1 ± 0.3	0.013 ± 0.001	4.4	0.003	2.2	0.001
	5	5.3 ± 0.2	0.0037 ± 0.0002	2.0	0.0005	0.8	0.0001
	6	2.7 ± 0.2	0.0009 ± 0.0001	0.9	0.0001	0.3	0.00001

4.5 Conclusions

We modeled the bouncing motion of ellipsoidal-wobbling air bubbles at water-air interfaces without surfactants until coalescence using a simplified model based on the balance of forces acting after the first bubble-interface collision. The model represented well the bubbles' motion at the interface after their first "collision".

We compared the model results using two sets of data (IC1 and IC2) to determine its integration constants. The centroid position and its velocity predicted by the model with both sets of initial conditions and fitted parameters agree with

experiments for over 65% of the data points. The bouncing frequency predicted by the model agrees with the previous experimental prediction of the bouncing period. For the analyzed experimental runs, the added mass coefficient was determined with a standard deviation lower than 3 %. The IC2 model estimated values for the amplitude decay factor and bouncing frequency that agree within their error margins for bubbles with the same number of bounces.

The maximum bubble's velocity values between bounces determined using the experimental data and simulated results show that coalescence occurs after the velocity drops below 5 cm/s, indicating a critical Weber number for coalescence somewhat below 0.35.

Nomenclature

A_c	projected area
B, E, J	model parameters
C_1, C_2	model constants
C_D	drag coefficient
C_V	added mass coefficient
a	ellipse's semi-major axis
F_D	drag force
F_R	restitution force
g	gravity
J	dimensionless frequency of an oscillation
k	stiffness
K	ratio between of the continuous and dispersed phases viscosity
R	equivalent radius
T	temperature
t	time
$U_{Y_{max}}$	maximum instantaneous vertical velocity
U_Y	instantaneous vertical velocity
u	standard uncertainty
V	volume
Y_c	vertical position of bubble's barycenter in mm

Y_{int} vertical interface position in mm

Greek letters

ν_C continuous phase dynamic viscosity

ρ_C continuous phase density

ρ_D dispersed phase density

σ surface tension

τ dimensionless time

τ_c dimensionless coalescence time

ξ dimensionless vertical bubble position

Abbreviations

Re Reynolds number

We Weber number

We_{max} maximum Weber number after n bounces

ODR orthogonal distance regression

Appendix

4.A Deduction of bubble bouncing approximate model

The solution of Eq. 4.8 is the sum of the solution of the homogeneous equation and a particular solution.

$$\xi(\tau) = \xi_h(\tau) + \xi_p(\tau) \tag{4.26}$$

The characteristic polynomial of the ordinary differential equation is:

$$\Xi^2 + 2B\Xi + E = 0 \tag{4.27}$$

whose roots are:

$$\Xi = -B \pm i\sqrt{E - B^2} \tag{4.28}$$

for $J^2 = E - B^2 > 0$.

Table 4.B.1: Selected experimental points of data set III in terms of dimensionless variables.

Exp.	36	37	38	39	40
$\tau_{1/2}$	1.50 ± 0.01	1.37 ± 0.01	1.30 ± 0.01	1.36 ± 0.01	1.48 ± 0.01
τ_1	2.80 ± 0.01	2.53 ± 0.01	2.66 ± 0.01	2.45 ± 0.01	2.83 ± 0.01
τ_c	7.73 ± 0.01	2.53 ± 0.01	15.37 ± 0.02	2.45 ± 0.01	7.69 ± 0.01
$\xi(0)$	0.78 ± 0.05	0.77 ± 0.07	0.80 ± 0.01	0.79 ± 0.02	0.88 ± 0.02
$\xi(\tau_{1/2})$	0.23 ± 0.01	0.29 ± 0.02	0.37 ± 0.01	0.34 ± 0.01	0.19 ± 0.01
$\xi(\tau_1)$	0.69 ± 0.05	0.65 ± 0.05	0.63 ± 0.03	0.66 ± 0.07	0.76 ± 0.03
$\xi(\tau_c)$	0.59 ± 0.04	0.65 ± 0.05	0.53 ± 0.02	0.66 ± 0.07	0.64 ± 0.03

Thus, the solution of the homogeneous equation is:

$$\xi_h(\tau) = e^{-B\tau}\left[C_1\cos(J\tau) + C_2\sin(J\tau)\right] \tag{4.29}$$

It is easy to show that the particular solution for this case is:

$$\xi_p = \frac{1}{C_V E} = \frac{1}{C_V(J^2 + B^2)} \tag{4.30}$$

4.B Experimental Data

Tables 4.B.1 presents some selected data points from experimental data set III. These points are used in the numerical procedure to estimate the model constants and the initial guesses of the model parameters. They are presented in terms of dimensionless variables defined in Eq. 4.4.

Chapter 5

Conclusions and Suggestions

5.1 Conclusions

In this thesis, we analyzed the coalescence time of ellipsoidal-wobbling air bubbles colliding on a surfactant-free flat air-water interface encompassing the Morton, Eötvös, Weber, and Reynolds dimensionless numbers of 2.9×10^{-11}, 2 - 3, 1 - 4, and 500 - 1100, respectively. We used high-speed fluid imaging techniques to measure the bubble's size, velocity, and bounce with the interface.

We present results for the bubble volume, velocity, coalescence time, and number of bounces at the interface before coalescence. The mean volume and the equivalent diameter of bubbles were determined with excellent accuracy, giving the hypothesis of an ellipsoid of revolution from the image processing. The terminal velocity of the bubbles was close to its literature value for pure air-water systems under standard conditions, being within ± 10 % of this value. Two criteria to establish the time of the collision were defined: the physical criterion, based on the distance between the top of the bubble and the static interface, and the hydrodynamic criterion, based on bubble deceleration. The distribution of coalescence time for the bubbles colliding at terminal velocity was estimated by both collision criteria. A two-parameter gamma distribution proved to be adequate for representing the coalescence time data for both criteria.

The coalescence time was well-fitted by linear models as a function of the number of bounces for both collision criteria. We determined a period of an oscillation between each bounce using the hydrodynamic collision criterion. The better adjustment to a linear model with a zero linear coefficient makes this criterion more consistent than the physical one.

Additionally, we modeled the motion of air bubbles bouncing up to coalescence at water/air interfaces using an approximate model based on the balance of forces acting on the bubble after the collision. The model represents fairly well the motion

of bouncing bubbles until coalescence. Additionally, we made a comparative analysis of the estimated parameters using two set of data to determine the integration constants of the approximated model. We obtained that the velocity predicted by the fitted model using both conditions agrees to the experimental data for more than 60% of the data within their margins of error, including the maximum velocity after n bounces. The bouncing frequency predicted by the model agrees with the previous prediction in their margins of error. The critical bubble's velocity between bounces occurred after this velocity drops below 5 cm/s, when the Weber number was below 0.35.

These results are a basis for planning new experiments, analyzing the coalescence of bubbles in stagnant fluids with different properties and/or turbulent flows.

5.2 Suggestions

An analysis of the current experimental data should focus on contact time i.e. the duration a bubble remains in contact with the free interface or interaction time.

In addition, enhancements to the experimental setup can be made by using a syringe pump for bubble injection with continuous operation and remote control via Wi-Fi [54]. Additionally, a remote data acquisition with assisted processing using deep learning methods, such as convolutional neural networks, should aim to detect and process data in real-time, reducing the required hard drive space and increasing overall data efficiency.

Improvements in image processing are needed to address errors caused by lighting changes associated with bubble and interface deformations, which affect the image binarization process. These improvements should include the development of new filters and image processing operations.

The experimental operating range should also be expanded by using different fluids, such as water-glycerin mixtures or silicon oils, to analyze the effect of changing fluid properties on oscillation frequency and the number of bounces before coalescence, which directly influences coalescence time.

Further investigation into the use of additives that promote coalescence could help reduce coalescence times and increase efficiency, particularly, in turbulent flows where coalescence does not occur.

References

[1] GUINANCIO, R. *Análise experimental de modelos de eficiência de coalescência de bolhas.* Dissertação de mestrado, Universidade Federal do Rio de Janeiro, 2015.

[2] MITRE, J., TAKAHASHI, R., RIBEIRO JR, C., et al. "Analysis of breakage and coalescence models for bubble columns", *Chemical Engineering Science*, v. 65, n. 23, pp. 6089–6100, 2010.

[3] ZHANG, X.-B., LUO, Z.-H. "Effects of Bubble Coalescence and Breakup Models on the Simulation of Bubble Columns", *Chemical Engineering Science*, p. 115850, 2020.

[4] MOHAYEJI, M., FARSI, M., RAHIMPOUR, M., et al. "Modeling and operability analysis of water separation from crude oil in an industrial gravitational coalescer", *Journal of the Taiwan Institute of Chemical Engineers*, v. 60, pp. 76–82, 2016.

[5] FUERSTENAU, M. C., JAMESON, G. J., YOON, R.-H. *Froth flotation: a century of innovation.* SME, 2007.

[6] WANG, H., YANG, W., YAN, X., et al. "Regulation of bubble size in flotation: A review", *Journal of Environmental Chemical Engineering*, p. 104070, 2020.

[7] MITRE, J. F., LAGE, P. L., SOUZA, M. A., et al. "Droplet breakage and coalescence models for the flow of water-in-oil emulsions through a valve-like element", *Chemical Engineering Research and Design*, v. 92, n. 11, pp. 2493–2508, 2014.

[8] KHAJEHESAMEDINI, A., MIRANDA, D. M., TAVARES, F., et al. "Development of Coalescence and Capture Kernels for the Electrocoalescence Process Based on Batch Experiments", *Industrial & Engineering Chemistry Research*, v. 59, n. 3, pp. 1277–1297, 2019.

[9] COELHO, D. B. *Projeto e construção de uma célula de coalescência de bolhas.* Dissertação de mestrado, Universidade Federal do Rio de Janeiro, 2014.

[10] CLIFT, R., GRACE, J. R., WEBER, M. E. *Bubbles, drops, and particles.* Courier Corporation, 2005.

[11] TRIPATHI, M. K., SAHU, K. C., GOVINDARAJAN, R. "Dynamics of an initially spherical bubble rising in quiescent liquid", *Nature communications*, v. 6, n. 1, pp. 1–9, 2015.

[12] SANADA, T., SATO, A., SHIROTA, M., et al. "Motion and coalescence of a pair of bubbles rising side by side", *Chemical Engineering Science*, v. 64, n. 11, pp. 2659–2671, 2009.

[13] SUÑOL, F., GONZÁLEZ-CINCA, R. "Rise, bouncing and coalescence of bubbles impacting at a free surface", *Colloids and Surfaces A: Physicochemical and Engineering Aspects*, v. 365, n. 1-3, pp. 36–42, 2010.

[14] HORN, R. G., DEL CASTILLO, L. A., OHNISHI, S. "Coalescence map for bubbles in surfactant-free aqueous electrolyte solutions", *Advances in colloid and interface science*, v. 168, n. 1-2, pp. 85–92, 2011.

[15] KIRKPATRICK, R., LOCKETT, M. "The influence of approach velocity on bubble coalescence", *Chemical Engineering Science*, v. 29, n. 12, pp. 2363–2373, 1974.

[16] DOUBLIEZ, L. "The drainage and rupture of a non-foaming liquid film formed upon bubble impact with a free surface", *International journal of multiphase flow*, v. 17, n. 6, pp. 783–803, 1991.

[17] SANADA, T., WATANABE, M., FUKANO, T. "Effects of viscosity on coalescence of a bubble upon impact with a free surface", *Chemical engineering science*, v. 60, n. 19, pp. 5372–5384, 2005.

[18] DUINEVELD, P. C. *Bouncing and coalescence of two bubbles in water.* Ph.d. thesis, Twente University, Netherlands, 1994.

[19] ZAWALA, J., MALYSA, K. "Influence of the impact velocity and size of the film formed on bubble coalescence time at water surface", *Langmuir*, v. 27, n. 6, pp. 2250–2257, 2011.

[20] SATO, A., SHIROTA, M., SANADA, T., et al. "Modeling of bouncing of a single clean bubble on a free surface", *Physics of Fluids*, v. 23, n. 1, 2011.

[21] LEHR, F., MILLIES, M., MEWES, D. "Bubble-Size distributions and flow fields in bubble columns", *AIChE Journal*, v. 48, n. 11, pp. 2426–2443, 2002.

[22] CHESTERS, A., HOFMAN, G. "Bubble coalescence in pure liquids". In: *Mechanics and Physics of Bubbles in Liquids*, Springer, pp. 353–361, The Netherlands, 1982.

[23] LIAO, Y., LUCAS, D. "A literature review on mechanisms and models for the coalescence process of fluid particles", *Chemical Engineering Science*, v. 65, n. 10, pp. 2851–2864, 2010.

[24] ZAWALA, J., DORBOLO, S., TERWAGNE, D., et al. "Bouncing bubble on a liquid/gas interface resting or vibrating", *Soft Matter*, v. 7, n. 14, pp. 6719–6726, 2011.

[25] MANICA, R., KLASEBOER, E., CHAN, D. Y. "The impact and bounce of air bubbles at a flat fluid interface", *Soft Matter*, v. 12, n. 13, pp. 3271–3282, 2016.

[26] FENG, J., MURADOGLU, M., KIM, H., et al. "Dynamics of a bubble bouncing at a liquid/liquid/gas interface", *Journal of Fluid Mechanics*, v. 807, pp. 324, 2016.

[27] FONTALVO, E. M., LAGE, P. L., LOUREIRO, J. B. "Coalescence Time of Ellipsoidal-Wobbling Bubbles at Surfactant-Free Interface: Experimental Analysis and Collision Criteria", *Chemical Engineering Science*, p. 120756, 2024.

[28] NEETHLING, S., CILLIERS, J. "Simulation of the effect of froth washing on flotation performance", *Chemical engineering science*, v. 56, n. 21-22, pp. 6303–6311, 2001.

[29] RUBIO, J., SOUZA, M., SMITH, R. "Overview of flotation as a wastewater treatment technique", *Minerals engineering*, v. 15, n. 3, pp. 139–155, 2002.

[30] RIBEIRO JR, C. P., MEWES, D. "The effect of electrolytes on the critical velocity for bubble coalescence", *Chemical Engineering Journal*, v. 126, n. 1, pp. 23–33, 2007.

[31] MARRUCCI, G. "A theory of coalescence", *Chemical engineering science*, v. 24, n. 6, pp. 975–985, 1969. doi: https://doi.org/10.1016/0009-2509(69)87006-5.

[32] JONES, A., WILSON, S. "The film drainage problem in droplet coalescence", *Journal of Fluid Mechanics*, v. 87, n. 2, pp. 263–288, 1978.

[33] CHESTERS, A. "Modelling of coalescence processes in fluid-liquid dispersions: a review of current understanding", *Chemical engineering research and design*, v. 69, n. A4, pp. 259–270, 1991.

[34] CRAIG, V., NINHAM, B., PASHLEY, R. "Effect of electrolytes on bubble coalescence", *Nature*, v. 364, n. 6435, pp. 317–319, 1993.

[35] LIU, B., MANICA, R., LIU, Q., et al. "Coalescence or Bounce? How Surfactant Adsorption in Milliseconds Affects Bubble Collision", *The journal of physical chemistry letters*, v. 10, n. 18, pp. 5662–5666, 2019.

[36] LIU, B., MANICA, R., XU, Z., et al. "The boundary condition at the air-liquid interface and its effect on film drainage between colliding bubbles", *Current Opinion in Colloid & Interface Science*, 2020.

[37] VAKARELSKI, I. U., MANICA, R., LI, E. Q., et al. "Coalescence dynamics of mobile and immobile fluid interfaces", *Langmuir*, v. 34, n. 5, pp. 2096–2108, 2018.

[38] VAKARELSKI, I. U., YANG, F., THORODDSEN, S. T. "Free-rising bubbles bounce stronger from mobile than immobile water-air interfaces", *Langmuir*, 2020.

[39] SUÑOL, F., GONZÁLEZ-CINCA, R. "Effects of gravity level on bubble detachment, rise, and bouncing with a free surface", *International Journal of Multiphase Flow*, v. 113, pp. 191–198, 2019.

[40] RIBEIRO JR, C. P., MEWES, D. "On the effect of liquid temperature upon bubble coalescence", *Chemical Engineering Science*, v. 61, n. 17, pp. 5704–5716, 2006.

[41] ORVALHO, S., RUZICKA, M. C., OLIVIERI, G., et al. "Bubble coalescence: Effect of bubble approach velocity and liquid viscosity", *Chemical Engineering Science*, v. 134, pp. 205–216, 2015. doi: https://doi.org/10.1016/j.ces.2015.04.053.

[42] REYNOLDS, O. "IV. On the theory of lubrication and its application to Mr. Beauchamp tower's experiments, including an experimental determination of the viscosity of olive oil", *Philosophical transactions of the Royal Society of London*, v. 177, n. 177, pp. 157–234, 1886.

[43] YANG, W., LUO, Z., LAI, Q., et al. "Study on bubble coalescence and bouncing behaviors upon off-center collision in quiescent water", *Experimental Thermal and Fluid Science*, v. 104, pp. 199–208, 2019.

[44] MALYSA, K., KRASOWSKA, M., KRZAN, M. "Influence of surface active substances on bubble motion and collision with various interfaces", *Advances in colloid and interface science*, v. 114, pp. 205–225, 2005.

[45] ORVALHO, S., STANOVSKY, P., RUZICKA, M. C. "Bubble coalescence in electrolytes: effect of bubble approach velocity", *Chemical Engineering Journal*, v. 406, pp. 125926, 2021.

[46] VERSLUIS, M. "High-speed imaging in fluids", *Experiments in fluids*, v. 54, n. 2, pp. 1–35, 2013.

[47] JOINT COMMITTEE FOR GUIDES IN METROLOGY, J. *Guide to the Expression of Uncertainty in Measurement (GUM)*. Relatório técnico, Joint Committee for Guides in Metrology, 2008.

[48] DE SANTO, M., LIGUORI, C., PAOLILLO, A., et al. "Standard uncertainty evaluation in image-based measurements", *Measurement*, v. 36, n. 3-4, pp. 347–358, 2004.

[49] OTSU, N. "A threshold selection method from gray-level histograms", *IEEE transactions on systems, man, and cybernetics*, v. 9, n. 1, pp. 62–66, 1979.

[50] HU, M.-K. "Visual pattern recognition by moment invariants", *IRE transactions on information theory*, v. 8, n. 2, pp. 179–187, 1962.

[51] BOGGS, P. T., DONALDSON, J. R., BYRD, R. H., et al. "Algorithm 676: ODRPACK: software for weighted orthogonal distance regression", *ACM Transactions on Mathematical Software (TOMS)*, v. 15, n. 4, pp. 348–364, 1989.

[52] CROWE, C., SCHWARZKOPF, J., SOMMERFELD, M., et al. *Multiphase Flows with Droplets and Particles, SecondEdition. Taylor & Francis*. CRC Press, 2011.

[53] BRENNEN, C. E. "Fundamentals of Multiphase Flow", *Cambridge Ltd*, 2005.

[54] SILVA, A. D. D. *Bomba seringa com operação em regime contínuo e atuação remota via wi-fi*. B.S. thesis, Universidade Federal do Rio Grande do Norte, 2021.

Appendix A

Supplementary Material 1

This supplementary material presents the fluid properties, the analysis of image moments and ellipses, and the experimental data in the following three sections. The first section presents the data and models for calculating properties such as density, viscosity, and surface tension of fluids in function of temperature. The second section shows a complete analysis of image moments and interpretation with ellipses. Finally, the third section presents the data on bubble characteristics, dimensionless numbers, and coalescence times of experimental data sets I, II, and III.

A.1 Fluid Properties

This section presents the results of properties such as density, viscosity, and surface tension of the phases as a function of temperature. The measurements were correlated with models of 1 or 2 parameters that can predict the fluid properties in a temperature range of 20 - 30 $^{\circ}C$.

A.1.1 Density

The density of water was previously measured over a temperature range of 20 – 30 $^{\circ}C$ presented in Table A.1.1.

The experimental data follows a linear and inversely proportional trend with the range of temperature variation as observed in Figure A.1.1. The standard mean value and standard deviation of the mean properties and the coefficients of the linear regression calculated by Orthogonal Distance Regression [51] are presented in the figure.

The calculation of continuous phase density and their uncertainty in kg/m^3 in a range of 292 to 300 K of temperature with a 95% confidence interval can be

Table A.1.1: Continuous phase density as a function of temperature, whose uncertainty is $u(T) = 0.01$ K.

T [K]	ρ [kg/m^3]	$u(\rho)$ [kg/m^3]
293.15	997.86	5.89×10^{-4}
295.15	997.27	3.46×10^{-2}
297.15	996.82	2.08×10^{-2}
298.15	996.56	4.60×10^{-4}
299.15	996.19	2.08×10^{-2}
301.15	995.63	2.65×10^{-2}
303.15	995.04	1.99×10^{-4}

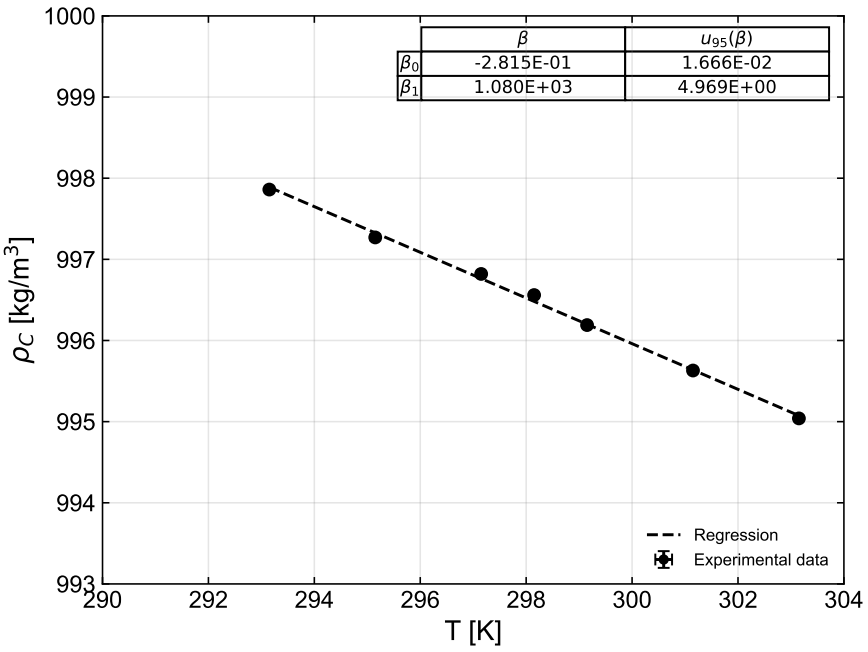

Figure A.1.1: Density as a function of temperature

Table A.1.2: Continuous phase viscosity as a function of temperature. Temperature and viscosity uncertainties are 0.01 K and 0.001 mPa s, respectively.

T [K]	ν [mPa s]
292.09	1.070
292.62	1.050
293.15	1.040
293.66	1.030
294.17	1.010
294.68	1.000
295.18	0.987
295.69	0.974
296.18	0.963
296.68	0.951
297.18	0.940
297.69	0.929
298.19	0.919
298.69	0.909
299.19	0.897
299.69	0.887
300.19	0.875

calculated with the following functions:

$$\rho_C = \beta_0 T + \beta_1 \tag{A.1}$$

where

$$u(\rho_C) = \sqrt{\beta_0^2 u^2(T) + T^2 u^2(\beta_0) + u^2(\beta_1)} \tag{A.2}$$

being T the temperature in Kelvin and $u(T)$ the temperature uncertainty at which the property was measured.

The density of the air used as the dispersed phase is calculated at sea level by the psychrometric chart and its standard relative uncertainty by the uncertainties of mean temperature and mean relative humidity at which the property was measured.

A.1.2 Viscosity

The water viscosity was also previously measured over a 20 - 30 °C temperature range as presented in Table A.1.1.

The calculation of the viscosity and its uncertainty in mPa s for a 95% confidence interval was approximated to an inverse linear model as seen in Figure A.1.2 represented by the following equations:

$$\nu_C = \frac{1}{\beta_0 T + \beta_1} \tag{A.3}$$

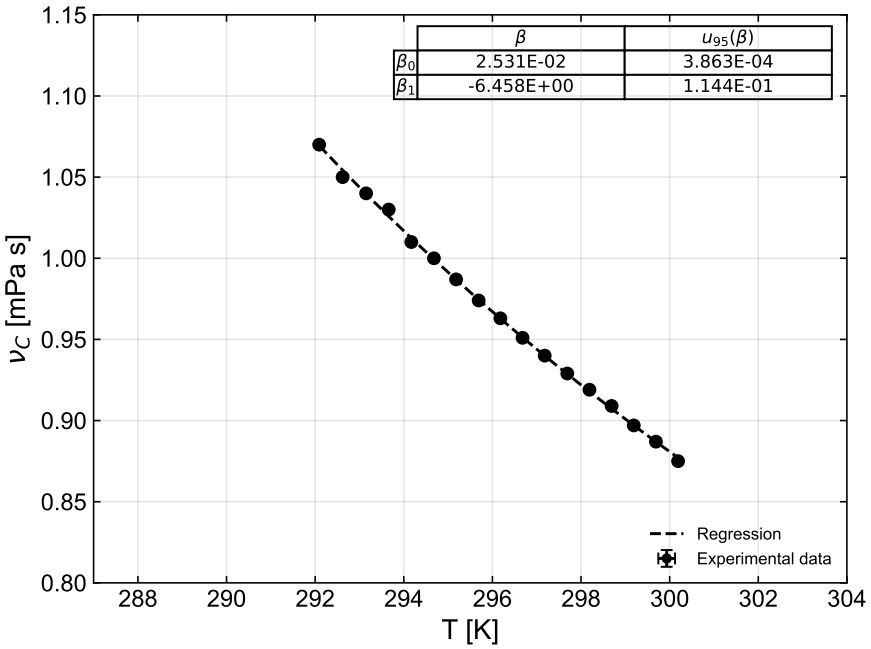

Figure A.1.2: Viscosity as a function of temperature

$$u(\nu_C) = \nu_C^2 \sqrt{\beta_0^2 u^2(T) + T^2 u^2(\beta_0) + u^2(\beta_1)} \tag{A.4}$$

where T is the temperature in Kelvin and $u(T)$ their uncertainty.

A.1.3 Surface Tension

Furthermore, the surface tension of water has also been previously measured over a temperature range of 20 – 30°C presented in Table A.1.3.

The surface tension calculation and its uncertainty in [mN/m] for a 95% confidence interval were approximated to an inverse linear model as seen in Figure A.1.3 represented by the following equations:

$$\sigma = \beta_0 \frac{298}{T} \tag{A.5}$$

$$u(\sigma) = \sigma \sqrt{\left(\frac{1}{T}\right)^2 u^2(T) + \left(\frac{1}{\beta_0}\right)^2 u^2(\beta_0)} \tag{A.6}$$

The β_0 and β_1 of Eqs. A.1 - A.6 and their uncertainties were calculated by ODR. The values of the parameters are presented in Table A.1.4.

Table A.1.3: Surface tension as a function of temperature

T [K]	$u(T)$ [K]	σ [mN/m]	$u(\sigma)$ [mN/m]
292.78	0.02	65.772	3.41×10^{-2}
293.73	0.01	66.158	2.22×10^{-2}
294.21	0.01	65.692	2.25×10^{-2}
294.69	0.02	65.687	2.01×10^{-2}
295.2	0.01	65.289	2.69×10^{-2}
295.67	0.01	65.421	1.91×10^{-2}
296.17	0.01	65.056	2.24×10^{-2}
297.13	0.03	64.955	2.86×10^{-2}
297.61	0.02	64.845	1.67×10^{-2}
298.1	0.01	65.03	2.82×10^{-2}
299.56	0.05	64.386	2.19×10^{-2}
300.16	0.01	64.063	2.65×10^{-2}

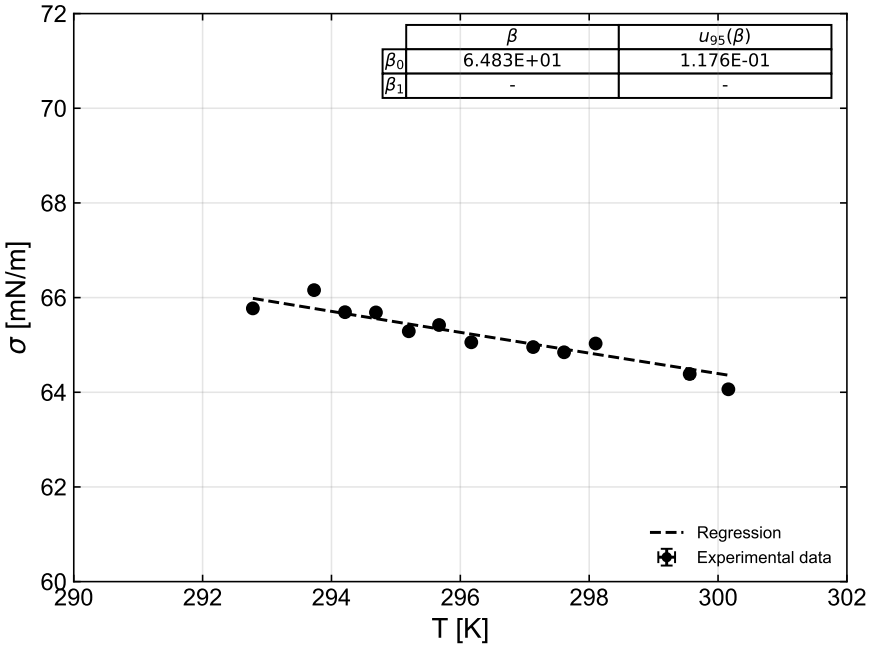

Figure A.1.3: Surface tension as a function of temperature

Table A.1.4: Regression coefficients.

	ρ_C	ν_C	σ
β_0	-0.28 ± 0.02	0.0253 ± 0.0004	64.8 ± 0.1
β_1	1080 ± 5	-6.5 ± 0.1	-

A.2 Analysis of Image Moments and Interpretation with Ellipses

A.2.1 Deduction of the image moments

For a bivariate and binarized distribution, $I(x, y)$ defined as:

$$I(x,y) = \begin{cases} 1, & if (x,y) \in \mathbb{D} \\ 0, & if (x,y) \notin \mathbb{D} \end{cases} \tag{A.7}$$

The moment m_{ij} is calculated as:

$$m_{ij} = \int_{-\infty}^{\infty}\int_{-\infty}^{\infty} x^i y^j I(x,y) dxdy = \iint_{\mathbb{D}} x^i y^j dxdy \tag{A.8}$$

The moments can be calculated based on images formed by pixels, where I represents the pixel intensity of the binary image, and Eq. A.8 becomes:

$$m_{ij} = \sum_{x,y\in\mathbb{D}} x^i y^j \Delta x \Delta y = \sum_{k=1}^{N_b} x_k^i y_k^j \Delta x_k \Delta y_k \tag{A.9}$$

where (x_k, y_k) is the center of the pixel k in $\mathbb{D}$. Using pixel units, $\Delta x_k = \Delta y_k = \Delta = 1$ px.

The coordinates of the centroids (x_c, y_c) are the mean values of x and y given by:

$$x_c = \frac{m_{10}}{m_{00}} = \frac{1}{N_b}\sum_{k=1}^{N_b} x_k \quad ; \quad y_c = \frac{m_{01}}{m_{00}} = \frac{1}{N_b}\sum_{k=1}^{N_b} y_k \tag{A.10}$$

The central moments for the same distribution are defined as:

$$\mu_{ij} = \int_{-\infty}^{\infty}\int_{-\infty}^{\infty} (x-x_c)^i (y-y_c)^j I(x,y)\, dx\, dy = \iint_{\mathbb{D}} (x-x_c)^i (y-y_c)^j\, dx\, dy \tag{A.11}$$

In discrete terms, we have:

$$\mu_{ij} = \sum_{x,y\in\mathbb{D}} (x-x_c)^i (y-y_c)^j \Delta x \Delta y = \sum_{k=1}^{N_b} (x_k - x_c)^i (y_k - y_c)^j \tag{A.12}$$

The first central moments in terms of the ordinary moments are $\mu_{00} = m_{00}$, $\mu_{10} = m_{10} - \frac{m_{10}}{m_{00}} m_{00} = 0$, and $\mu_{01} = m_{01} - \frac{m_{01}}{m_{00}} m_{00} = 0$.

The covariance matrix of the central moments has the form:

$$\Sigma = \begin{bmatrix} \mu_{20} & \mu_{11} \\ \mu_{11} & \mu_{02} \end{bmatrix} \tag{A.13}$$

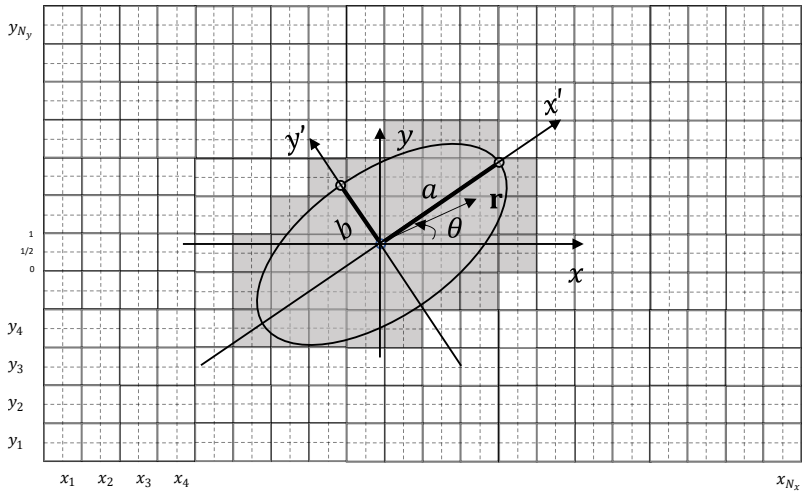

Figure A.2.1: Change of reference (rotation) and representation of an ellipse on a pixel map

which is symmetric and can be diagonalized by an orthogonal matrix constructed with the eigenvectors of the eigenvalue problem: $\Sigma\mathbf{r} = \lambda\mathbf{r}$, or $(\Sigma - \lambda I)\mathbf{r} = 0$, leading to a quadratic solution:

$$|\Sigma - \lambda I| = \begin{vmatrix} \mu_{20} & \mu_{11} \\ \mu_{11} & \mu_{02} \end{vmatrix} - \lambda \begin{vmatrix} 1 & 0 \\ 0 & 1 \end{vmatrix} = \begin{vmatrix} \mu_{20} - \lambda & \mu_{11} \\ \mu_{11} & \mu_{02} - \lambda \end{vmatrix} \tag{A.14}$$

$$|\Sigma - \lambda I| = \lambda^2 - (\mu_{20} - \mu_{02})\lambda + \mu_{20}\mu_{02} - \mu_{11}^2 = 0 \tag{A.15}$$

The solution of Eq. A.15 gives the eigenvalues:

$$\lambda_{1,2} = \frac{\mu_{20} + \mu_{02}}{2} \pm \frac{\sqrt{4\mu_{11}^2 + (\mu_{20} - \mu_{02})^2}}{2},\ \lambda_1 > \lambda_2 \tag{A.16}$$

The eigenvectors $\mathbf{r}_i$ satisfying $\Sigma\mathbf{r}_i = \lambda\mathbf{r}_i$, with $|\mathbf{r}_i| = 1$, determine $\mathbf{r}_1$ and $\mathbf{r}_2$, and $Q = [\mathbf{r}_1\, \mathbf{r}_2]$, such that $Q^T\Sigma Q = \begin{bmatrix} \lambda_1 & 0 \\ 0 & \lambda_2 \end{bmatrix}$, then $\Sigma\mathbf{r} = \lambda\mathbf{r}$, and $Q^T\Sigma Q \cdot Q^T\mathbf{r} = \lambda Q^T\mathbf{r}$, or $\Sigma'\mathbf{r}' = \lambda\mathbf{r}'$. Since $Q^T = Q^{-1}$ (orthogonal), then $\Sigma = (Q\Sigma' Q^T)$.

Rotation

In Figure A.2.1, an ellipse is represented on a pixel map of dimensions $N_x,\ N_y$, along with a change of reference obtained by a rotation around the center at the bubble.

The vectors $\mathbf{r}$ and $\mathbf{r}'$ have respectively distinct coordinates in the (xy) system and the $(x'y')$ system, which diverges from the initial system by an angle (θ), such that:

$$\mathbf{r} = \begin{bmatrix} x \\ y \end{bmatrix}^T \quad \mathbf{r}' = \begin{bmatrix} x' \\ y' \end{bmatrix}^T \tag{A.17}$$

The relation between $\mathbf{r}$ and $\mathbf{r}'$ is given by:

$$\mathbf{r} = Q\mathbf{r}' \tag{A.18}$$

where the rotation matrix Q for rotating a column vector $\mathbf{r}$ in Cartesian coordinates about the origin to obtain $\mathbf{r}'$ is:

$$Q = \begin{bmatrix} \cos\theta & -\sin\theta \\ \sin\theta & \cos\theta \end{bmatrix} \tag{A.19}$$

From the figure, we have $x' = x\cos\theta + y\sin\theta$ and $y' = -x\sin\theta + y\cos\theta$, or equivalently $x = x'\cos\theta - y'\sin\theta$ and $y = x'\sin\theta + y'\cos\theta$.

Therefore, the rotated central moments are defined as:

$$\mu_{20}^{'} = \mu_{20}\cos^2\theta + 2\mu_{11}\sin\theta\cos\theta + \mu_{02}\sin^2\theta \tag{A.20}$$

$$\mu_{02}^{'} = \mu_{20}\sin^2\theta - 2\mu_{11}\sin\theta\cos\theta + \mu_{02}\cos^2\theta \tag{A.21}$$

$$\mu_{11}^{'} = -\mu_{20}\sin\theta\cos\theta - \mu_{11}(\sin^2\theta - \cos^2\theta) + \mu_{11}\cos\theta + \mu_{02}\sin\theta\cos\theta \tag{A.22}$$

To obtain a diagonal covariance matrix, we need to satisfy the following condition:

$$\mu_{11}^{'} = -\mu_{20}\sin\theta\cos\theta + \mu_{11}(\cos^2\theta - \sin^2\theta + \mu_{11}\cos\theta + \mu_{02}\sin\theta\cos\theta = 0 \tag{A.23}$$

Isolating θ and substituting $(1 - \sin^2\theta) = \cos^2\theta$, and $\sin\theta\cos\theta = \frac{1}{2}\sin 2\theta$, we have:

$$\mu_{11}(\theta - \sin^2\theta) = \sin\theta\cos\theta(\mu_{20} - \mu_{02}) = \mu_{11}\cos 2\theta = \frac{\sin 2\theta}{2}(\mu_{20} - \mu_{02}) \tag{A.24}$$

Rearranging the above equation, we get:

$$\frac{2\mu_{11}}{\mu_{20} - \mu_{02}} = \frac{\sin 2\theta}{\cos 2\theta} = \tan 2\theta \tag{A.25}$$

Therefore, θ can be expressed as:

$$\theta = \frac{1}{2}\arctan\left[\frac{2\mu_{11}}{\mu_{20} - \mu_{02}}\right] \tag{A.26}$$

Thus, the orientation was calculated in terms of the central moments μ_{20}, μ_{02}, and μ_{11}.

From equation A.23, we also obtain:

$$\cos^2 2\theta = \left(\frac{\mu_{20} - \mu_{02}}{2\mu_{11}}\right)^2 \sin^2 2\theta = \left(\frac{\mu_{20} - \mu_{02}}{2\mu_{11}}\right)^2 (1 - \cos^2 2\theta) \tag{A.27}$$

Simplifying, we have:

$$\cos^2 2\theta \left[1 + \left(\frac{\mu_{20} - \mu_{02}}{2\mu_{11}}\right)^2\right] = \left(\frac{\mu_{20} - \mu_{02}}{2\mu_{11}}\right)^2 \tag{A.28}$$

Taking the square root on both sides, we get:

$$\cos 2\theta \left[1 + \left(\frac{\mu_{20} - \mu_{02}}{2\mu_{11}}\right)^2\right]^{1/2} = \frac{\mu_{20} - \mu_{02}}{2\mu_{11}} \tag{A.29}$$

or

$$\frac{\cos 2\theta}{2(\mu_{20} - \mu_{02})} = \frac{1}{4\mu_{11}} \left[\frac{4\mu_{11}^2 + (\mu_{20} - \mu_{02})^2}{4\mu_{11}^2}\right]^{-1/2} \tag{A.30}$$

Rearranging, we get:

$$\frac{\cos 2\theta}{2(\mu_{20} - \mu_{02})} = \frac{1}{2} \left[(\mu_{20} - \mu_{02})^2 + 4\mu_{11}^2\right]^{-1/2} \tag{A.31}$$

The above equation will be important later in estimating the eigenvalues.

The definition of λ_1 and λ_2 is obtained from the second-order central moments as follows:

$$\mu_{20}^{'} = \mu_{20} \cos^2 \theta + 2\mu_{11} \sin\theta \cos\theta + \mu_{02} \sin^2 \theta \tag{A.32}$$

By making the following substitutions: $\sin 2\theta = 2\sin\theta\cos\theta$, $\sin^2\theta = 1 - \cos^2\theta$, $\cos\theta = \frac{1+\cos 2\theta}{2}$, $\sin\theta = \frac{1-\cos 2\theta}{2}$, and $\sin 2\theta = \tan 2\theta \cdot \cos 2\theta$ we obtain:

$$\mu_{20}^{'} = \mu_{20} \left(\frac{1 + \cos 2\theta}{2}\right) + \mu_{11} (\sin 2\theta) + \mu_{02} \left(\frac{1 - \cos 2\theta}{2}\right) \tag{A.33}$$

$$= \frac{\mu_{20} + \mu_{02}}{2} + \cos 2\theta \left(\frac{\mu_{20} - \mu_{02}}{2}\right) + \mu_{11} \sin 2\theta \tag{A.34}$$

$$= \frac{\mu_{20} + \mu_{02}}{2} + \frac{\cos 2\theta}{2} (\mu_{20} - \mu_{02} + 2\mu_{11} \tan 2\theta) \tag{A.35}$$

$$= \frac{\mu_{20} + \mu_{02}}{2} + \frac{\cos 2\theta}{2(\mu_{20} - \mu_{02})} \left[(\mu_{20} - \mu_{02})^2 + 4\mu_{11}^2\right] \tag{A.36}$$

Substituting Eq. A.31 into Eq. A.36, we get:

$$\mu_{20}^{'} = \frac{\mu_{20} + \mu_{02}}{2} + \frac{1}{2} \left[(\mu_{20} - \mu_{02})^2 + 4\mu_{11}^2\right]^{-1/2} \left[(\mu_{20} - \mu_{02})^2 + 4\mu_{11}^2\right] \tag{A.37}$$

$$= \frac{\mu_{20} + \mu_{02}}{2} + \frac{1}{2}\left[(\mu_{20} - \mu_{02})^2 + 4\mu_{11}^2\right]^{1/2} = \lambda_1 \tag{A.38}$$

Hence, the formula derived from the rotation $\mu_{20}^{'}$ is in the same form as λ_1. Therefore, λ_1 is the rotated central moment $\mu_{02}^{'}$ by an angle θ.

Similarly, we can get:

$$\mu_{02}^{'} = \frac{\mu_{20} + \mu_{02}}{2} - \frac{1}{2}\left[(\mu_{20} - \mu_{02})^2 + 4\mu_{11}^2\right]^{1/2} = \lambda_2 \tag{A.39}$$

Therefore, Eqs. A.38 and A.39 provide the definitions of λ_1 and λ_2 in terms of the second-order central moments μ_{20}, μ_{02}, and μ_{11}.

A.2.2 Representation of the ellipse.

The equation of the ellipse in Figure A.2.1 is given by Eq. A.40:

$$\frac{x'^2}{a^2} + \frac{y'^2}{b^2} = 1 \tag{A.40}$$

where a is the horizontal semi-axis and b is the vertical semi-axis. Thus,

$$y' = \pm b\sqrt{1 - \frac{x'^2}{a^2}} \tag{A.41}$$

$$x' = \pm a\sqrt{1 - \frac{y'^2}{b^2}} \tag{A.42}$$

Given that, all interior points of the ellipse have $I = 1$ and all exterior points have $I = 0$, it follows that:

$$\mu_{20}^{'} = \iint_{\mathbb{D}} (x' - x_c')^2 dx'dy' \tag{A.43}$$

$$\lambda_1 = \mu_{20}^{'} = 4\int_0^a (x' - x_c')^2 \left[b\sqrt{1 - \frac{(x' - x_c')^2}{a^2}}\right] dx' \tag{A.44}$$

Substituting

$$u = \frac{x' - x_c'}{a},\ du = \frac{1}{a}dx',\ (x' - x_c')^2 = a^2u^2, \tag{A.45}$$

we find that λ_1 is equal to:

$$\lambda_1 = \mu_{20}^{'} = 4a^3b \tag{A.46}$$

Similarly, for λ_2, we have

$$\lambda_2 = \mu_{02}^{'} = 4\int_0^b (y' - y_c')^2 \left[a\sqrt{1 - \frac{(y' - y_c')^2}{b^2}}\right] d\,(y' - y_c') \tag{A.47}$$

and substituting

$$v = \frac{y' - y_c'}{b}, \quad dv = \frac{1}{b}dy', \quad (y' - y_c')^2 = b^2v^2, \tag{A.48}$$

we find that

$$\lambda_2 = \mu_{02}^{'} = 4ab^3 \tag{A.49}$$

Hence, by the ratio of the eigenvalues, we can calculate the semi-axes:

$$\frac{\lambda_1^3}{\lambda_2} = \left(\frac{\pi}{4}\right)^3 \frac{a^9b^3}{\frac{\pi}{4}ab^3} = \left(\frac{\pi}{4}\right)^2 a^8 \tag{A.50}$$

$$a = \left[\frac{16}{\pi^2}\frac{\lambda_1^3}{\lambda_2}\right]^{\frac{1}{8}} \tag{A.51}$$

$$\frac{\lambda_2^3}{\lambda_1} = \left(\frac{\pi}{4}\right)^3 \frac{a^3b^9}{\frac{\pi}{4}a^3b} = \left(\frac{\pi}{4}\right)^2 b^8 \tag{A.52}$$

$$b = \left[\frac{16}{\pi^2}\frac{\lambda_2^3}{\lambda_1}\right]^{\frac{1}{8}} \tag{A.53}$$

Another definitions based on the centered moments are the aspect ratio (ε) between the semi-axes:

$$\varepsilon = \frac{a}{b} = \frac{\left[\frac{16}{\pi^2}\frac{\lambda_1^3}{\lambda_2}\right]^{\frac{1}{8}}}{\left[\frac{16}{\pi^2}\frac{\lambda_2^3}{\lambda_1}\right]^{\frac{1}{8}}} = \frac{\lambda_1^4}{\lambda_2^4} = \frac{\lambda_1}{\lambda_2} \tag{A.54}$$

and the eccentricity:

$$\epsilon = \sqrt{1 - \left(\frac{b}{a}\right)^2} \tag{A.55}$$

A.3 Experimental Data

A.3.1 Bubble Characteristics

Tables A.3.1, A.3.2, and A.3.3 present the results of the bubble's projected area, volume, equivalent diameter, and the mean ascension velocity of experimental data sets I, II, and III, respectively.

Table A.3.1: Bubble characteristics of experimental data set I.

Run	$\overline{A}$ [mm^2]	$\overline{V}$ [mm^3]	$\overline{d}_e$ [mm]	$\overline{U}_y$ [mm/s]
1	10.4 ± 0.3	40.3 ± 0.2	4.25 ± 0.01	246 ± 6
2	12.9 ± 0.2	40.8 ± 0.2	4.27 ± 0.01	245 ± 3
3	12.1 ± 0.2	40.7 ± 0.6	4.27 ± 0.02	260 ± 4
4	12.2 ± 0.2	41.5 ± 0.7	4.30 ± 0.02	257 ± 3
5	10.5 ± 0.3	40.9 ± 0.7	4.27 ± 0.03	244 ± 5
6	12.9 ± 0.1	40.1 ± 0.2	4.25 ± 0.01	236 ± 2
7	12.4 ± 0.1	40.2 ± 0.4	4.25 ± 0.01	256 ± 3
8	10.6 ± 0.3	41.3 ± 0.7	4.29 ± 0.02	243 ± 4
9	13.0 ± 0.2	40.7 ± 0.1	4.27 ± 0.01	235 ± 2
10	12.6 ± 0.1	39.0 ± 0.1	4.21 ± 0.01	236 ± 2
11	10.0 ± 0.2	37.9 ± 0.4	4.17 ± 0.02	253 ± 6
12	10.0 ± 0.2	37.5 ± 0.4	4.15 ± 0.01	252 ± 6
13	11.9 ± 0.2	41.7 ± 0.8	4.30 ± 0.03	259 ± 5
14	10.6 ± 0.2	40.0 ± 0.4	4.24 ± 0.01	249 ± 5
15	11.5 ± 0.1	40.7 ± 0.8	4.27 ± 0.03	259 ± 4
16	12.8 ± 0.1	40.5 ± 0.2	4.26 ± 0.01	239 ± 3
17	12.5 ± 0.1	38.7 ± 0.1	4.20 ± 0.01	239 ± 2
18	13.0 ± 0.1	41.5 ± 0.2	4.29 ± 0.01	249 ± 3
19	12.7 ± 0.1	40.4 ± 0.2	4.26 ± 0.01	253 ± 3
20	12.9 ± 0.1	40.5 ± 0.2	4.26 ± 0.01	242 ± 3
21	12.5 ± 0.1	39.0 ± 0.1	4.21 ± 0.01	239 ± 2
22	10.3 ± 0.3	40.6 ± 0.4	4.26 ± 0.01	247 ± 5
23	11.8 ± 0.1	40.1 ± 0.5	4.25 ± 0.02	261 ± 4
24	12.7 ± 0.2	40.2 ± 0.2	4.25 ± 0.01	249 ± 3
25	10.3 ± 0.3	40.6 ± 0.4	4.26 ± 0.01	247 ± 5
26	12.4 ± 0.1	40.2 ± 0.4	4.25 ± 0.01	256 ± 4
27	13.0 ± 0.2	40.7 ± 0.1	4.27 ± 0.01	235 ± 2
28	10.1 ± 0.2	39.2 ± 0.3	4.21 ± 0.01	250 ± 6
29	10.6 ± 0.2	41.8 ± 0.1	4.31 ± 0.01	245 ± 4
30	12.5 ± 0.1	38.5 ± 0.2	4.19 ± 0.01	238 ± 2

A.3.2 Dimensionless Numbers and Coalescence Time

Tables A.3.4, A.3.5, and A.3.6 present the relevant dimensionless numbers as Eötvös, Weber, and Reynolds, as well as the coalescence time using both collision criteria,

Table A.3.2: Bubble characteristics of experimental data set II.

Run	$\overline{A}$ [mm^2]	$\overline{V}$ [mm^3]	$\overline{d}_e$ [mm]	$\overline{U}_y$ [mm/s]
31	12.6 ± 0.1	39.78 ± 0.04	4.24 ± 0.01	242 ± 2
32	12.7 ± 0.1	40.39 ± 0.04	4.26 ± 0.01	242 ± 2
33	12.7 ± 0.1	40.38 ± 0.04	4.26 ± 0.01	242 ± 2
34	12.5 ± 0.1	39.12 ± 0.04	4.21 ± 0.02	242 ± 2
35	12.9 ± 0.1	41.2 ± 0.2	4.29 ± 0.05	241 ± 2

Table A.3.3: Bubble characteristics of experimental data set III.

Run	$\overline{A}$ [mm^2]	$\overline{V}$ [mm^3]	$\overline{d}_e$ [mm]	$\overline{U}_y$ [mm/s]
36	12.7 ± 0.4	38.6 ± 0.3	4.24 ± 0.01	147 ± 3
37	12.7 ± 0.4	38.7 ± 0.4	4.26 ± 0.01	142 ± 4
38	12.5 ± 0.4	39.0 ± 0.5	4.26 ± 0.02	139 ± 5
39	12.6 ± 0.7	39.7 ± 0.9	4.21 ± 0.03	129 ± 4
40	12.7 ± 0.5	41.9 ± 0.4	4.29 ± 0.01	152 ± 2

of the experimental data set I, II, and III, respectively.

Table A.3.4: Dimensionless numbers and coalescence time of experimental data set I. The coalescence time uncertainty is 2 ms.

Run	Eo	We	$Re_d \times 10^{-3}$	$t_c^{(*)}$ [ms]	$t_c^{(**)}$ [ms]
1	1.97 ± 0.05	3.36 ± 0.16	0.938 ± 0.03	694	680
2	2.47 ± 0.04	3.73 ± 0.09	1.047 ± 0.02	610	588
3	2.32 ± 0.04	4.08 ± 0.13	1.076 ± 0.02	968	948
4	2.34 ± 0.04	4.00 ± 0.10	1.069 ± 0.02	898	878
5	1.99 ± 0.06	3.31 ± 0.14	0.935 ± 0.02	360	346
6	2.47 ± 0.03	3.47 ± 0.07	1.009 ± 0.01	1356	1330
7	2.37 ± 0.03	3.99 ± 0.11	1.071 ± 0.02	774	752
8	2.03 ± 0.06	3.34 ± 0.13	0.943 ± 0.02	220	204
9	2.48 ± 0.03	3.44 ± 0.06	1.006 ± 0.01	1268	1242
10	2.41 ± 0.03	3.42 ± 0.07	0.996 ± 0.01	636	608
11	1.92 ± 0.04	3.50 ± 0.16	0.952 ± 0.02	412	398
12	1.92 ± 0.04	3.49 ± 0.16	0.951 ± 0.02	392	376
13	2.27 ± 0.04	3.98 ± 0.16	1.058 ± 0.02	506	488
14	2.03 ± 0.04	3.50 ± 0.15	0.966 ± 0.02	366	350
15	2.20 ± 0.03	3.93 ± 0.13	1.043 ± 0.02	476	460
16	2.46 ± 0.03	3.55 ± 0.08	1.020 ± 0.01	204	176
17	2.39 ± 0.03	3.49 ± 0.07	1.004 ± 0.01	694	666
18	2.49 ± 0.03	3.87 ± 0.09	1.068 ± 0.02	486	458

19	2.43 ± 0.03	3.95 ± 0.11	1.073 ± 0.02	462	434
20	2.46 ± 0.03	3.65 ± 0.09	1034 ± 0.02	94	64
21	2.40 ± 0.03	3.48 ± 0.07	1.004 ± 0.01	530	500
22	1.96 ± 0.05	3.37 ± 0.15	0.939 ± 0.02	430	416
23	2.25 ± 0.02	4.03 ± 0.12	1.062 ± 0.02	304	288
24	2.43 ± 0.03	3.82 ± 0.10	1.054 ± 0.02	330	304
25	1.96 ± 0.05	3.37 ± 0.15	0.939 ± 0.02	432	418
26	2.37 ± 0.03	3.99 ± 0.11	1.071 ± 0.02	610	588
27	2.48 ± 0.03	3.44 ± 0.06	1.006 ± 0.01	1270	1240
28	1.93 ± 0.05	3.44 ± 0.17	0.945 ± 0.03	638	624
29	2.03 ± 0.05	3.39 ± 0.12	0.951 ± 0.02	726	712
30	2.39 ± 0.03	3.46 ± 0.06	1.000 ± 0.01	776	746

(*) PCC (**) HCC

Table A.3.5: Dimensionless numbers and coalescence time of experimental data set II. The coalescence time uncertainty is 1 ms.

Run	Eo	We	$Re_d \times 10^{-3}$	$t_c^{(*)}$ [ms]	$t_c^{(**)}$ [ms]
31	2.40 ± 0.02	3.58 ± 0.06	1.002 ± 0.01	1548	1521
32	2.43 ± 0.03	3.61 ± 0.06	1.009 ± 0.01	765	748
33	2.42 ± 0.02	3.60 ± 0.06	1.008 ± 0.01	1132	1105
34	2.38 ± 0.02	3.57 ± 0.06	0.998 ± 0.01	1464	1448
35	2.46 ± 0.03	3.59 ± 0.06	1.010 ± 0.01	980	952

(*) PCC (**) HCC

Table A.3.6: Dimensionless numbers and coalescence time of experimental data set III. The coalescence time uncertainty is 1 ms.

Run	Eo	We	$Re_d \times 10^{-3}$	$t_c^{(*)}$ [ms]	$t_c^{(**)}$ [ms]
36	2.41 ± 0.08	1.33 ± 0.05	0.611 ± 0.02	133	113
37	2.41 ± 0.08	1.23 ± 0.07	0.588 ± 0.02	59	37
38	2.39 ± 0.08	1.19 ± 0.09	0.576 ± 0.02	248	225
39	2.41 ± 0.13	1.02 ± 0.07	0.536 ± 0.02	61	36
40	2.43 ± 0.10	1.43 ± 0.05	0.636 ± 0.02	135	114

$^{(*)}$ PCC $^{(**)}$ HCC